The Institute of Paper Chemistry

Appleton, Wisconsin

Doctor's Dissertation

A Study of Dynamic Wettability
on a Hydrophobic Surface

David E. McIntyre

January, 1969

A STUDY OF DYNAMIC WETTABILITY ON A HYDROPHOBIC SURFACE

A thesis submitted by

David E. McIntyre

B.A. 1963, Lawrence University
M.S. 1965, Lawrence University

in partial fulfillment of the requirements
of The Institute of Paper Chemistry
for the degree of Doctor of Philosophy
from Lawrence University,
Appleton, Wisconsin

January, 1969

TABLE OF CONTENTS

SUMMARY

It has long been known that the rate of application of a liquid to a solid greatly affects the wetting characteristics of a dynamic system. The objective of the present study was to investigate a dynamic three-phase system and determine the effects of velocity and acceleration of the fluid on the instantaneous wetting properties of the system. Small drops of water and glycerol-water mixtures were driven in steady-state oscillation in the ellipsoidal mode of deformation on smooth paraffin surfaces. This oscillation was achieved using an electromagnetic coil to drive a steel platform supporting a paraffin surface with a very small amplitude at the resonant frequency of the drop under observation. The oscillations of the drop and the large dynamic contact angle changes were recorded with high-speed filming techniques. The shape changes of the drops were measured from the films on a microcomparator. The contact angles were measured on projections of the films using a specially designed tangentometer device.

The equilibrium descriptions of the drops were obtained by numerical integration of the equation of capillarity expressed in spherical coordinates. The perturbations of the drops about the equilibrium form were described with a Legendre series. This approach allowed a complete theoretical description of the flow, and the kinetic and potential energy transfers for the oscillating drops. Good agreement was obtained between theoretically calculated and experimentally determined drop shapes, volumes, decay times and changes in gravitational potential energy. It was concluded that the theoretical model gave a good description of the physical phenomena.

Calculations from the model were made of the energy associated with the liquid-solid interface being created or removed at different phases in the drop oscillation. The results showed that a lower liquid-solid interfacial energy per cm.^{2} was associated with the reduced dynamic contact angles and a higher value with the increased

dynamic contact angles. Calculations of the interfacial energy changes based on the motion of the drop edges, the experimental dynamic contact angles, and an instantaneous force balance gave results which agreed well with those predicted by the flow model.

It was concluded that fluid flow effects on the curvature of the free liquid surface change orientation requirements for liquid molecules placed in the three-phase boundary region. These orientation changes resulted in energies associated with the liquid-solid area in that specific region that differed from the equilibrium values. Liquid molecules in contact with solid molecules in this region will relax to the equilibrium liquid-solid relationship when the boundary has passed. However, the relationship in the boundary on a real solid surface determines the amount of contact and, therefore, the amount of entrapped vapor in the resulting liquid-solid interface. Higher energy orientation requirements of an increased dynamic contact angle will result in a higher energy interface on a real solid surface (i.e., surface roughness).

The viscous behavior of fluids requires that the liquid molecules have zero velocity when placed in the boundary region (i.e., no slip at the wall). Rapidly relaxing molecules should meet the orientation requirements in the boundary instantly, and the energies (differing from the equilibrium) associated with this region can be determined from the fluid flow description. This was shown in the results of Rose, et al., (24-26) who found a linear relationship between the cosine of the advancing contact angle and the steady-state velocity for liquid-vapor interfaces in capillary tubes. A constant increase in the viscous forces (i.e., the constant velocity gradients characterized by the steady velocities) was opposed by a constant increase in the energy of the orientation requirements in the three-phase boundary (i.e., constant decrease in the cosine of the dynamic contact angle). In the present study of oscillating drops, the rates of shear were small compared

to very large rates of change of rate of shear. No measurable viscous effects were obtained. The dynamic contact angles resulted from the very large inertial forces. Linear relationships were found between the acceleration gradient and the cosine of the dynamic contact angle for all the drops. The average slope of this relationship was $3 \times 10^{-6}/\text{sec.}^{-2}$. Thus, the contact angle increased slightly with an increasing rate of deceleration.

The observed contact angle changes for the oscillating drops were 20 to 30 degrees. The median dynamic and the equilibrium contact angles were the same for drops of water and drops of less than 65% glycerol. The median dynamic values were slightly higher than the equilibrium values for drops of more than 65% glycerol. This indicated that some molecules in the glycerol-H_2O complex for drops containing more than 65% glycerol could not relax rapidly enough to meet the orientation requirements in the three-phase boundary. This resulted in a slightly increased energy in this region.

INTRODUCTION

Wetting is a physical phenomenon involved in many industrial processes. It is an area of considerable interest to the paper industry in the application of coatings, adhesives, inks, and other operations. The degree of wetting may be thought of as the amount of molecular contact per unit area achieved between a liquid and a solid. The quality of the coverage, the ease of application, and the adhesion of the applied liquid to the solid all depend largely on the wetting characteristics of the system.

Many equilibrium studies have been made to evaluate the wetting relationship between liquids and solids. Wetting in an ideal equilibrium system is determined solely by its fundamental thermodynamic properties (i.e., the surface tension of the liquid, and the surface energy of the smooth solid). The equilibrium contact angle is a measure of the balance of these forces.

However, for industrial systems, the applied liquids are moving relative to the solid surfaces. Equilibrium studies are not sufficient to describe the wetting of these systems. The wetting will be affected by the mechanical and geometrical properties in addition to the thermodynamic properties of the system. The dynamic contact angle is a measure of the instantaneous wetting properties of such a system.

It is desirable, then, to investigate the effects of velocity and acceleration of a fluid (and, therefore, viscous and inertial effects) on dynamic contact angles.

BACKGROUND OF THE PROBLEM

Many studies have been made of equilibrium wetting situations. In addition, much emphasis has been placed on the hysteresis of advancing and receding contact angles. Some of this literature will be reviewed here as background for the dynamic problem. The dynamic wetting studies will then be reviewed.

EQUILIBRIUM CONTACT ANGLES

Laplace, in 1806, (1) explained the adhesion of liquids to solids in terms of central fields of force between volume elements of a continuous medium. This approach resulted in the fundamental equation of capillarity. The difficulty with this treatment was that the parameters defining the interparticle field of force were not experimentally obtainable.

Young (2) at the same time treated the contact angle of a liquid on a solid as resulting from a mechanical equilibrium of three-surface tensions. Johnson (53) has given a clear statement of the thermodynamic justification of Young's equation. Young's equation is given as, $\gamma_{sv} - \gamma_{sl} = \gamma_{lv} \cos\phi$. In this expression*, ϕ = the liquid-solid contact angle measured in the liquid between the tangent to the liquid surface at the point of contact and the plane of the solid surface, γ_{lv} = the surface energy of the liquid surface in equilibrium with its vapor (ergs/cm.^{2}), γ_{sv} = the surface energy of the solid in equilibrium with the vapor (ergs/cm.^{2}), γ_{sl} = the interfacial energy of solid and liquid in equilibrium (ergs/cm.^{2}). This concept of contact angle was important to the notion of wettability. Every liquid wets a surface to some extent, and the contact angle is seen to be a useful inverse measure of spreadability or wettability. However, it is hard to measure γ_{sl} and γ_{sv}

*The contact angle has been designated by ϕ in this work to avoid confusion with the spherical coordinate, θ.

reliably. Also, most solid surfaces are not systems in equilibrium. Recently, Lester (3) has shown that Young's approach is correct only if the surface is not too deformable.

Sixty years after Young, Dupré (4) derived the reversible work of adhesion of liquid and solid and its relation to the surface free energies from a thermodynamic approach. His equation merely says that the reversible work of adhesion is equal to the free energy change in the system,

$$W_{sl} = \gamma_{sv} + \gamma_{lv} - \gamma_{sl}.$$

Here, W_{sl} is the work of adhesion, and γ_{sl}, γ_{sv}, γ_{lv} are the surface free energies in ergs/cm.^{2} with the same subscripts as Young's equation.

In 1937, Bangham and Razouk (5, 6) showed the importance of including the adsorption of vapor on the surface of the solid phase in deriving the equilibrium expressions concerning the contact angle. The following combination of the Young and Dupré equations resulted.

$$W_{sl} = (\gamma_{s^o} - \gamma_{sv}) + \gamma_{lv} (1 + \cos\phi).$$

Here, γ_{s^o} = energy of solid surface against a vacuum in ergs/cm.^{2}. The first term on the right is the free energy decrease on immersion of the solid in the saturated vapor phase.

These relationships are true only for perfectly smooth isotropic surfaces in systems that are in mechanical and thermal equilibrium.

HYSTERESIS OF EQUILIBRIUM CONTACT ANGLES

Hysteresis between advanced and receded equilibrium contact angles of liquids on solid surfaces has been noted many times in the literature. This hysteresis

can be caused by partially adsorbed films on the solid surface which give a surface of different energy sites on advancing and receding. It can also be caused by roughness of the solid surface.

Bartell and Bristol in 1940 (7) studied the wetting characteristics of solid surfaces covered with adsorbed films. They concluded that clean solid surfaces adsorb constituents from the air, and these heterogeneities can be readily detected by contact angle measurements. Yarnold in 1946 (8), and Yarnold and Mason in 1949 (9), included in Young's equation the effects of adsorbed films on the solid's surface energy. This resulted in general expressions for hysteresis of the contact angle on advancing and receding.

Many workers have investigated contact angle hysteresis caused by surface roughness. Wenzel (10) defined a measured roughness ratio, rr = actual surface area/ geometric surface area. The cosine of the advancing contact angle on a rough surface was given as rr times that found for an advancing contact angle on a plane surface. In 1944, Cassie and Baxter (11) extended Wenzel's treatment. They considered surfaces composed of small regions of different types of roughness. The overall roughness effect on the apparent contact angle was established by a summation of the effect of the small regions. Shuttleworth and Bailey (12) in 1948 introduced the concept of a metastable equilibrium of a liquid at rest on a rough surface. They indicated that contact angle hysteresis is due to a difference in minimum total surface free energy when the liquid comes to rest on advancing and receding.

The culmination of the earlier work and thinking about contact angle hysteresis is found in a series of four 1964 articles by Johnson and Dettre (13-16). The metastable configurations suggested by Shuttleworth and Bailey were incorporated into computer studies. Heterogeneous surfaces resulting from surface roughness and partially adsorbed films were considered. They predicted the particular contact

angle hysteresis for idealized heterogeneous surfaces simulated with a computer and verified the results experimentally.

Schwartz, Rader, and Huey in a 1964 study (17) were concerned with the pressures required to move small indices (separated droplets) of high surface tension fluids in small, smooth capillary tubes of Teflon and polyethylene. They defined a critical line force as the force necessary per cm. of three-phase boundary (liquid-solid-air) to cause the index to move and keep it in motion. They defined hysteresis in their system as the difference between the advancing and receding contact angles extrapolated to zero velocity. The critical line force was found to increase linearly with decreasing cosine of the equilibrium contact angle of various liquids, and continued to do so for liquids with equilibrium contact angles greater than 90°. They indicated that in their system surface roughness would be expected to be the sole cause for the hysteresis. However, the surface roughness effect would be expected to be maximum at $\phi = 90°$. Since the hysteresis continued to increase with equilibrium contact angles, Schwartz and coworkers concluded that roughness was not the sole cause of the critical line phenomenon or of the contact angle hysteresis. They implied that the thermodynamic equilibrium value of the solid-liquid interface given by the Young equation may not hold in the highly localized region of the three-phase boundary line.

DYNAMIC CONTACT ANGLES

Ablett (18) in 1923 was the first to publish a study of dynamic contact angles. He used a paraffin-water-air system. A horizontal, hollow cylinder whose inner surface was machined paraffin was placed half submerged in a tank of water. The cylinder was rotated at different constant speeds, and the advancing and receding contact angles were determined with a mirror arrangement. He found large increases in the advancing contact angle and large decreases in the receding contact angle at

speeds from zero to 0.4 mm./sec. At higher velocities, the dynamic angles reached constant values. The maximum value of the advancing contact angle was about 8° higher, and the minimum value of the receding angle was about 8° lower than the equilibrium value of 104°.

In 1948, Yarnold and Mason (9) measured dynamic contact angles of water on paraffin. A plane water surface was raised or lowered hydraulically at a definite rate while in contact with the surface of a steel sphere coated with paraffin wax which was suspended from a Sucksmith ring balance. The force experienced by the sphere and position of the water surface was continuously recorded, and the angle of contact was determined graphically from the coincidence of the observed upward force with the calculated hydrostatic upthrust. At velocities over 1.6 mm./min. they found small but distinct increases in the advancing contact angles and decreases in the receding contact angles with increasing velocities. They also pointed out a dependence of the contact angle on the time of immersion of the paraffin surface in the water.

Elliot and Leese in 1957 (19) and 1959 (20) published studies with dynamic contact angles. An air bubble was released from a jet submerged in water. The impact of the bubble with a horizontal paraffin surface and the subsequent contact angle changes were recorded with a motion picture camera at 53 frames per second. The air bubble in water rebounded from the surface several times, and the apparent contact angle changed from an initial value of zero to 105° at equilibrium in approximately 0.2 sec. At 53 frames per second they most certainly missed most of the oscillation and marked changes of the contact angle. Their main concern was with the equilibrium time for air bubbles released in different liquids.

Knight, in a 1947 thesis (21) at the Institute, investigated spontaneous wettability of paper surfaces. He used an apparatus developed at the Institute to

apply and remove ink solutions rapidly across paper surfaces at velocities up to 241 ft./min. He noted that wettability became less with increasing velocities. This would indicate a dependence of the dynamic contact angles on velocity. However, Knight was concerned with wettability patterns and treatments affecting surface properties and not direct investigation of dynamic contact angles.

Much of the work with dynamic contact angles has resulted from considerations of the rate dependency of the capillary driving force. Both Barrer (22) and Brittin (23) have given theoretical consideration to the changes in interfacial curvature due to the fluid flow in capillary rise, and both have applied the Navier-Stokes equations to the problem. Barrer limited his analysis to cases where the acceleration terms of the equations can be dropped, and Brittin retained these acceleration terms in an approximate way.

Rose and Heins (24) used a Nujol-air-glass system to study the effect of different steady velocities on dynamic contact angles in capillary flow. They found a negative linear relationship between the cosine of the advancing contact angle and the fluid velocity.

From zero to 0.23 cm./sec. the advancing contact angle increased from 20 to 80°. The data were obtained at equilibrium velocities with no acceleration effects. Rose (25), in a 1962 discussion of capillary rise, indicated that a constant curvature interface can be expected at the junction of two immiscible fluids for steady flow in a capillary tube of constant cross section. In a 1962 paper, Rose, Chaudhari and Fara (26) started with this assumption, and further assumed that the observed advancing dynamic contact angle is a measure of this curvature. They then assumed that the advancing interfacial curvature is a mixed function of interfacial velocity, Z', and acceleration, Z''. They used a Maclaurin Series expansion to express the advancing contact angle in terms of Z' and Z''. All but the first three

terms of the series were assumed to be negligible. This resulted in the expression,

$$\cos \phi_a = \cos \phi_e + M_v Z' + M_a Z'' + \ldots,$$

Here, $\cos \phi_e$ = the equilibrium contact angle, and M_v and M_a are constants which are the time zero limits of the partial derivatives of $\cos \phi_a$ with Z' and Z'', respectively. Their experimental work with steady-state capillary flow and nonsteady-state motion in a manometer system all indicated a good linear correlation of $\cos \phi_a$ with $M_v Z'$. The $M_a Z''$ term was dropped from their expression. It was noted that the accelerations were small by the time measurements could be made of the dynamic contact angles in their manometer system.

McIntyre and Swanson (27), in 1963, developed a procedure for using high-speed photography to film the impact of a fluid drop with a low energy surface and to observe the subsequent contact angle changes as the drop oscillated on the surface. Richards and Swanson (28), in 1964, improved the filming techniques. They found the damping times for the drops were linear with the viscous properties of the various liquids used in the study. However, no conclusions could be drawn regarding the observed dynamic contact angles and the mechanical properties of the system since the hydrodynamic properties of this type of oscillation were too complex to analyze.

Elliot and Riddiford in 1962 (29) caused volumes of liquids to grow and shrink between two parallel plates. They found a rate dependency of the contact at velocities greater than 1 mm./min. For the air-water-siliconed glass system, the advancing contact angle increased from 103 to 115 degrees with velocities from 1 to 8 mm./min., but the contact angle remained at 115° with further velocity increases (up to approximately 100 mm./min.). In 1967 Elliot and Riddiford (30) published another study demonstrating dynamic contact angles at various interfacial velocities by causing a radial growth of a puddle between two plates. They used siliconed

glass and polyethylene plates. They studied the water-air system and several two-liquid systems. They used a kinetic interpretation originally suggested by Hansen and Miotto (31). This approach compares the interfacial velocity with the natural displacement velocity of the molecules in the solid-liquid-vapor boundary. The natural displacement velocity is given by the ratio of the peripheral thickness to the relaxation time of the most slowly relaxing molecule at the periphery. In the air-water-siliconed glass system at speeds less than 1 mm./min., no changes in the contact angle were observed, and this velocity was taken as an underestimate of the natural displacement velocity. As the interfacial velocity increased from 1 mm./min. to 8 mm./min., the peripheral molecules became increasingly disoriented giving rise to an increasing advancing contact angle. The maximum angle was reached at 8 mm./min. This interfacial velocity was taken as the point of complete disorientation of the molecules and, therefore, an overestimation of the natural displacement velocity of the molecules in the periphery. For the air-water-siliconed glass system, using molecular dimensions as the thickness of the periphery, these estimates of the natural displacement velocity led to a maximum value of 10^{-5} seconds and minimum value of 10^{-6} seconds for the relaxation time of the water molecules in the periphery. These values were reasonable when compared to molecular relaxation times (45) of 10^{-10} sec. for bulk water molecules and 10^{-3} sec. for water molecules in the solid state (ice). The water structure in the periphery would be expected to be more oriented than in the bulk region, but less oriented than the solid state. Based on these relaxation times, Elliot and Riddiford estimated an energy barrier between 5 and 7 kcal./mole for the adsorption of water molecules on the solid surface.

STATEMENT OF THE THESIS PROBLEM

When a three-phase, solid-liquid-vapor, system is at equilibrium, the wetting characteristics are determined solely by the fundamental thermodynamic properties of the system. However, when such a system is dynamic, the instantaneous wetting characteristics are also affected by the external or mechanical properties of the system.

The objective of this thesis was to investigate a dynamic three-phase system and to determine the effects of velocity and acceleration of the fluid on the instantaneous wetting properties.

APPROACH TO THE THESIS PROBLEM

It was desirable to choose a simple system in which dynamic contact angles could be observed and photographed. It was also necessary that the hydrodynamics of the system be amenable to analysis. The steady-state oscillation of small drops undergoing the ellipsoidal mode of deformation on a plane surface provided such a system. This deformation was symmetrical about the vertical axis and reduced the problem to two independent variables. The dynamic changes in this system were readily recorded using high-speed filming techniques.

Smooth paraffin surfaces were chosen as the substrate material to minimize roughness effects. High surface tension liquids provided the easiest system in which to force steady-state oscillations and to give readily observable contact angle changes. To prevent irrelevant dynamic surface tension effects, (i.e., mass transfer of surfactants and surface flow due to surface tension gradients), very pure liquids were used. Water and water-glycerol mixtures were the liquids selected for this study. These liquids have high surface tensions of comparable magnitudes and provided a wide range of viscosity.

The oscillation of the drops was forced using an electromagnetic coil to drive a steel platform to which the paraffin surfaces were attached. The natural frequencies of vibration of the drops were determined by generating a range of frequencies with an audio-oscillator. The oscillations needed very little reinforcement. The amplitudes imparted to the paraffin surfaces were so extremely small they could not be detected. The drop oscillations were recorded on film at 4000 to 5000 frames per second. The time function was recorded on the side of the films at 10^{-3} second intervals with a strobe flash. The absolute scale was obtained in CGS units by filming a stage micrometer during each series of filming sessions. This approach resulted in a good experimental description of dynamic contact angles and the corresponding fluid motion.

THEORETICAL CONSIDERATIONS

INTERFACIAL ENERGIES

Surface tension and interfacial energies arise from a number of intermolecular forces (54). These forces depend on the chemical nature of the materials. Fowkes (32) developed an interesting approach to the calculation of surface tensions and interfacial energies based on summing the contributions of the different attractive forces in the materials. For solid-liquid systems interacting by dispersion forces only, Fowkes' approach works fairly well.

The systems used in this study were paraffin and water and water-glycerol mixtures. The surface forces of the hydrocarbon paraffin surfaces are primarily dispersion forces. Therefore, in this study, the solid-liquid interactions consisted mainly of dispersion-type forces.

The well-known Young equation for the contact angle of a liquid on a solid is

$$\gamma_{lv}\cos\phi = \gamma_{sv} - \gamma_{ls} - \pi_e. \qquad (1)$$

Here, γ_{lv} is the liquid-vapor interfacial energy per cm.^{2}, γ_{sv} is the solid-vapor interfacial energy per cm.^{2}, γ_{ls} is the interfacial energy per cm.^{2} between the liquid and solid, ϕ is the contact angle, and π_e is the equilibrium film pressure of the adsorbed vapor on the solid surface in energy per cm.$^{-2}$.

According to Fowkes, the geometric mean of the dispersion forces can be used to predict the interfacial energy between a liquid and solid interacting by these forces only. The interfacial energy is given by

$$\gamma_{ls} = \gamma_{lv} + \gamma_{sv} - 2\sqrt{\gamma_l^{(d)}\gamma_s^{(d)}}. \qquad (2)$$

Here, $\gamma_{\underline{l}}^{(\underline{d})}$ and $\gamma_{\underline{s}}^{(\underline{d})}$ are the dispersion components of the respective liquid and solid surface energies.

Substitution of Equation (2) into Equation (1) gives the result,

$$\gamma_{lv}\cos\phi = -\gamma_{lv} + 2\sqrt{\gamma_l^{(d)}\gamma_s^{(d)}} - \pi_e. \qquad (3)$$

Phillips and Riddiford (33) have shown that, for water on paraffin, the adsorbed liquid film pressure is zero. For the systems used in this study, this further simplifies Equation (3). Finally, using the critical surface tension method of Zisman (34), an approximation to the surface energy of a solid can be determined by plotting the experimental values of the cosine of the equilibrium contact angles of different surface tension liquids on the solid versus their surface tensions. Extrapolation of such a plot to zero contact angle gives the maximum surface tension of liquids which will wet the solid. This value can be taken as an estimate of the surface energy of the solid if the surfaces are smooth and the liquid film pressures are zero.

For a paraffin surface $\gamma_{\underline{sv}} = \gamma_{\underline{s}}^{(\underline{d})}$. Therefore, with a knowledge of the equilibrium contact angles of the water and water-glycerol mixtures on the paraffin surfaces used in this study, good approximations to the liquid-solid interfacial energies can be made. In addition, dispersion force contributions of the liquid to liquid-solid interfacial energies can also be calculated.

FLOW MODEL FOR AN OSCILLATING DROP ON A PLANE SURFACE

APPROACH

Spherical coordinates were selected as appropriate to describe the geometry of a drop resting on a plane surface. The origin was selected as the center of the base of the drop in contact with the plane solid surface. This selection of

coordinate system and placement of the origin reduced the problem to one of two independent variables since there was symmetry about the vertical axis. Also, subsequent integral expressions were conveniently evaluated by integrating θ, the angle of displacement from the vertical axis, from zero to 90 degrees.

The radial coordinate, r, of the oscillating drop surface can be described at any time by,

$$r = R(\theta) + S(\theta,t). \tag{4}$$

Here, $R(\theta)$, is the equilibrium description and is a function of θ only. $S(\theta,t)$ describes the surface perturbations and is a function of θ and the time, t.

EQUILIBRIUM SURFACE DESCRIPTION

For sufficiently small drops, the equilibrium portion, $R(\theta)$, of Equation (4) would reduce to the equation of a sphere (or circle in two dimensions). However, it has been shown that for drops larger than, approximately, 1 mm.^{3} (35) gravitational effects are significant in flattening a sessile drop. The drops used in this study were from 1 to 8 mm.^{3} It was necessary, therefore, to include gravitational effect in the equilibrium description.

For a sessile drop, the equation of capillarity can be written (36),

$$\gamma_{lv}(1/R_1 + 1/R_2) = \Delta\rho g y_o + (2\gamma_{lv}/b). \tag{5}$$

Here, γ_{lv} = the liquid-vapor interfacial tension, R_1 and R_2 are the principal radii of curvature, g = the gravitational constant, $\Delta\rho$ = the density difference of the phases, y_o = the ordinate position, and b = the radius of curvature at the drop top. This equation is given with the origin at the top of the drop.

The origin can be translated to the center of the base by substituting $\underline{y} = \underline{y}_o + \underline{h}$, where $\underline{h}$ = drop height. The principal radii, $\underline{R}_1$ and $\underline{R}_2$, can be derived in polar coordinates. Finally, the substitution of $\underline{y} = \underline{R} \cos \theta$ can be made. (θ is the angular displacement from the vertical axis.) Applying these operations to Equation (5) and rearranging terms, the following result is obtained:

$$R'' = \left(\frac{R^2+2R'^2}{R}\right) + \left(\frac{R'\tan\theta+R}{R}\right)\left(\frac{R^2+R'^2}{R}\right) - \frac{1}{R}\left(\frac{\rho g}{\gamma_{lv}}(R\cos\theta+h) + \frac{2}{b}\right)(R^2+R'^2)^{3/2}. \quad (6)$$

Here, $\underline{R}' = d\underline{R}/d\theta$ and $\underline{R}'' = d^2\underline{R}/d\theta^2$. In Equation (6) $\underline{R}''$ is expressed as a function of θ, $\underline{R}$, and $\underline{R}'$. This expression is well suited for numerical integration using Runge-Kutta methods and incrementing the θ. Numerical integration of Equation (6) will result in a table of θ values and the corresponding $\underline{R}$ values which describe the equilibrium surface, including gravitational effects, of a sessile drop with the origin at the center of the base. Such tables can then be used as the $\underline{R}(\theta)$ portion of Equation (4).

DYNAMIC SURFACE DESCRIPTION

Small oscillations of liquid globules about the equilibrium form (spherical) have been successfully described by Rayleigh (37) and Lamb (38) using spherical harmonics. In this approach, the surface perturbations are described by expanding the dynamic portion of $\underline{r}$ in a series of Legendre functions. This approach assumes that the flow within the drop is irrotational and that the perturbations are small relative to the dimensions of the drop.

This approach was adapted for describing the perturbations of a small drop oscillating on a plane surface. The dynamic portion of Equation (4) can be expanded in the series

$$S(\theta,t) = e^{i\omega t}\left[A_o + A_1P_1(\mu) + A_2P_2(\mu) + A_3P_3(\mu) + \ldots + A_nP_n(\mu)\right]. \quad (7)$$

In this expression, the P_n terms are Legendre polynomials, and these are a function of the cosine of the colatitude (i.e., $\mu = \cos\theta$). The A_n terms are complex coefficients, ω is the circular frequency of the vibration, and t is the time. The $P_n(\mu)$ terms are generated from the general formula (39),

$$P_n(\mu) = \frac{1}{2^n n!} \frac{d^n}{d\mu^n} (\mu^2-1)^n. \tag{8}$$

Here, n can have any integer value. An important property of these Legendre functions is that any two polynomials of different order are orthogonal (40).

The Legendre functions are applied to the equilibrium configuration of the drop on a plane surface with the origin at the center of the drop base. In order to maintain the symmetry of the vibration of the drop and its mirror image, the A_n coefficients in Equation (7) of odd order should be zero. Also, A_o should be very small since the volume of the drop is constant. This reduces the expression for the description of the liquid surface perturbations to

$$S(\theta,t) = e^{i\omega t}[A_2P_2(\mu) + A_4P_4(\mu) + \ldots + A_nP_n(\mu)]. \tag{9}$$

The values of the A_n coefficients are determined by the geometry of the system and the boundary conditions. Therefore, Equation (9) and the table of equilibrium surface values provide the overall description of the surface of a drop oscillating on a plane surface that was proposed in Equation (4).

THE VELOCITY POTENTIAL AND ITS DERIVATIVES

If the fluid flow is assumed to be irrotational, an expression can be developed using spherical harmonics and the description for r to solve the Laplace equation,

$$\nabla^2\psi = 0. \tag{10}$$

Here, ψ is the velocity potential.

For a drop on a plane surface, ψ was expressed as a Legendre series consisting of even order terms,

$$\psi(r,\theta,t) = -i\omega e^{i\omega t}[r^2 B_2 P_2(\mu) + r^4 B_4 P_4(\mu) + \ldots + r^n B_n P_n(\mu)]. \qquad (11)$$

The $\underline{B}_n$ coefficients are also determined by the geometry and the boundary conditions of the system. The relationship between the $\underline{A}_n$ and $\underline{B}_n$ coefficients is uniquely determined through the equation for the velocity in the radial direction. This is given by

$$\frac{\partial S}{\partial t} = -\frac{\partial \psi}{\partial r} + \frac{1}{r^2}\frac{\partial \psi}{\theta} \cdot \frac{\partial r}{\partial \theta}. \qquad (12)$$

Here, $\underline{S}$ involves the $\underline{A}_n$ coefficients and ψ involves the $\underline{B}_n$ coefficients. The approximation is generally made that the right hand of Equation (12) is evaluated at the unperturbed surface. In the free drop case, with the origin at the center of the sphere, the radial direction is also normal to the liquid surface. In that case, the right-hand side of Equation (12) reduces to the first term. In the case of a drop on a plane surface the second term on the right-hand side of Equation (12) must be retained because of the displacement of the origin from the center of the sphere and the gravitational flattening effects.

The partial derivatives of the velocity potential function, ψ, can be obtained with the aid of the formula (39),

$$\frac{dP_n(\mu)}{d\theta} = \frac{n}{\sin\theta}[\cos\theta\, P_n(\mu) - P_{n-1}(\mu)]. \qquad (13)$$

This is for values of $\underline{n} \geq 1$, and $\mu = \cos\theta$. The partial derivatives of ψ are given by

$$\frac{\partial \psi}{\partial r} = -i\omega e^{i\omega t}[2rB_2 P_2(\mu) + 4r^3 B_4 P_4(\mu) + \ldots + nr^{n-1} B_n P_n(\mu)], \qquad (14)$$

and

$$\frac{\partial \psi}{\partial \theta} = - \frac{i\omega e^{i\omega t}}{\sin \theta} \{2r^2 B_2[\mu P_2(\mu) - P_1(\mu)] + 4r^4 B_4[\mu P_4(\mu) - P_3(\mu)] + \ldots$$

$$+ nr^n B_n[\mu P_n(\mu) - P_{n-1}(\mu)]\}. \qquad (15)$$

Finally, the partial derivative of $\underline{r}$ with respect to θ must be determined. This can be closely approximated by taking the differences $\Delta \underline{R}/\Delta\theta$ from the table of numerically integrated equilibrium values of $\underline{R}(\theta)$.

INTEGRAL EXPRESSIONS

With expressions developed for the description of the dynamic liquid surface and the velocity potential, the entire system of a drop oscillating on a plane surface can be described.

Drop Volume

The drop volume is given by,

$$Y = \int_0^{\pi/2} 2/3 \, \pi r^3 \sin\theta d\theta. \qquad (16)$$

Potential Energy of the Liquid-Vapor Interface

If $\gamma_{\underline{lv}}$ is the liquid-vapor interfacial surface energy and is assumed constant, the potential energy stored in this surface is given by,

$$V_l = \gamma_{lv} \int_0^{\pi/2} 2\pi r^2 \sqrt{1 + \frac{1}{r^2}\left(\frac{\partial r}{\partial \theta}\right)^2} \sin\theta d\theta. \qquad (17)$$

Here, $\underline{r}$ is the dynamic value determined from Equation (4), and $(\partial r/\partial\theta)^2$ is approximated from $\underline{R}(\theta)$.

Potential Energy of the Liquid-Solid Interface

The potential energy of the liquid-solid interface is given by

$$V_2 = \gamma_{ls} - \pi\,[r(\pi/2,t)]^2 \tag{18}$$

Here, γ_{ls} is the liquid-solid interfacial energy. It will be constant for most of the region, but is not necessarily constant in the region near the three-phase boundary.

Gravitational Potential Energy

The gravitational potential energy is given by

$$V_3 = \int_0^{\pi/2} \frac{1}{2}\,\pi\rho g r^4 \cos\theta \sin\theta d\theta. \tag{19}$$

Here, ρ is the liquid density, and g is the gravitational constant.

Kinetic Energy

The kinetic energy is given by

$$T = \pi\rho \int_0^{\pi/2} \psi \frac{\partial\psi}{\partial r} R^2 \sin\theta d\theta - \pi\rho \int_0^{\pi/2} \psi \frac{\partial\psi}{\partial\theta} \frac{\partial R}{\partial\theta} \sin\theta d\theta. \tag{20}$$

The approximation is made here that the integration is carried out over the unperturbed surface.

Viscous Dissipation

Lamb's approach is used to determine the energy of viscous dissipation for the drop on a plane surface. For a fluid of constant density and irrotational flow, Lamb's expression (55) in vector notation (with the curl equal to zero) is,

$$2F = -\eta \int\int 2\,[(\vec{v}\cdot\nabla)\cdot\vec{v}]\cdot\hat{n}\cdot d\sigma. \tag{21}$$

Here η is the fluid viscosity and $d\sigma$ is an element of surface. For symmetry about the vertical axis, Equation (21) is evaluated over the unperturbed surface with,

$$\left\{(\vec{v}\cdot\nabla)\vec{v}\right\}_R = v_r \frac{\partial v_r}{\partial r} + \frac{v_\theta}{r}\frac{\partial v_r}{\partial \theta} - \frac{v_\theta^2}{r} ,$$

$$\left\{(\vec{v}\cdot\nabla)\vec{v}\right\}_\theta = v_r \frac{\partial v_\theta}{\partial r} + \frac{v_\theta}{r}\frac{\partial v_\theta}{\partial \theta} + \frac{v_r v_\theta}{r} . \qquad (21a)$$

and

$$v_r = -\frac{\partial \psi}{\partial r} , \quad v_\theta = -\frac{1}{r}\frac{\partial \psi}{\partial \theta} . \qquad (21b)$$

The normal coordinates in this system are,

$$n_r = \frac{1}{\sqrt{1+\frac{1}{R^2}\left(\frac{\partial R}{\partial \theta}\right)^2}} \cdot n_\theta = \frac{-\frac{1}{R}\frac{\partial R}{\partial \theta}}{\sqrt{1+\frac{1}{R^2}\left(\frac{\partial R}{\partial \theta}\right)^2}} \qquad (21c)$$

Since Equation (21) is based on the potential flow expressions, it represents a slight overestimation of the viscous dissipation.

The decay time, τ, for the unforced motion is given by,

$$\tau = \frac{2\pi}{\omega} \cdot \frac{2 \cdot (\text{average energy stored})}{(\text{energy dissipated per cycle})} . \qquad (21d)$$

Here ω is the circular frequency of the vibration, and τ is the time in seconds for the amplitude of the oscillation to reach $1/\underline{e}$ of its original value.

EXPERIMENTAL PROCEDURES

MATERIALS

PURIFICATION OF THE MATERIALS

Sun Oil paraffin wax No. 5512 (m.p. 158-160°F.) was used in this work. The commercial product was further processed to remove any polar impurities by passing the molten paraffin through a steam-heated column of activated silica gel. The water used was triply distilled and stored in clean glass bottles. Matheson, Coleman, and Bell (No. 5089) 99.5% minimum assay glycerol was used in this work. It was further purified by double distillation under vacuum. Appendix I contains detailed descriptions for the purification procedures for these materials.

All glassware used in the course of this work was boiled for 4 hours in a cleaning solution of sulfuric acid saturated with sodium dichromate, thoroughly rinsed with triply distilled water, and dried in a clean oven.

PHYSICAL PROPERTIES OF THE LIQUID MIXTURES

Mixtures of 40.00, 57.51, 74.69, and 85.00% by weight of glycerol in water were weighed on a double pan balance. The viscosities of the mixtures were measured at 23.5°C. using a Hoppler falling ball viscometer. Refractive indices of the mixtures were measured at 20.0°C. with an Abbe Refractometer. Surface tensions of the mixtures were measured with a DeNouy Interfacial Tensiometer at 23.5°C. The appropriate corrections were applied to the experimental surface tension values for the ring size of the instrument and the density of the liquids. The densities of the mixtures were measured at 23.5°C. by weighing 100-ml. volumes.

APPARATUS

THE DRIVE CIRCUIT FOR DROP OSCILLATION

The vibration of the liquid drops was forced by driving a steel platform with an electromagnetic coil. The basic circuit contained an audio-oscillator, an amplifier, and the electromagnetic coil. The amplifier gain was 20% open. The amplitude of the impulse was then controlled from zero to 100% of this gain with the rheostat on the audio-oscillator. An oscilloscope was connected in parallel with the vibrating coil to determine the purity of the sine wave impulse to the coil. For frequencies of 20 to 400 cycles per second (c.p.s.) the impulse was a nondistorted sine wave at amplitudes of 65% or less. The experimental work was all done well within these limits.

A short circuit switch was placed across the coil to stop the impulse rapidly for studying the damping behavior of drops. (The current from the main circuit was simultaneously passed through an equivalent resistance.) The details of the drive circuit are in Appendix II.

THE DRIVE COIL AND R.H. CONTROL CHAMBER

The electromagnetic drive coil was made by wrapping a soft iron core with 1/2 pound of number 24 polyethylene-coated copper wire. The coil and core were mounted in a vertical position between two brass plates. A lucite box was placed around the exposed top of the soft iron core. An annular pad of urethane foam was glued around the top of the core. A 1/4-inch steel platform rested freely on this pad leaving a narrow gap between the platform and the core. The steel platform was fitted with small brass screws and straps. These straps were used to secure brass molds containing smooth paraffin surfaces.

The lucite box was used as a control chamber for relative humidity (R.H.). Early in the work it was noted that the small oscillating drops evaporated very rapidly at all but very high relative humidities. The R.H. chamber had a small stoppered hole in the top for placing the small drop on the paraffin surface at filming time. The R.H. was controlled by placing wet filter paper on the chamber floor and placing about 100 control drops in the chamber. The R.H. reached 99+% in 3.5 hours, and this was the time selected to age the chamber before each run. After this time, saturation was reached and the walls of the chamber became cloudy. Two sides of the chamber had optical glass surfaces to facilitate filming of the drops. Figure 1 shows the design of the coil and R.H. chamber. Details of the coil, the evaporation rate of small vibrating drops, and the R.H. equilibration curve for the chamber are in Appendix II.

HIGH-SPEED AND STILL-FILMING SETUPS

A high-speed camera was mounted on a concrete base. The coil and R.H. chamber were mounted on a separate base which was carefully leveled and insulated against extraneous vibrations. The optical system used for the high-speed filming was a horizontally mounted microscope. An extension was added to the microscope barrel to increase the focal length. The optical system was stationary. Focusing on the object was done by moving the object into the focal plane. This was easy to do since the coil and R.H. chamber were further mounted on a small 3-dimensional adjusting table. The optics system contained a very fine crosshair which was used to reference the edge of the paraffin surface. Light was supplied by a filament lamp behind the object. The still photography used essentially the same system. In this case, a micro-ipso and Leica camera were installed in the barrel of the microscope. Appendix II contains the details of the photographic setup and the lighting arrangements that were used.

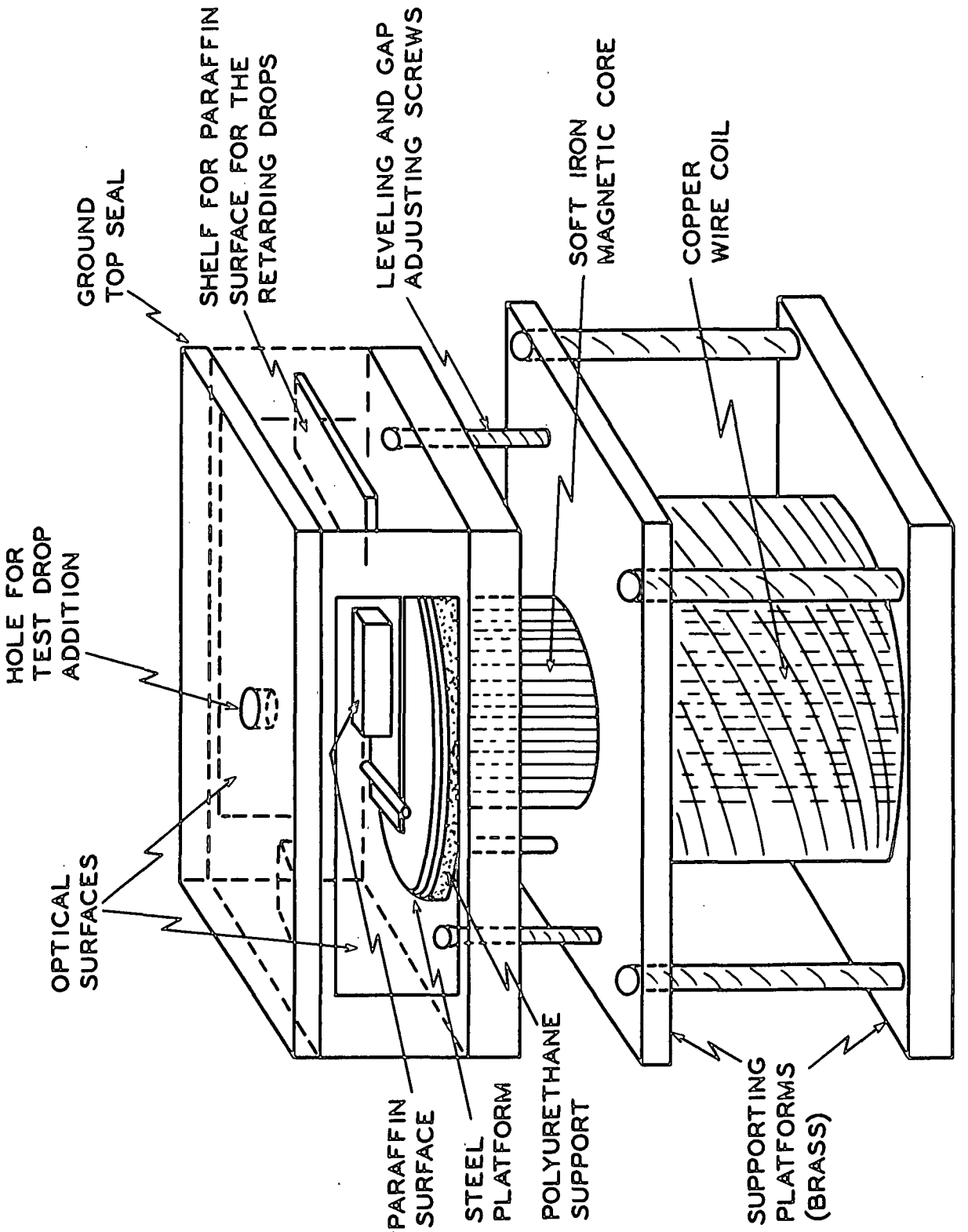

Figure 1. Design of the Drive Coil and the R.H. Chamber

FILMING PROCEDURES

PREPARATION FOR FILMING

Smooth paraffin surfaces were prepared by molding them against clean ferrotype plates. The paraffin was heated to slightly above its melting point. The molten paraffin was then poured into a small brass mold on a ferrotype plate. The mold and plate were heated slowly to the paraffin melting point, and then allowed to cool slowly at room temperature. Complete details of this procedure are in Appendix III. The mold was then broken from the ferrotype plate exposing a smooth paraffin surface for immediate use. The method produced good surfaces $\sim$ 30% of the time.

The mold and fresh paraffin surface were attached to the steel platform and placed in the R.H. chamber above the drive coil. The drive coil, chamber, and platform were very carefully leveled prior to each run to insure vertical symmetry of the oscillation. Wet strips of filter paper were placed in the chamber. About 50 water droplets were placed on each of two similar paraffin surfaces at each side of the R.H. chamber. The top was sealed on the chamber, and 3.5 hours were allowed for very high R.H. to be established. A small drop was introduced at the end of a clean microdropper through the small stoppered hole in the top of the R.H. chamber and placed on the smooth paraffin surface. The temperature of the chamber was recorded. At this time, the system was ready for filming. The test drop was used immediately for one film trial (i.e., oscillation, or damping, or equilibrium). However, each surface conditioned in the R.H. chamber in this manner could be used for as many as 3 or 4 film trials by placing a fresh test drop in a different position on the surface. The number of film trials obtained from a conditioned surface depended on the time used in loading the film, and if there was any measurable temperature rise due to lighting.

TYPES OF FILMS TAKEN

High-speed films were taken of the regular steady-state oscillation of the test drops in the ellipsoidal mode of deformation. This was done by turning on the filament lamp briefly, focusing on the drop, adjusting the audio-oscillator frequency and amplitude to determine the resonance frequency of the drop and the necessary input to force the oscillation. The lamp was immediately turned off and the audio-oscillator input turned to zero. The viewing eyepiece (used for focusing) was removed from the high-speed camera. A black photographer's cloth was draped over the entire photographic system from lamp to camera. The lamp was then turned on, the input amplitude restored to the determined value, the high-speed film was taken, and the lamp and input amplitude were turned off. This procedure was repeated for several more test drops until a measurable temperature rise was noted ($\sim$ 0.5°C.) in the R.H. chamber.

The high-speed filming of the damping of drop oscillation was done using the same procedure. In this case, the short circuit switch across the drive coil was triggered approximately in the middle of the 100 feet of film passing through the high-speed camera (i.e., at 5000 f.p.s. this was about 1/4 second after triggering the camera). The input to the drive coil was stopped rapidly by the short circuit, and the damping behavior of the drops was captured on film.

The equilibrium pictures were also taken in a similar manner. The drop was focused and vibrated for a time equivalent to the vibration time in the oscillation and damping filming. This was done to insure that the equilibrium drops had experienced the same conditions as the dynamic drops. The input was then stopped and the equilibrium picture taken using a micro-ipso and Leica camera.

Finally, at the completion of each filming run, a high-speed film or equilibrium pictures (as the case might be) were taken of a 0.01, 0.1 mm. stage micrometer

placed in the focal plane. This provided a reference of the absolute dimensions of the drops, and a check from run to run on any differences in the dimensional stability of the films during developing.

A complete description of filming conditions (lighting, voltages, shutter speeds, types of film, etc.) is in Appendix III.

MEASUREMENT TECHNIQUES

DIMENSIONS AND TIMES

A microcomparator with an IBM data punch output was used to measure the shapes of the drops and the distance separation of the 1/1000 second marks on the developed films. For the steady-state oscillation drops, portions of the high-speed films were sectioned in 20 frame pieces and mounted on glass plates. Enough footage was selected from each film to cover 4 periods of the drop oscillation. About 80 frames per 4 periods of oscillation were measured on each film. The footage selected for measurement was taken from a depth in the reel at which the camera had achieved constant speed. On each frame measured, the coordinates of the drop edge were punched first, the origin second (determined by taking the midpoint between the drop edges), the drop top third, followed by 17 more sets of coordinates around 1/2 of the drop's surface outline. These data were then stored in punched IBM data card form with the sequence of the oscillation preserved.

The time was obtained using the microcomparator to measure the distance between the 1/1000 second marks for a film and an average frame length for that film.

Damping films were measured in a similar manner on the microcomparator. The individual frames selected for measurement were those with the maximum amplitude. The time was determined by measuring the 1/1000 second separations, frame length, and the number of frames between maximum amplitudes.

Equilibrium drop shapes were measured using 40 coordinate sets around 1/2 of the drop's surface outline. This information was used to determine drop volumes and gravitational effects on drop shape.

The 0.01, 0.1-mm. stage micrometer reference films were measured with the microcomparator. This determined the conversion of microcomparator units to c.g.s. units. Also, it provided a dimensional stability check on the films themselves.

The details of the microcomparator measurements and the data storage are in Appendix III.

CONTACT ANGLES

All contact angles were measured using a tangentometer-protractor device designed for this study. This device (Appendix III discusses the design) allowed the matching of the curvature of the drop at the contact point with the reflected image in a vertical mirror. A direct reading of the contact angle was obtained. The high-speed films and equilibrium films were projected on a microfilm reader. The contact angle measurements were made on these projections. The contact angle measurements were made on the same frames measured with the microcomparator.

EXPERIMENTAL RESULTS

PHYSICAL PROPERTIES OF THE GLYCEROL-WATER MIXTURES

The experimental physical properties of the glycerol-water mixtures agreed very closely with available literature values (41, 42) at the appropriate temperatures. Table I shows the weight percent glycerol in water based on the weighing up of the mixtures and the average weight percent glycerol of the mixtures based on comparison of the measured physical properties (refractive index and viscosity) with literature values. Also included in Table I are the experimentally determined viscosities at 23.5°C. Figure 2 shows the experimental values of refractive index, surface tension, and density plotted versus composition. It can be noted that all these properties follow the same behavior. There is a slight deviation from ideal behavior, but the behavior is quite regular.

TABLE I

WEIGHT % OF GLYCEROL IN WATER
AND THE VISCOSITIES OF THE MIXTURES

Wt. % Glycerol Based on Weighing Up	Wt. % Glycerol Based on the Physical Properties	Viscosity at 23.5°C., cp.
0.00	0.00	1.0
40.00	40.32	3.6309
57.51	57.93	8.4123
85.00	85.17	89.582
100.00	100.00	1130.0 (23.0°C.)

A complete description of the measurement techniques and the data for the physical properties of the liquid mixtures are found in Appendix I.

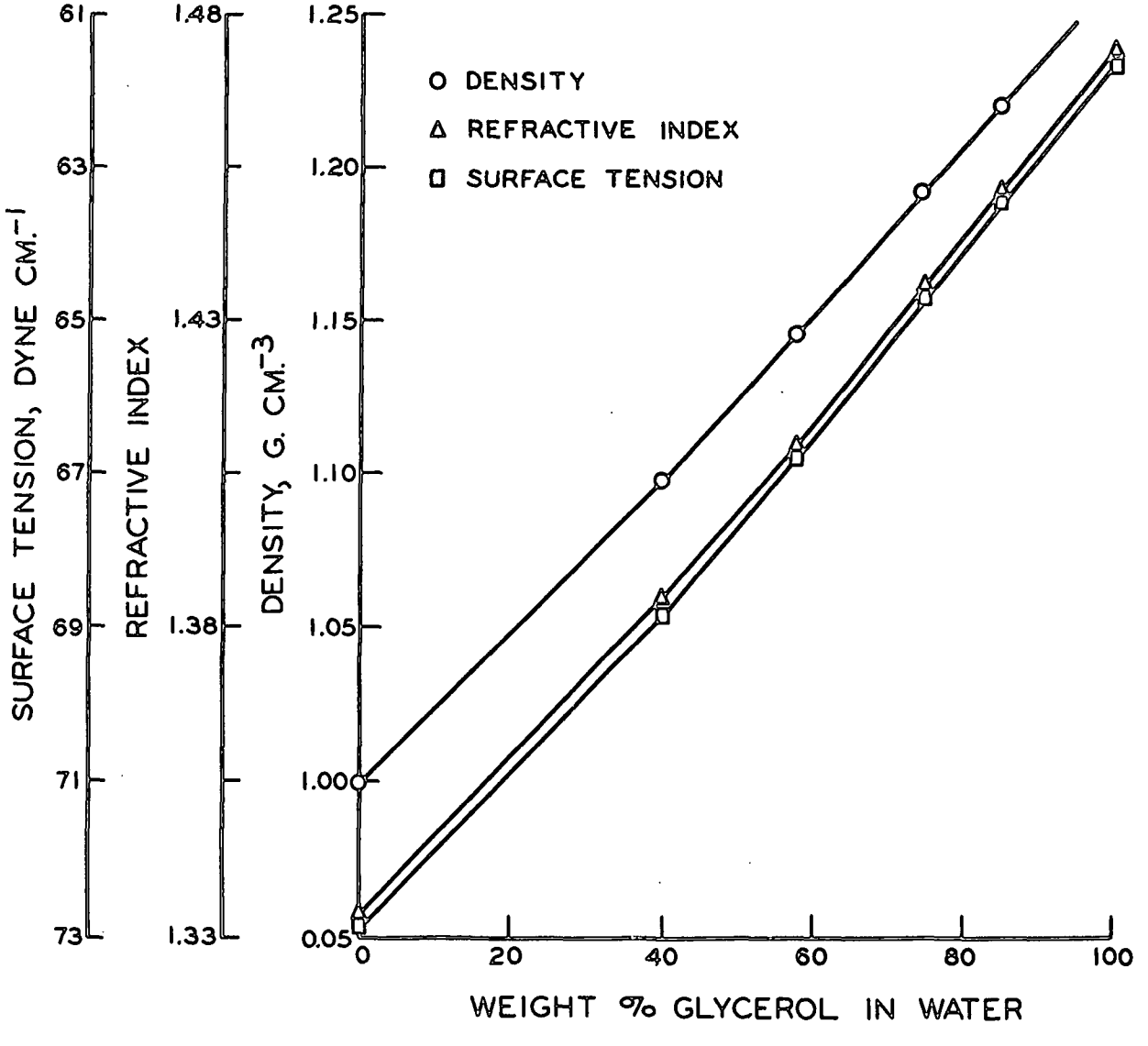

Figure 2. Physical Properties of the Mixtures

EQUILIBRIUM DATA

EQUILIBRIUM CONTACT ANGLES OF THE MIXTURES ON PARAFFIN

Contact angles were measured from pictures taken of equilibrium drops of the different liquid mixtures on smooth paraffin surfaces. The complete data are presented in Appendix IV. Table II summarizes the average equilibrium contact angles for each mixture on paraffin.

TABLE II

AVERAGE EQUILIBRIUM CONTACT ANGLES OF THE GLYCEROL-WATER MIXTURES ON PARAFFIN AT 23.5°C.

Wt. % Glycerol in Water	Average Contact Angle, °
0.00	106.5 ± 0.5
40.32	100.2 ± 0.8
57.93	97.0 ± 0.5
75.13	94.5 ± 0.0
85.17	93.0 ± 0.0
100.00	91.0 ± 0.5

THE PARAFFIN SURFACES

Electron micrographs, at different magnifications, were taken of the molded paraffin surfaces. Inspection of these pictures indicated that the paraffin surfaces were quite smooth and continuous. The surface asperities were of very small elevation compared to the dimensions of the liquid drops. Figure 3 shows a typical electron micrograph of a paraffin surface replica magnified 29,500 times and shadowed at an angle of 30°.

Magnification 29,500X

Figure 3. Electronmicrograph of a Smooth Paraffin Surface

DYNAMIC DATA

SELECTION OF HIGH-SPEED FILMS

Certain high-speed films of the oscillation of drops were selected for analysis from the large group taken. These films were selected on the basis of overall clarity of the drop outline and the sharpness of the drop outline at the contact point. A sufficient number of films were measured to obtain information describing the behavior of the different mixtures. Table III is a summary of the films that were analyzed and the type of measurements that were made on these films.

STEADY-STATE OSCILLATION

Dynamic Contact Angles

Dynamic contact angles were measured from the high-speed films using the contact angle tangentometer discussed earlier. The measurements covered four successive periods of oscillation on each film. The dynamic contact angles were plotted versus time. In every case, the plots were found to be sinusoidal and 180 degrees out of phase with the motion of drop's top. There was no measurable hysteresis of the dynamic contact angles. The complete dynamic contact angle data are in Appendix IV. The median values and the amplitudes of the dynamic angle changes for all the drops are shown in Table IV. Figure 4 shows the filmed outline of a drop at its maximum up and down positions and its median position. The large contact angle changes can readily be observed. Figure 5 presents a typical set of dynamic contact angle data relative to the other characteristics of the drop motion.

Drop Shape Changes

Reference Film Measurements

As shown in Table III, high-speed films of a 0.1, 0.01-mm. stage micrometer were taken at different times during the course of filming all the drops used in

TABLE III

SUMMARY OF THE CONTENTS OF THE HIGH-SPEED FILMS AND THE TYPE OF MEASUREMENTS MADE ON THE FILMS

Subject Matter of Films	High-Speed Film Number	Type of Measurements
Oscillation of water drops	17,18,20,21 33,34,36,73	Microcomparator shape and dynamic contact angles
Oscillation of 40.32% glycerol drops	41,43,45	"
Oscillation of 57.93% glycerol drops	53,54,56,61, 63,65	"
Oscillation of 75.13% glycerol drops	77,82	"
Oscillation of 85.17% glycerol drops	79,81	"
Oscillation of 75.13% glycerol drops	48,50,78	Dynamic contact angles
Oscillation of 85.17% glycerol drops	58,66,80	"
Damping of water drops	35,37,39,72,74	Microcomparator shape on max. amplitude frames
Damping of 40.32% glycerol drops	42,44,46	"
Damping of 57.93% glycerol drops	53,55,57,62,64	"
Damping of 75.13% glycerol drops	49.51	"
Damping of 85.17% glycerol drops	59.67	"
0.01, 0.1-mm. stage micrometer reference scale	23,30,40,47,60, 68,76	Microcomparator units per mm.
Second observable mode of vibration of a water drop	75	None

TABLE IV

MAXIMUM, MINIMUM, AND MEDIAN VALUES
OF THE SINUSOIDAL CONTACT ANGLE CHANGES

High-Speed Film Number	Composition of Drop	Median Dynamic Contact Angle, °	Range of Contact Angle Changes, °
17	H_2O	105.0	115-95
34	"	105.5	119-92
18	"	104.5	119-90
20	"	107.0	122-92
33	"	105.8	117-94.5
36	"	106.0	121-91
21	"	107.0	122-92
73	"	105.0	116-94
41	40.32% wt. glycerol in H_2O	100.0	111-89
45	"	102.0	113-91
43	"	101.0	110-92
56	57.93%	96.0	107-85
61	"	96.5	107-86
53	"	96.0	107-85
63	"	96.5	108-85
54	"	97.0	107-87
65	"	96.0	106-86
77	75.13%	95.5	106-85
82	"	95.8	105.5-86
48	"	95.5	106-85
50	"	97.0	105-89
78	"	95.5	105-86
79	85.17%	95.0	102-88
81	"	95.5	102-89
58	"	96.0	105-87
66	"	94.5	103-86
80	"	95.0	103-87

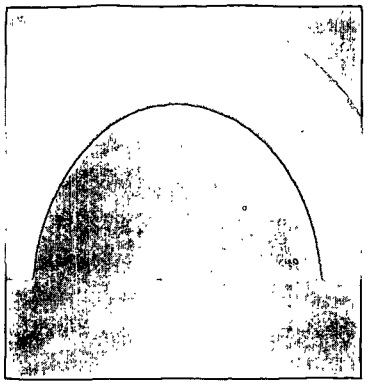

Up Position
$(\omega t) = \pi/2$

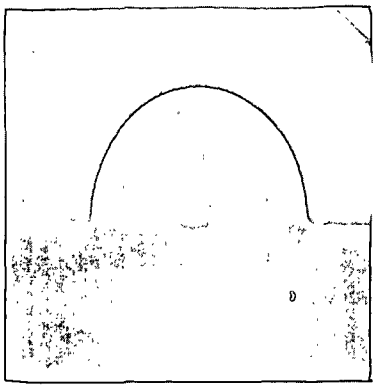

Film 21

Film 34

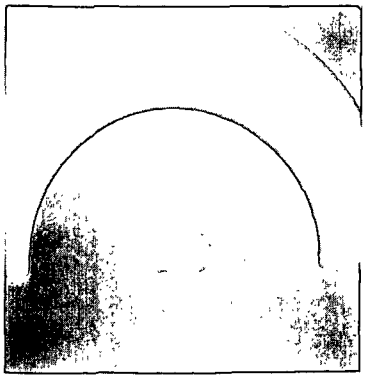

Median
Position
$(\omega t) = \pi$

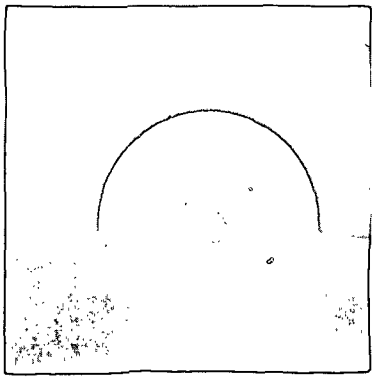

Film 21

Film 34

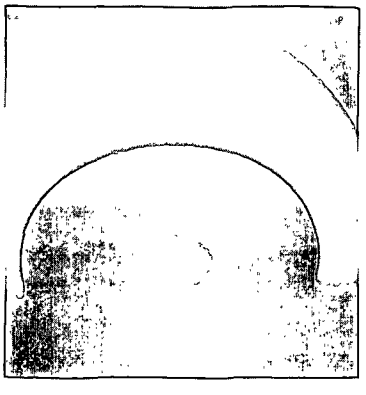

Down Position
$(\omega t) = 3\pi/2$

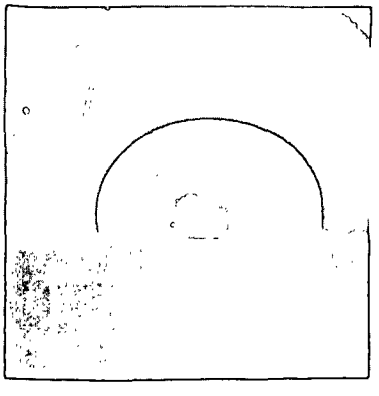

Film 21
Water Volume = 5.49 MM.^{3}

Film 34
Water Volume = 2.03 MM.^{3}

Enlarged 8.5X

Figure 4. Frames from High-Speed Films Showing the Up, Median, and Down Positions

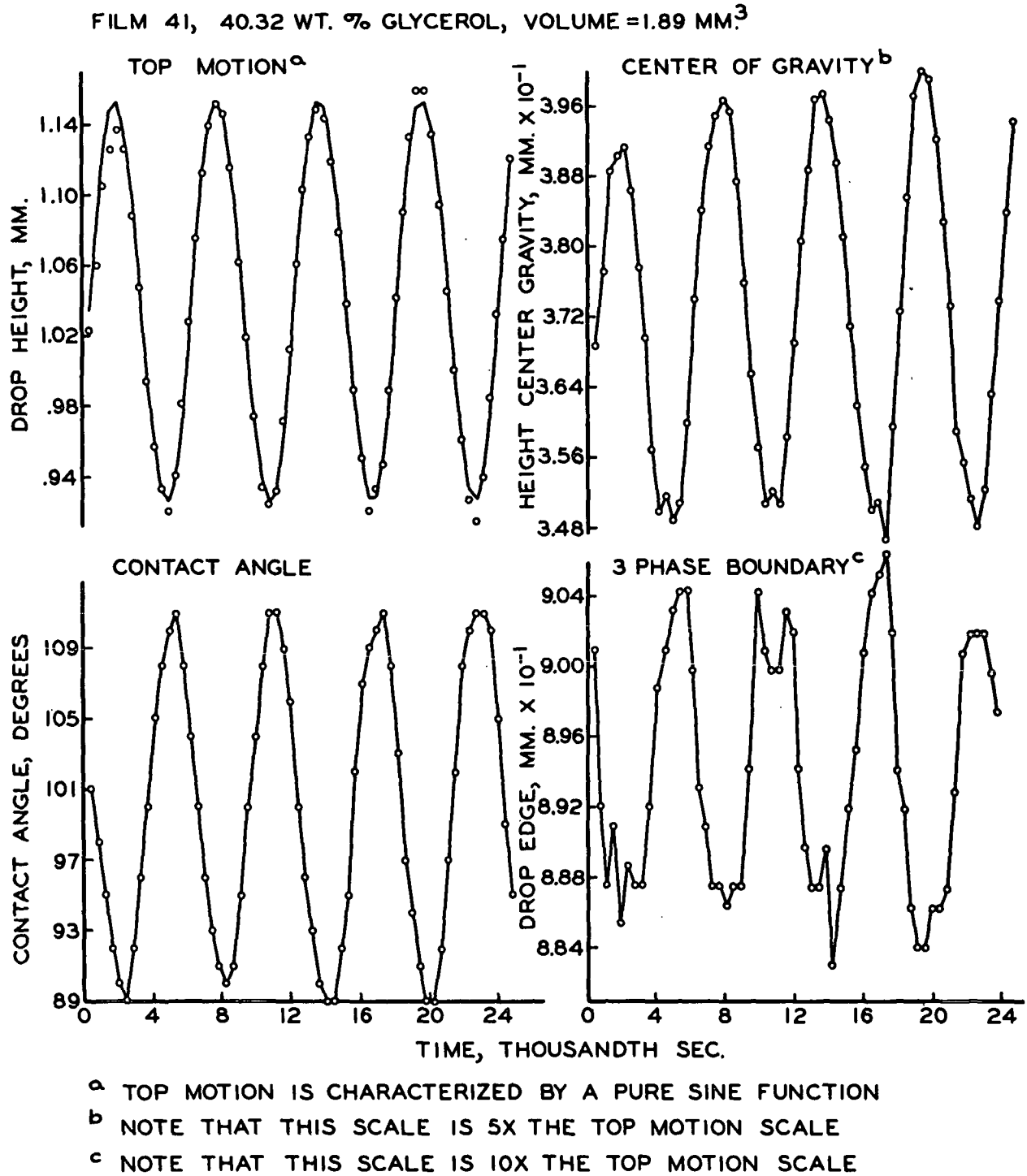

Figure 5. Experimental Characteristics of Drop Oscillation Relative to Time

this study. These films served three purposes. First, they provided an absolute scale reference to convert microcomparator measurements into CGS units. Second, they gave an indication of the dimensional stability of the films themselves. This was important since the films were developed in batches of about five films. Finally, they provided an estimate of the error in the microcomparator measurements within a given film and from one film to another. The error analysis will be pursued in detail in a later section.

Appendix IV contains the complete data from reference film measurements. For all the films taken through number 76, the optics of the filming setup were unchanged. The absolute scale measured for these films was 895.7 microcomparator units per mm. This measurement included the magnification of the camera optics and the microcomparator. For the films from number 77 on, the camera optics were changed slightly. These included the films of the 75 and 85% glycerol-water mixtures. The absolute conversion measured for these films was 1064.7 microcomparator units per mm.

Vibrational Frequencies and Drop Top Motion

The vibrational frequencies of the drops were determined by plotting the motion of the top of the drops versus time. The microcomparator data of the drop shape changes with time were normalized relative to the origin using appropriate computer programs. The time function was determined from 10^{-3} second marks on the side of the film. The distance between these markings was measured on the microcomparator. The average frame length was measured, and the time in frames per second was readily calculated for each film. These data are in Appendix IV.

Again, utilizing appropriate computer programs, the drop top motion was plotted versus time. In all cases, the motion of the drop top was found to be sinusoidal. Best fit sine curves were applied to the top motion of all the drop data. The

vibrational frequencies of the drops and the phase angle of the beginning of the data were determined. The vibrational frequencies of all the drops are summarized in Table V.

The motion of all the drop tops fit sinusoidal curves very closely. The amplitudes of this motion are summarized in Table V. The plotted values for a typical drop are shown in relation to the other characteristics of drop oscillation in Fig. 5.

Three-Phase Boundary Motion

The normalized data drop shape data measured the motion of the drop's edge in contact with the solid surface. Error analysis of the microcomparator data (discussed later in this paper) indicated the possible error in the measurements of this motion could be large since the motion was quite small. However, these measurements were considered to be an estimate of the drop edge motion.

The edge motion observed in the data was also, approximately, sinusoidal and 180 degrees out of phase with the motion of the top of the drops. The amplitudes of this motion for the drops were summarized in Table V. A typical set of such data and its relation to the other characteristics of drop motion was shown in Fig. 5.

Volumes and Gravitational Motion

The drop volumes were integrated from the experimental data from each frame and averaged for each drop. The averaged volumes for the drops were summarized in Table V.

The experimental gravitational motion for a drop was obtained by once again integrating each frame of data and determining the center of gravity for the frame. This information was then plotted versus time. In every case, the gravitational motion was approximately sinusoidal and in phase with the motion of the drop's top.

TABLE V

SUMMARY OF THE EXPERIMENTAL CHARACTERISTICS OF THE MOTION OF THE STEADY-STATE OSCILLATING DROPS ON PARAFFIN SURFACES

Film Number	Mixture	Volume, $mm.^3$	Gravitational Amplitude, mm.	Drop Edge Amplitude, mm.	Drop Top Amplitude, mm.	Vibrational Frequency, c.p.s.
17	H_2O	0.88	2.28×10^{-2}	0.46×10^{-2}	8.70×10^{-2}	245.0
34	"	2.03	2.21	0.68	9.82	165.1
18	"	2.13	3.70	1.04	15.07	158.0
20	"	3.27	2.21	1.08	17.29	130.5
36	"	4.01	4.60	1.10	19.13	118.8
33	"	4.31	3.20	1.00	13.63	114.0
21	"	5.49	4.28	1.04	18.38	103.5
73	"	6.45	2.94	0.90	18.20	97.8
41	40.32 wt. % glycerol	1.89	2.58	0.78	11.46	168.8
45	"	2.95	2.59	0.51	11.44	132.0
43	"	6.42	2.60	0.58	13.10	97.8
56	57.93 wt. % glycerol	2.20	2.05	0.42	9.99	149.9
61	"	2.46	1.92	0.28	9.85	143.7
53	"	3.66	2.36	0.76	14.93	119.5
63	"	4.26	2.48	0.39	14.30	117.3
54	"	6.69	2.29	0.46	12.56	94.5
65	"	7.09	2.56	0.42	14.02	89.4
77	75.13 wt. % glycerol	3.12	1.92	0.40	11.39	117.1
82	"	3.79	2.30	0.56	12.07	117.1
79	85.17 wt. % glycerol	6.34	1.17	0.40	8.82	85.0
81	"	8.05	1.75	0.40	9.80	73.6

The magnitude of the gravitational amplitude was about 10% of the amplitude of the drop top motion. These experimental gravitational amplitudes were summarized for all the drops in Table V. A typical plot of the experimental gravitational motion in relation to the other drop motion characteristics was shown in Fig. 5.

Modes of Vibration

The mode of vibration of the drops measured in this study was the first excitable mode. This is the mode described as ellipsoidal deformation. Higher pure modes of vibration were observed and photographed. However, microcomparator measurements were not made on these films. Figure 6 shows the two extreme forms of the oscillation for the first three modes of vibration of an approximately 12 $mm.^3$ water drop at 60, 122, and 242 cycles per second, respectively. Figure 6 also shows the photographed outlines of a drop in the second mode of vibration. The outline of this mode can be contrasted with the photograph of the first mode shown earlier in Fig. 4.

DROP DAMPING DATA

The high-speed films of drop damping were measured with the microcomparator. The shape was measured to determine the drop volumes and the decreasing amplitude of the motion of the drop top. The time function was determined from the 10^{-3} second marks on the films. The decaying amplitude of the drop top motion was plotted versus time. The experimental decay time, τ, (43) of a particular drop was taken as the time in seconds in which the amplitude of the drop's top motion decreased to 1/e of its original value (e is the base of natural logarithms). Figure 7 shows a typical amplitude decay plot. Table VI presents the decay times obtained for the drops of the different liquid mixtures obtained in this study.

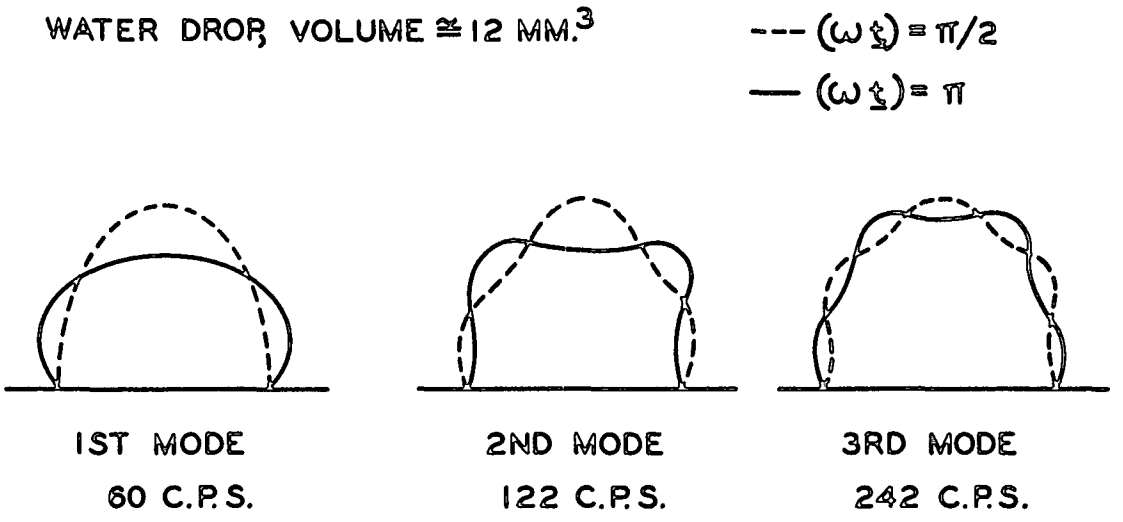

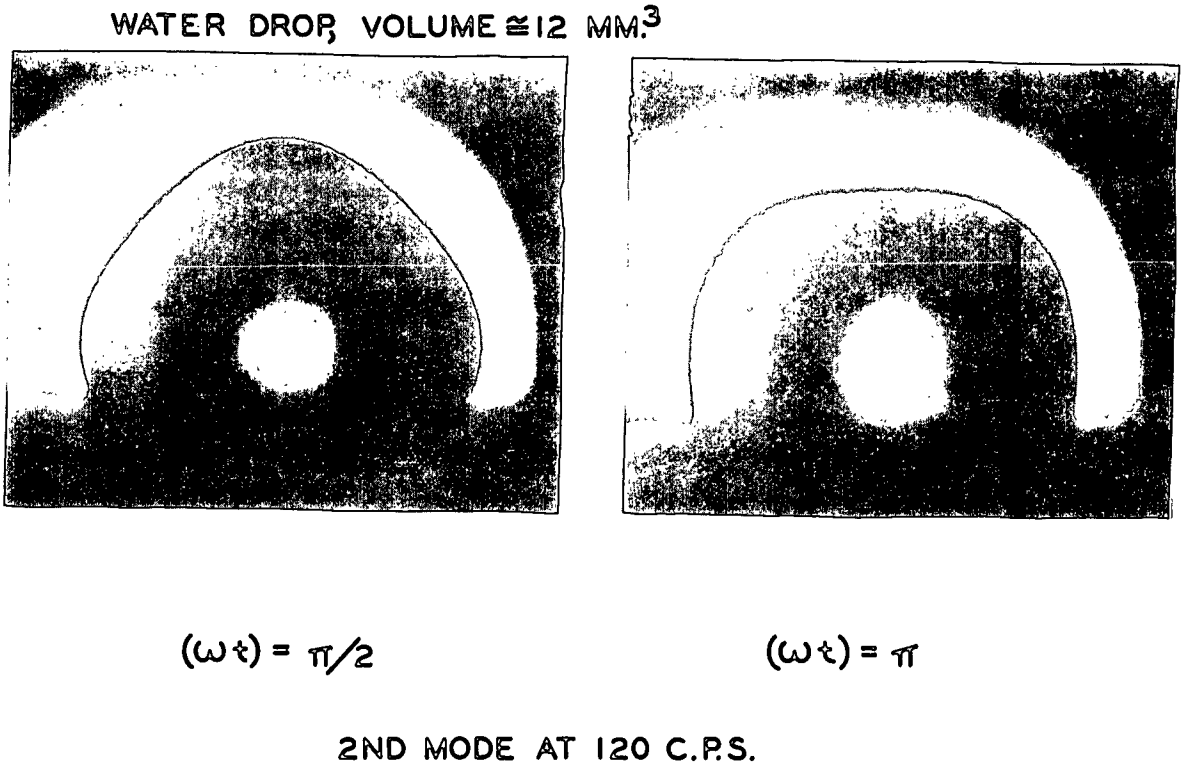

Figure 6. Modes of Vibration of a Water Drop on a Paraffin Surface

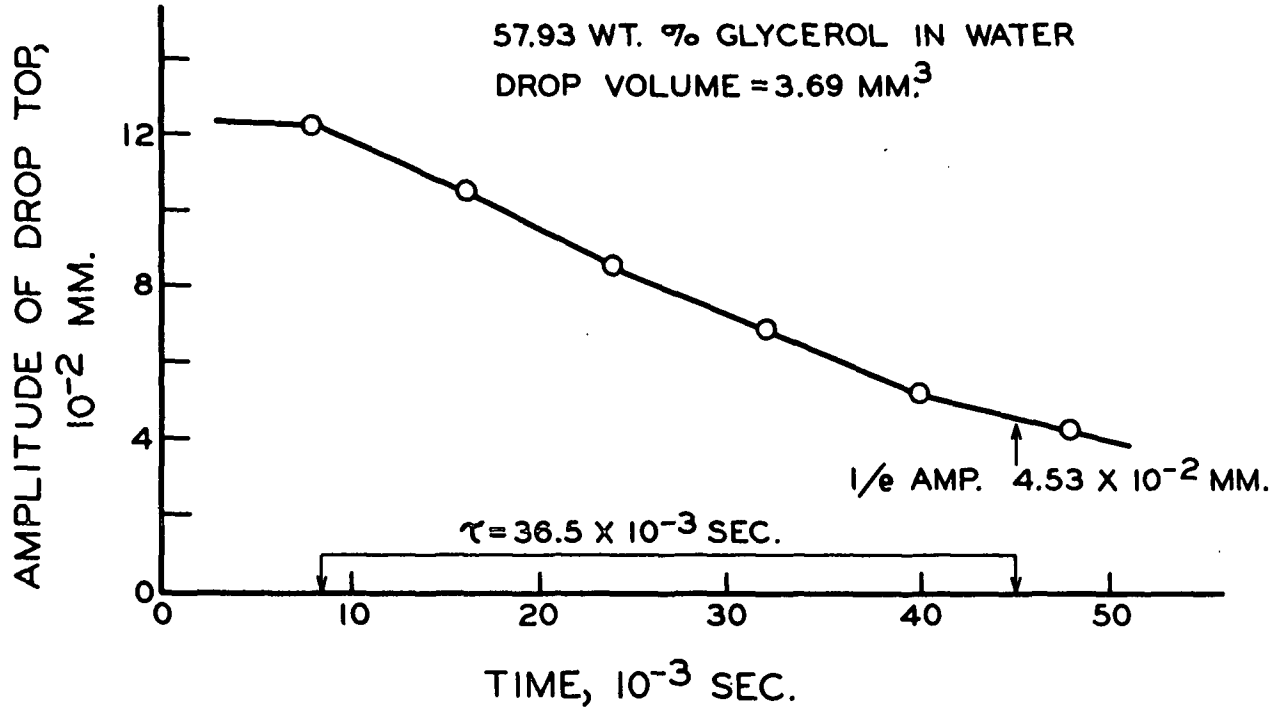

Figure 7. Experimental Damping Curve for Film 53

TABLE VI

EXPERIMENTAL DECAY TIMES FOR THE DROPS OF GLYCEROL-WATER MIXTURES OSCILLATING ON A PLANE SURFACE

Film Number	Mixture	Volume, $mm.^3$	Experimental Decay Time, x 10^{-3} sec.
35	H_2O	2.03	85.0
37	"	3.80	92.0
72	"	4.45	100.0
39	"	6.07	101.0
74	"	6.40	110.0
42	40.32% wt. glycerol	1.92	22.0
46	"	2.94	37.0
44	"	6.29	58.0
57	57.93% wt. glycerol	2.36	24.5
62	"	2.61	24.0
53	"	3.69	36.5
64	"	4.43	43.0
55	"	6.89	40.0
49	75.13% wt. glycerol	5.87	22.0
51	"	9.07	32.0
59	85.17% wt. glycerol	7.59	13.0
67	"	8.93	13.0

ERROR ANALYSIS

Contact Angles

The accuracy of the contact angle tangentometer was determined by making a series of measurements on constructed contact angles of different values. These constructed angles covered the range of angles measured for the drops in this study. Angles were constructed by intersecting the outline of a circle with straight lines to give angles of approximately 60, 70, 80, 100, 110, and 120 degrees. A series of ten measurements was made with the tangentometer device on each of these constructed contact angles. The instrument is scored at 0.5 degree intervals. The contact angles were estimated to tenths of a degree.

The standard deviation of the individual groups was determined. The accuracy of the device was found to be somewhat better for contact angles less than 90°. The overall standard deviation of the groups was found to be $\pm$ 0.19° contact angle. The average contact angles, as measured with the device, agreed extremely well with the geometric values determined by measuring the arc length of the circle between the base line of the contact angle and a parallel line through the origin of the circle. These results are summarized in Table VII. The complete data are in Appendix IV. The contact angle device was found to be a very accurate instrument. The measurements on constructed contact angles indicated that the error introduced in the measurement of the contact angles of the liquid drops on paraffin was in the neighborhood of $\pm$ 0.2°.

Microcomparator Measurements

The data from the reference films were discussed earlier in connection with the determination of the absolute scale in CGS units for the high-speed films. The complete data from the measurement of the filmed stage micrometers are in Appendix IV. The variations of the individual measurements within a given film, and from film to film, were used to make error estimates for all data taken with the microcomparator.

TABLE VII

SUMMARY OF MEASUREMENTS WITH THE CONTACT ANGLE TANGENTOMETER ON CONSTRUCTED CONTACT ANGLES

Average Contact[a] Angle Measured with Tangentometer, °	Standard Deviation	Angle Determined by Arc Intercepted, °
62.37	± 0.12	62.4
70.73	± 0.14	70.7
81.35	± 0.22	81.2
101.31	± 0.21	101.2
110.65	± 0.20	110.5
120.87	± 0.20	120.8

Overall Standard Deviation = ± 0.19 degree

[a]Average of ten measurements to the nearest tenth degree.

The average conversion factor based on all the reference films was 895.7 micro-comparator (mc.) units per mm. The standard deviation of this average was ± 6.02 mc. units. This indicated a maximum error in length measurements of 0.67%. This error included the contributions of error in measurements within a given film and error between films due to differences in the dimensional stability during developing.

The average standard deviation of the measurements in a given film was ± 2.48 mc. units. This gave an error of 0.28% for length measurements in mc. units within a given film. An error of 0.28% in a length measurement could give rise to an error of 1.0 to 2.0% in the amplitude of the motion of a given drop's top (depending on the size of the drop and the amplitude). Since there was an error of 0.68% in the conversion factor, this could lead to an error of 1.0% in the absolute dimensions of a given drop. This would result in an error of 5.0 to 10.0% in the absolute c.g.s. dimensions of the amplitudes of drop top motion.

The measured amplitudes of the motion of the three-phase boundary were small (about 10%) relative to the motion of the drop top. In c.g.s. units, the estimated error could be as high as 50.0 to 100.0% of the reported three-phase boundary amplitudes.

Based on the length error in absolute c.g.s. units, the error in the drop volumes was $\pm$ 3.0%. Based on the error in mc. units, the error in the measured time function was $\pm$ 0.6%.

The error analysis for the microcomparator measurements indicated that the information obtained from these measurements was extremely accurate in characterizing the nature of the drop oscillation. The exception to this generalization was the possibility of a very large error in the measurement of the very small amplitudes of the three-phase boundary motion.

COMPARISON OF DYNAMIC AND EQUILIBRIUM CONTACT ANGLES

The cosines of the average equilibrium contact angles (reported in Table II) and the cosines of the average of the median dynamic contact angle values (reported in Table IV) were plotted *versus* composition by weight of glycerol in water. This plot is shown in Fig. 8. This plot was quite close to linear for the equilibrium drops. The median values for the dynamic drops followed the same linear plot from zero to $\sim$65% glycerol in water. From 65 to 85% glycerol in water, higher values of the contact angle were obtained for the median dynamic contact angles than were found in the equilibrium case. These differences were small ($\sim$2.0 degrees) but were experimentally significant.

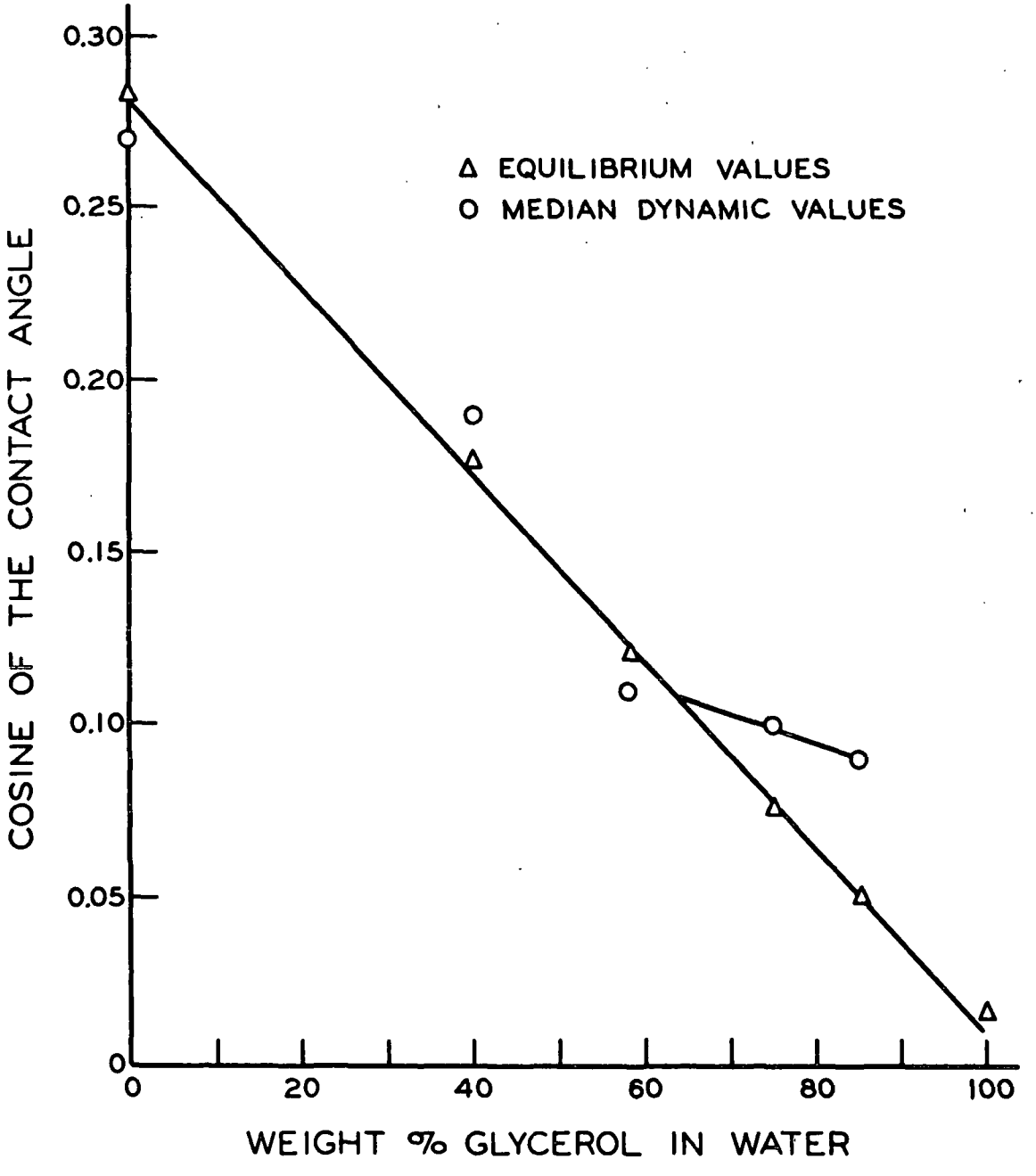

Figure 8. Cosine of the Equilibrium and Median Dynamic Contact Angles Versus Composition of the Drops

INTERPRETATION

The evaluation and results of the theoretical expressions included in the THEORETICAL CONSIDERATIONS section of this work are presented here. Comparisons are made with the data from the EXPERIMENTAL RESULTS section. Discussion of these comparisons and their implications are contained in the subsequent DISCUSSION OF RESULTS section.

INTERFACIAL ENERGIES

PARAFFIN SURFACE ENERGY

The surface energy of the paraffin surfaces was estimated using Zisman's critical surface tension determination (34). The cosines of the average equilibrium contact angles in Table II were plotted versus the surface tensions of the respective liquids. This plot is shown in Fig. 9. Extrapolation of cosine = 1.0 (zero contact angle) gave the approximate surface energy of the paraffin surfaces used in this study of 30.2 ergs $cm.^{-2}$ at 23.5°C. This value agreed well with literature values. [Phillips and Riddiford, in a review of literature values and techniques, have indicated the best value of paraffin surface energy at 20°C. is 33 ergs $cm.^{-2}$ (33).]

EQUILIBRIUM PARAFFIN-LIQUID INTERFACIAL ENERGIES

The surface energy of the paraffin surfaces in this study was determined as 30.2 ergs $cm.^{-2}$ at 23.5°C. This information was used with the equilibrium contact angles on paraffin and the surface tensions of the liquids to calculate the dispersion force contribution of the liquids to the paraffin-liquid equilibrium interfacial energy. This calculation was made according to Fowkes' method (32) using Equation (3). The calculated values at 23.5°C. are shown in Table VIII. The calculated values for water and 100% glycerol (22.6 and 30.7 ergs $cm.^{-2}$) agreed quite well with literature values (21.8 ± 0.7 and 37.0 ± 4 ergs $cm.^{-2}$) at 20°C. (44).

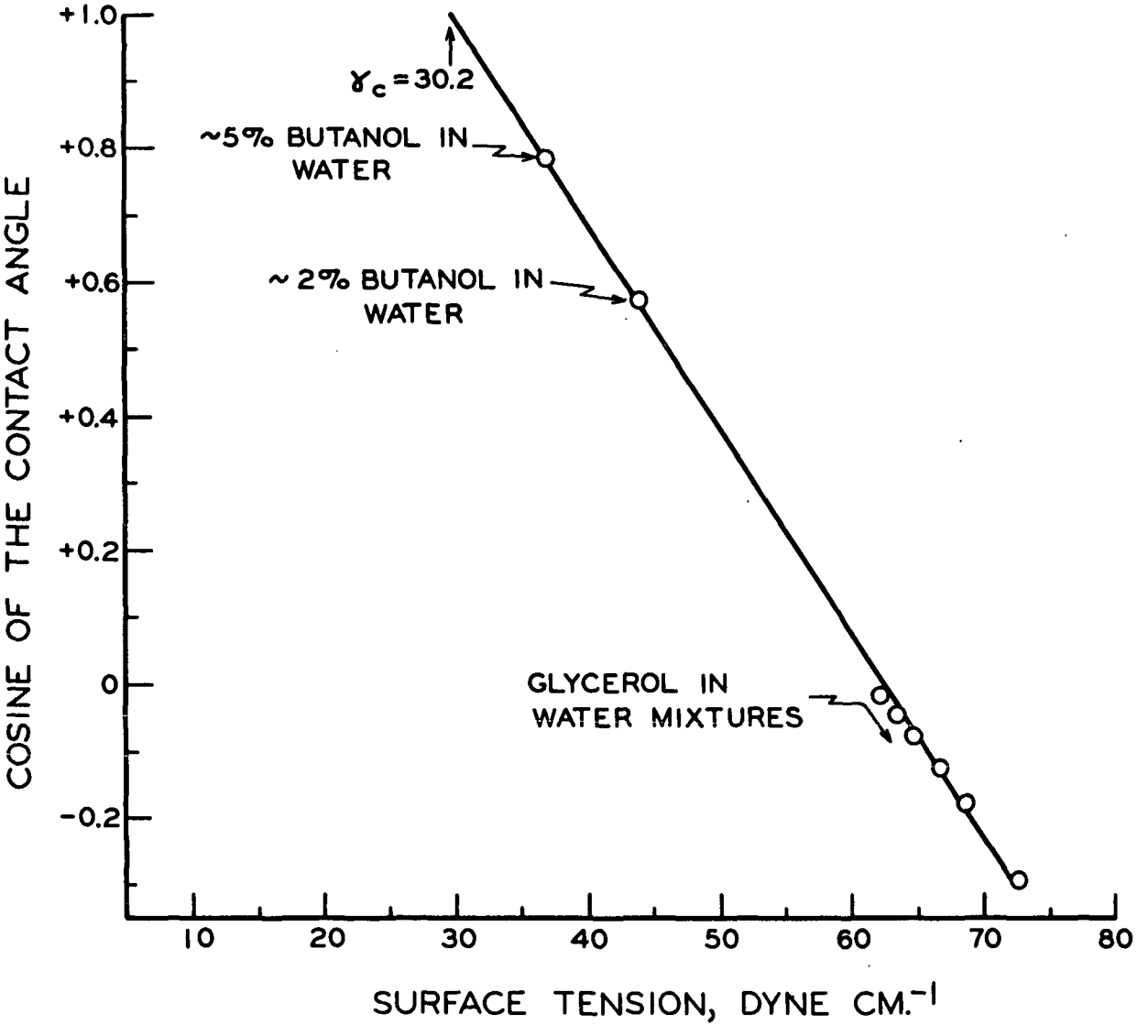

Figure 9. Critical Surface Tension Plot for the Mixtures on Conditioned Paraffin Surfaces at 23.5°C.

Equation (2) was used to calculate the total paraffin-liquid equilibrium interfacial energies for the different liquids on paraffin at 23.5°C. These values are also shown in Table VIII.

TABLE VIII

CALCULATED EQUILIBRIUM PARAFFIN-LIQUID INTERFACIAL ENERGIES (γ_{ls}) AND THE LIQUID DISPERSION FORCE COMPONENTS FOR GLYCEROL-WATER MIXTURES ($\gamma_l^{(d)}$) AT 23.5°C.

Wt. % Glycerol in H_2O	$\gamma_l^{(d)}$, ergs $cm.^{-2}$	γ_{ls}, ergs $cm.^{-2}$
0.00	22.6	50.7
40.32	26.3	42.6
57.93	28.4	38.4
75.13	29.6	35.0
85.17	29.8	33.6
100.00	30.7	31.1

INTERFACIAL ENERGIES ASSOCIATED WITH THE DYNAMIC CONTACT ANGLES

The dynamic contact angles represented changes in the orientation requirements for liquid molecules in the three-phase boundary region. This was necessarily true since the dynamic contact angles represented a change in the direction of the liquid-vapor surface tension forces acting on the specific region of the contact point. The relaxation time of water molecules at liquid-solid interfaces (45) has been found to be very rapid ($\sim 10^{-6}$ sec.). The relaxation times for, at least, the lower percent glycerol mixtures should also be rapid. These times are very fast compared to the frequencies of drop oscillation in this study. Therefore, the liquid molecules in the three-phase boundary region should be able to "instantly" meet the orientation requirements placed on them at the boundary.

An estimate of the different energies associated with the liquid-solid interfacial area in the specific region of the three-phase boundary was obtained using the dynamic contact angles of the liquid drops oscillating on the paraffin surfaces and Equation (1) (Young's equation). The liquid-vapor interfacial energies and the

solid-vapor energies were assumed constant. The film pressure of the liquid on the solid was assumed to be zero. Maximum and minimum energies in the three-phase boundary were calculated for each mixture. This was done by using the average maximum contact angle and average minimum contact angle for all the drops of a given mixture. Median energy values were calculated based on the median dynamic contact angles for each mixture. These results were not specific for a given drop, but they did give the magnitude of the energy changes for each mixture.

The calculated results are presented in Table IX. The energy differences in the three-phase boundary between the maximum and minimum contact angles were very large for all the mixtures. The maximum values were approximately twice as large as the minimum values.

TABLE IX

MAXIMUM, MINIMUM, AND MEDIAN VALUES FOR THE ENERGY (ERGS/CM.$^{-2}$) OF THE LIQUID-SOLID INTERFACIAL AREA IN THE SPECIFIC REGION OF THE THREE-PHASE BOUNDARY CALCULATED ON THE BASIS OF THE DYNAMIC CONTACT ANGLES AND THE YOUNG EQUATION AT 23.5°C. FOR EACH MIXTURE

	Liquid-Solid Energy in the Three-Phase Boundary		
Mixture	Maximum (Drop Down), ergs cm.$^{-2}$	Minimum (Drop Up), ergs cm.$^{-2}$	Median, ergs cm.$^{-2}$
0.00	66.4	32.5	50.7
40.32	54.7	31.2	43.1
57.93	49.5	25.3	37.6
75.13	46.7	25.5	37.4
85.17	44.2	26.7	36.2

A comparison was also made between the energy values calculated for the median dynamic contact angles in Table IX using Young's equation, and the equilibrium values in Table VIII that were calculated using Fowke's (32) geometric mean of dispersion forces [Equation (2)]. These energy calculations agreed very closely for water,

40.32 and 57.93% glycerol in water. For the higher mixtures of glycerol in water, the dynamic median energies were slightly higher than the equilibrium calculations. This reflects the result observed in Fig. 8 that the median dynamic contact angles for the higher content glycerol mixtures were slightly higher than the equilibrium values.

EQUILIBRIUM DROP SHAPE DESCRIPTION

EVALUATION OF THE THEORETICAL EXPRESSION

Equation (6) was derived from the equation of capillarity and describes the shape of the sessile drop on a plane surface. Equation (6) is a second-order differential equation in polar coordinates where $\underline{R}''$ is a function of $\underline{R}$, $\underline{R}'$, and θ. Here θ is the angular displacement from the vertical axis, $\underline{R}$ is the radial coordinate describing the equilibrium liquid surface, and $\underline{R}'$ and $\underline{R}''$ are the first and second derivatives with respect to θ. This equation was readily adapted to numerical integration using Runge-Kutta methods. To use this numerical integration approach, the values of $\underline{R}$, $\underline{R}'$, and θ must be known at the starting point. For the drops measured in this study, this information was available at two points on the drop shape. At the top of the drops, $\underline{R}$ = height of the drop, $\underline{R}' = 0$, and $\theta = 0.0$ radians. At the contact point between liquid and solid at the drop's edge, $\underline{R}$ = radius of the drop's base, $\underline{R}' = \underline{R}/\tan(\pi - \text{contact angle})$, and $\theta = \pi/2$ radians. To reduce the error generated in the numerical integration, the solution of Equation (6) was started from both the top and the edge of the drop. These two solutions were then mated approximately halfway around the curvature.

Equation (6) contains one further unknown, which is the $\underline{b}$ term. This $\underline{b}$ is the radius of curvature at the top of the drop. This term was incorporated in the solution using a trial and error approach. A first approximation to $\underline{b}$ was obtained by assuming the drop to be a sphere portion. In this case, $\underline{b}$ was the radius of the

sphere. This approximation gave a minimum value for b. During the course of the integration, the volume of the integrated drop was accumulated. At the completion of the integration, the integrated volume was compared with the volume obtained by integrating the experimental data for the specific dynamic drop. The value for b was progressively increased until the two volumes agreed. At this point, the numerical approximation was complete, and the numerical values of R for the successive θ increments were punched on cards and used to describe the equilibrium portion of all the subsequent dynamic expressions for that particular drop.

The θ coordinate was incremented at one-degree intervals. Decreasing the increment size to 0.1 degree did not change the value of the integrated volume more than 0.1% for the final b. The R values at one-degree intervals were considered accurate for this work. The time savings with the larger interval was overwhelming.

COMPARISON WITH DROP DATA

Initial numerical solutions of Equation (6) were compared with experimental data from equilibrium drops of water on paraffin. The equilibrium shapes were measured with the microcomparator. The values for starting points of the solutions were measured. The numerical solutions of the equilibrium shape were plotted on the experimental data. The agreement was extremely good. Figure 10 shows a typical plot.

The oscillation of the dynamic drops of water and the lower % glycerol drops passed through the equilibrium form. It was possible to observe the accuracy of the numerical solutions for the equilibrium portion of the dynamic drop description in these cases. The experimental shape data were plotted versus the dynamic model for all the drops in this study. At any time in the oscillation when sin (ωt) equaled $n\pi$, (where ω = circular frequency, t = time, and n = an integer), the experimental data passed through the equilibrium form, and the dynamic description consisted of

Points are the experimental data.
Lines are the numerical solutions.

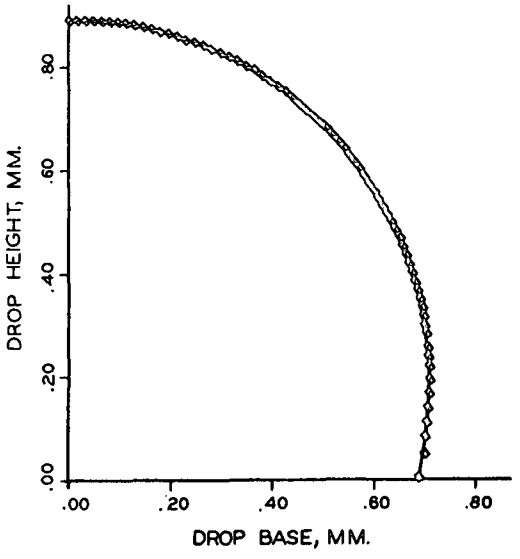

Equilibrium water drop
1.07 mm.^{3}

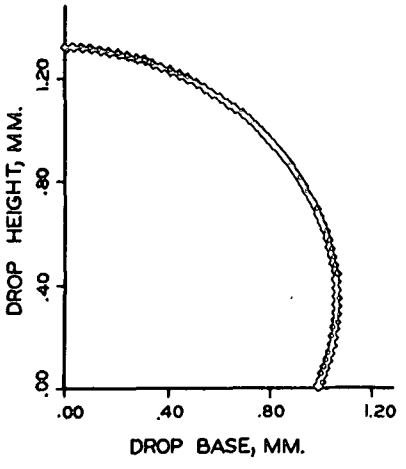

Equilibrium water drop
3.31 mm.^{3}

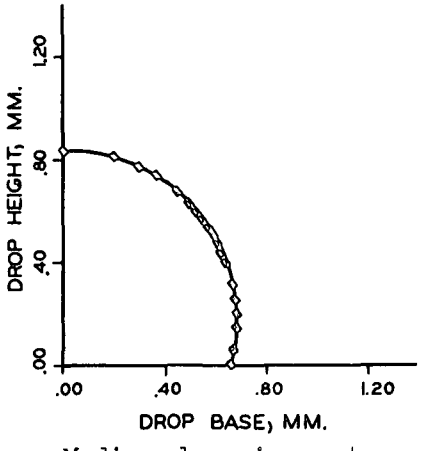

Median dynamic, water
film 17 0.885 mm.^{3}

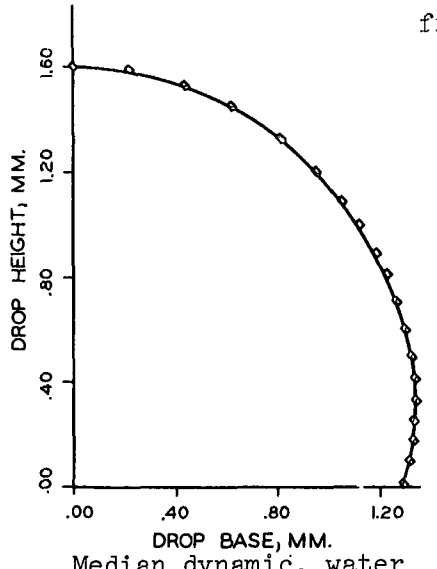

Median dynamic, water
Film 73 6.45 mm.^{3}

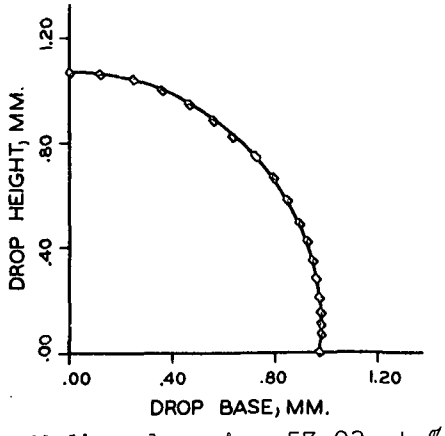

Median dynamic, 57.93 wt.% glycerol, Film 56 2.20 mm.^{3}

Figure 10. Comparison of Numerical Solutions and Experimental Data for Equilibrium and Median Dynamic Drop Shapes

the numerical equilibrium solution only. Examination of these plots for the water and lower % glycerol drops indicated the equilibrium numerical solutions were very accurate. Figure 10 shows several such plots from the dynamic model plots. These plots are representative of different boundary conditions (i.e., different liquids and volumes).

DYNAMIC DROP DESCRIPTION

SURFACE DESCRIPTION

Boundary Conditions and the Flow Model

The approach to describing the oscillation of a drop on a plane surface was presented in Equation (4). The equilibrium form was described by a table of values of R as a function of θ from the numerical integration of Equation (6). The perturbations about the equilibrium form were described by a series of Legendre polynomials, their respective A_n coefficients, and some time function as shown in Equation (7).

The time function was found to have a strict sinusoidal dependence. The experimental data for the position of the drop's top were plotted *versus* time. In every case, these data were fit extremely well with sinusoidal curves.

The oscillating drop on a plane surface had other key boundary conditions which were used in the selection of the A_n coefficients. The first of these was the condition of no slip at the wall. It was desirable to have a model which would give a zero velocity at the paraffin surface in the plane of the paraffin surface. Secondly, the oscillation of the drop and its mirror image must be symmetrical. This fact required that the A_n coefficients of odd order (i.e., $n = 1,3,\ldots$) be considered zero. Third, the drop volumes remained constant. This indicated that the A_o coefficient should be small. Finally, the amplitudes of the motion of the tops of the drops

were experimentally known. At the top of the drop θ, the spherical coordinate was equal to zero. This reduced all the Legendre polynomials to 1.0 at this point. Since the flow model had to meet the boundary condition of the amplitude of the top of the drop, the sum of the $\underline{A}_n$ coefficients had to equal the amplitude of the motion of the top of the drop.

Surface Description Coefficients

The boundary conditions of oscillating drop on a plane surface demanded that the perturbations be described by a series of even-numbered Legendre terms beginning with $\underline{n} = 2$. The sum of the $\underline{A}_n$ coefficients of this series had to equal the amplitude of the top of the drop. It was expected that Legendre series used to describe a simple mode of vibration, such as the mode in this study, would place the most emphasis on the initial coefficients in the $\underline{A}_n$ series. The first two even integer polynomials in the Legendre series (39) starting with $\underline{n} = 2$, are: $\underline{P}_2(\cos\theta) = (3\cos^2\theta - 1)/2$, and $\underline{P}_4(\cos\theta) = (35\cos^4\theta - 30\cos^2\theta + 3)/8$.

Inspection of these terms showed that the selection of the $\underline{A}_2$ and $\underline{A}_4$ coefficients to meet the boundary conditions and limit the series to two terms gave

$$A_2 = 3/7\ AH, \tag{22}$$

and

$$A_4 = 4/7\ AH. \tag{23}$$

Here, $\underline{AH}$ was the amplitude of the drop top motion.

The use of these two terms and the sinusoidal dependence of the motion reduced Equation (9) to,

$$S(\theta,t) = \sin(\omega t)[A_2(3\cos^2\theta-1)/2 + A_4(35\cos^4\theta-30\cos^2\theta+3)/8]. \tag{24}$$

Comparison with Experimental Data

Plots were made of the theoretical shape of the dynamic surfaces using the equilibrium descriptions and Equation (24) with the A_n coefficients described by Equations (22) and (23). Using a computer, the theoretical drops shapes were plotted over the experimental data at many different phases of the oscillation for all the drops in this study. The agreement was extremely good in all cases. This direct comparison indicated that Equation (24) gave a very good description of the surface perturbations of drops oscillating on plane surfaces. Figure 11 shows a direct comparison of the theory and the data for a water drop and a 57.93 wt. % glycerol drop at different phases in their oscillation.

Further substantiation for the selection of only two A_n coefficients to describe the dynamic surface will be discussed in connection with determination of the B_n coefficients.

VELOCITY POTENTIAL DETERMINATION

Selection of Coefficients

The general expression for the velocity potential, ψ, was given in Equation (11). This equation is also expanded in an even integer series of Legendre polynomials. The determination of the velocity potential requires the determination of a series of B_n coefficients associated with the Legendre polynomials. The B_n coefficients were necessarily related to the A_n coefficients through Equation (12),

$$(\text{viz.}, \frac{\partial S}{\partial t} = - \frac{\partial \psi}{\partial r} + \frac{1}{r^2} \cdot \frac{\partial \psi}{\partial \theta} \cdot \frac{\partial r}{\partial \theta}).$$

In the case of a free drop, this relationship is straightforward because the right-hand side of Equation (12) reduces to the first part.

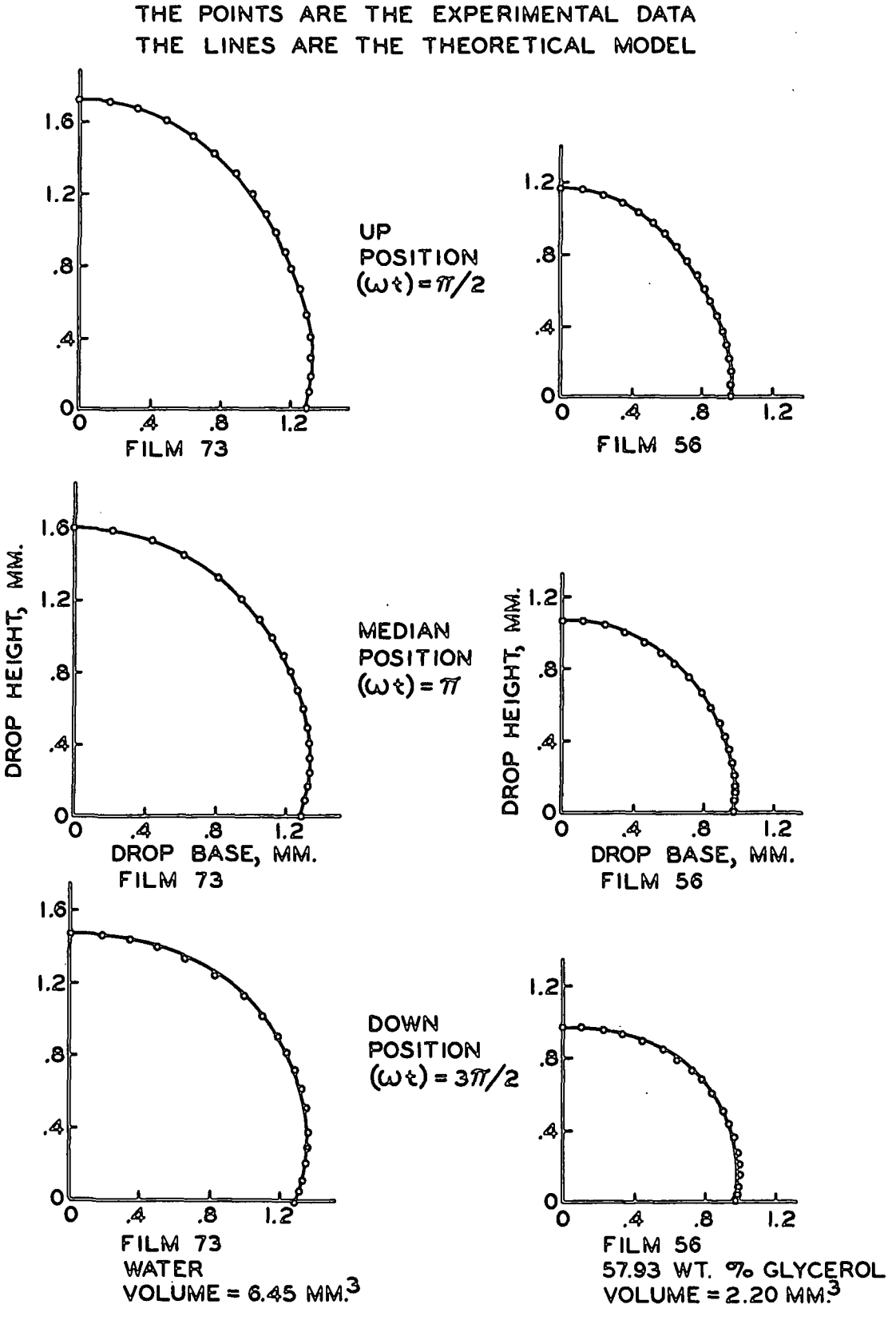

Figure 11. Comparison of the Theoretical and Experimental Oscillating Drop Shape in the Up, Median and Down Configurations

The general approach (46) for the determination of the coefficients of a Legendre series describing a function, $f(\mu)$, which is dependent on the position of a point on the equilibrium configuration was used to establish the relationship between the $\underline{A}_n$ and $\underline{B}_n$ coefficients. This approach is expressed in the equation,

$$A_n = (2n+1) \int_0^{+1} f(\mu) \cdot P_n(\mu) d\mu \ . \qquad (25)$$

The function, $f(\mu)$, selected for the integration, was the function relating the $\underline{A}_n$ and $\underline{B}_n$ coefficients, Equation (12). The relative magnitudes of the coefficients were judged by considering the $f(\mu)$ to consist of only one specific Legendre polynomial for each series of integrations of Equation (25). That is, Equation (25) was reduced to the form,

$$A_n = (2n+1) \int_0^{+1} \left[B_n \, mRP_m(\mu) + \frac{dR}{d\theta} (\mu P_m(\mu) - P_{m-1}(\mu)) \right] \cdot P_n(\mu) d\mu \ . \qquad (26)$$

The integrations of Equation (26) were carried out over the equilibrium surface for a particular drop. The integrations were first done for $\underline{m} = 2$. The series of $\underline{A}_n$ coefficients were determined by integrating with $\underline{n} = 2, 4, 6$, etc. The $\underline{A}_n$ series was then determined with $\underline{m} = 4$, and so on. The results for these calculations for a water drop on paraffin are shown in Table X.

Using the series of $\underline{A}_{n,m}$ coefficients calculated for each $\underline{B}_m$ coefficients, a series of six equations and six unknowns were solved for the $\underline{B}_m$ terms (with $\underline{n}$ and $\underline{m} = 2, 4, 6, 8, 10, 12$). The expression for the velocity potential, Equation (11), was then expanded to the first six even-numbered terms (excluding $\underline{m} = 0$) using the values for the $\underline{B}_m$ coefficients determined by the solution of the simultaneous equations. Using the resulting expression for ψ, the kinetic energy expression, Equation (20), was numerically integrated. The integration of Equation (20) was repeated eliminating the highest order term in the Legendre series. This process was continued until the

TABLE X

RESULTS FOR CALCULATIONS OF THE $\underline{A_n}$ COEFFICIENTS BASED ON THE VELOCITY POTENTIAL DERIVATIVES (WITH RESPECT TO THE COORDINATES) AND THE GEOMETRY OF A SMALL WATER DROP (NO. 17)

A Series Based on B 2

N	A(N)
2	-0.7736
4	-0.1336
6	0.0261
8	-0.0106
10	0.0063
12	-0.0024

A Series Based on B 8

N	A(N)
2	0.0017
4	-0.0024
6	-0.1328
8	-0.7210
10	-0.3219
12	0.0019

A Series Based on B 4

N	A(N)
2	-0.0077
4	-0.9345
6	-0.2610
8	0.0371
10	-0.0230
12	0.0180

A Series Based on B 10

N	A(N)
2	-0.0008
4	-0.0000
6	-0.0052
8	-0.1499
10	-0.5737
12	-0.2936

A Series Based on B 6

N	A(N)
2	-0.0044
4	-0.0852
6	-0.8629
8	-0.3189
10	0.0233
12	-0.0212

A Series Based on B 12

N	A(N)
2	0.0004
4	-0.0001
6	-0.0009
8	-0.0097
10	-0.1459
12	-0.4441

Based on B2 + B4, Total A2 = -0.7813

Based on B2 + B4, Total A4 = -1.0681

magnitude of the contribution to the kinetic energy was determined for each term in the series describing the velocity potential. For a water drop on paraffin, the results are shown in Table XI. These results showed that the $\underline{B}_2$ plus the $\underline{B}_4$ terms represented 99.6% of the total kinetic energy. The $\underline{B}_2$ term represented 46.5%, and the $\underline{B}_4$ term represented 53.1% of the total kinetic energy. The implication was that the dynamic behavior of the drop in the mode of vibration measured for this study was describable with the two Legendre polynomials, $\underline{P}_n(\mu)$, corresponding to $\underline{n}$ = 2 and 4.

TABLE XI

RESULTS OF THE DETERMINATION OF THE $\underline{B}_n$ SERIES OF COEFFICIENTS FOR A SMALL WATER DROP (NO. 17) AND THE MAGNITUDE OF THE EFFECT OF EACH TERM IN THE KINETIC ENERGY CALCULATION

$\underline{N}$	$\underline{B}_n$
2	-0.4429 x amplitude of drop top
4	-0.6279
6	0.0695
8	-0.0138
10	0.0044
12	-0.0015

Kinetic Energy	Terms Used	Total Kinetic Energy, %
6.998×10^{-3} ergs	B_2 to B_{12}	100.0
6.982×10^{-3} ergs	$B_2 + B_4$	99.6
3.247×10^{-3} ergs	B_2 only	46.5

Another very important deduction was made from these calculations. The contribution to the total kinetic energy by the correction term arising from the displacement of the origin from the "sphere" center and the gravitational effects causing departure from a spherical equilibrium form was only 1.12% of total kinetic energy. This fact

indicated that the second term on the right-hand side of Equation (12) was very small, and the relationship between the $\underline{A}_n$ and $\underline{B}_n$ coefficients can very satisfactorily be described by that for the free drop model (37). Assuming the corrective term to be small [the last term on the right-hand side of Equation (12)], comparison of Equation (9) and Equation (12) gives the relationship between the $\underline{A}_n$ and $\underline{B}_n$ coefficients as,

$$B_n = A_n/nR^{n-1}. \tag{26a}$$

For a free drop, the $\underline{R}$ term in this Equation (26a) is constant and equal to the radius of the sphere. For the drop on a plane surface with the origin at the center of the base, $\underline{R}$ is not constant. If $\underline{R}$ is integrated with respect to theta, an integrated value of $\underline{R}$ is obtained ($\underline{R}_s$). Equation (26a) becomes

$$B_n = A_n/nR_s^{n-1}. \tag{27}$$

Equation (27) indicates that the $\underline{B}_n$ coefficients have units of $1/cm.^{(\underline{n}-2)}$ (since $\underline{A}_n$ has units of cm.). The $\underline{B}_2$ and $\underline{B}_4$ coefficients were determined for all the drops using the approach outlined with Equations (25) and (26). These $\underline{B}_2$ and $\underline{B}_4$ coefficients were then put in the form shown in Equation (27). The $\underline{A}_2$ and $\underline{A}_4$ coefficients determined in this manner agreed very well for all the drops with the $\underline{A}_2$ and $\underline{A}_4$ coefficients determined using Equations (22) and (23). It was concluded that Equation (27) is a very good approximation to the $\underline{A}_n$ to $\underline{B}_n$ relationship for the oscillating drops in this study.

Calculated Potential Lines and Streamlines

By reducing Equation (11) to the first two terms, the lines of equal velocity potential were readily calculated for any drop oscillating in its first mode of vibration on a plane surface. This gave ψ as,

$$\psi = -\omega \cdot \cos(\omega t)\,[B_2 r^2\, P_2(\cos\theta) + B_4 r^4\, P_4(\cos\theta)] \tag{28}$$

Here, $\underline{r}$ is any position on the drop surface or within the drop. A plot of the calculated potential lines for a particular water drop at $\omega\underline{t}$ = 0 radians is shown in Fig. 12.

The velocity potential lines and the streamlines are everywhere normal to one another (47). The streamlines were, therefore, given by,

$$\Phi = - \omega \cdot \cos(\omega t) \cdot (\cos^2\theta) \left[2B_2 r^3 P_2(\cos\theta) + 4B_4 r^5 P_4(\cos\theta)\right] \qquad (29)$$

Figure 12 also shows the streamlines calculated for the same water drop at $\omega\underline{t}$ = 0 radians.

EVALUATION OF INTEGRAL EXPRESSIONS

Method of Integration

The values for the different integral expressions were numerically integrated at intervals of one degree θ. The method used was a straight summing of the increments. Simpson's Rule (48) was used to numerically integrate some of the integrals for the liquid-vapor potential energy. These results were compared with the step summation values for the same integrals. The results were found to agree very closely. The step summation approach to solution of the integrals was considered to be sufficiently accurate in this study.

Comparison of Theoretical and Experimental Volumes

The drop volumes obtained from numerical integration of the experimental data were compared with drop volumes obtained from numerical integration of the theoretical dynamic description [Equation (16)]. The agreement of the values was very good. The differences were generally less than one percent. The values are compared in Table XII.

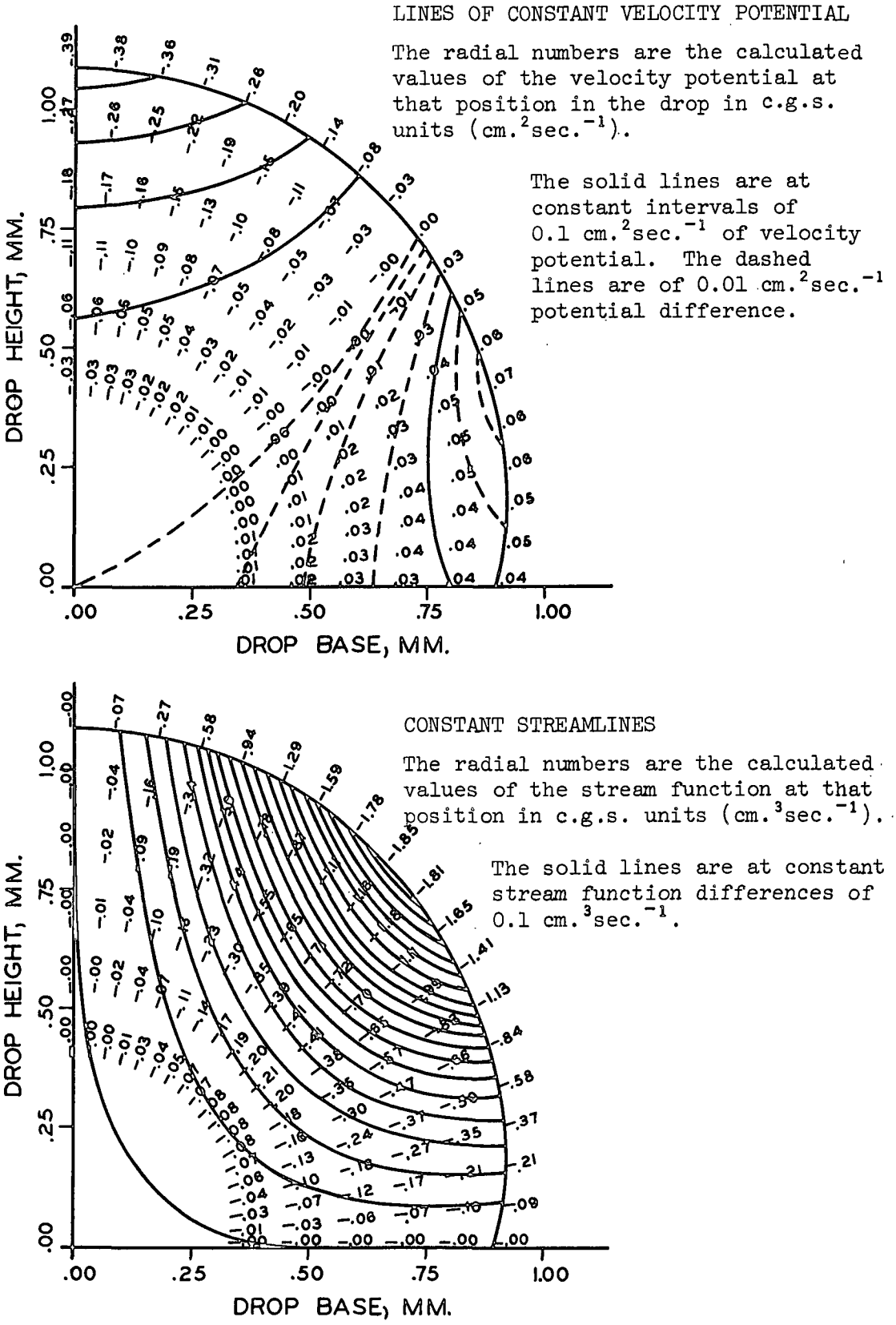

Figure 12. Maximum Velocity Potential Lines and Streamlines for an Oscillating Water Drop

TABLE XII

COMPARISON OF VOLUMES INTEGRATED
FROM THE MODEL AND THE EXPERIMENTAL DATA

Film Number	Experimental Volume, $mm.^3$	Model Volume, $mm.^3$
17	0.885	0.886
34	2.03	2.05
18	2.12	2.16
20	3.27	3.27
36	4.00	3.97
33	4.31	4.32
21	5.49	5.48
73	6.45	6.48
41	1.89	1.91
45	2.95	2.95
43	6.42	6.46
56	2.20	2.22
61	2.46	2.48
53	3.66	3.69
63	4.26	4.29
54	6.69	6.72
65	7.09	7.04
77	3.12	3.12
82	3.79	3.81
79	6.34	6.37
81	8.05	8.11

Energy Balance

Kinetic and Potential Energy Transfers

At any phase in the steady-state oscillation of a drop on a plane surface, the overall energy balance is given by

$$T + dV_1 + dV_2 + dV_3 = I - Q. \qquad (30)$$

Here, T is the kinetic energy, and dV_1, dV_2, and dV_3 are the changes in potential energy of the liquid-vapor interface, the liquid-solid interface, and the gravitational potential, respectively. I is the energy added to the system by the drive

coil to keep the oscillation steady-state, and $\underline{Q}$ is the energy lost to viscous dissipation.

The sum of the right-hand side of Equation (30) is zero. The magnitude of $\underline{Q}$ will be discussed in a later section. The sum of the left-hand side of Equation (30) is also zero. It involves the transfer of kinetic and potential energy in the oscillating drop. When the drops were in the $\omega\underline{t}$ = 0π, 1π, 2π, etc., radians phase of their oscillation, the kinetic energy of the drops was at a maximum, and the potential energy was at a minimum which corresponded to the potential energy of the equilibrium state. When the drops were in the $\omega\underline{t}$ = π/2, 3π/2, etc., radians phase of their oscillation, the kinetic energy of the drops was zero, and their potential energy was at a maximum.

The maximum values of the kinetic energy of the drops were calculated for all the drops by numerically integrating Equation (20) for the $\omega\underline{t}$ = zero radians phase of their oscillation. The values of the potential energy stored in the liquid-vapor surface ($\underline{V}_1$) and the gravitational potential ($\underline{V}_3$) for all the drops were determined by numerical integration of Equations (17) and (19) for the maximum up, median, and maximum down drop configurations ($\omega\underline{t}$ = π/2, 3π/2, and 0π radians, respectively).

The maximum potential energy changes for the liquid-vapor interface and the gravitational potential were calculated for the up position ($d\underline{V}_1$ up, $d\underline{V}_3$ up) and down position ($d\underline{V}_1$ down, $d\underline{V}_3$ down) by subtracting the values calculated for the equilibrium position from the values calculated from the extreme up and down configurations. Based on the left-hand side of Equation (80), the following equations can be written:

$$T_{max} = dV_1 \text{ up} + dV_2 \text{ up} + dV_3 \text{ up}, \tag{31}$$

$$T_{max} = dV_1 \text{ down} + dV_2 \text{ down} + dV_3 \text{ down}. \tag{32}$$

From Equations (31) and (32) theoretical predictions of the maximum potential energy changes in the liquid-solid interface were obtained for all the drops in the extreme up ($d\underline{V}_2$ up) and extreme down ($d\underline{V}_2$ $d\underline{n}$) drop configurations.

The theoretically calculated values in ergs for all the drops of the maximum kinetic energy and the maximum changes in potential energy ($d\underline{V}_1$, $d\underline{V}_2$, $d\underline{V}_3$) for the extreme up and down configurations are shown in Table XIII.

The theoretical model calculations indicated the same type of behavior for all the drops. In the maximum up configuration, the kinetic energy was transferred to potential energy stored in an increased gravitational potential (relative to the equilibrium state) and increased liquid-vapor surface area (relative to the equilibrium state). In addition, a loss in potential energy stored in the liquid-solid interface was obtained. This indicated that there was a decrease in the energy stored in the solid-liquid interface relative to the equilibrium state.

For the extreme down configuration, the calculations showed potential energy decreases (relative to the equilibrium state) in the gravitational potential and the liquid-vapor interfacial area. This indicated a fairly large increase in the energy stored in the liquid-solid interface due to the kinetic energy transferred to potential energy, the decrease in the gravitational potential, and the slight decrease in the liquid-vapor surface area.

The values of $\underline{T}$, $d\underline{V}_1$, $d\underline{V}_2$, and $d\underline{V}_3$ were calculated for several drops at intervals of $d(\omega\underline{t}) = \pi/8$ radians for one complete phase of drop oscillation. Figure 13 shows the plots of the values calculated for a particular water drop. The kinetic and potential energy transfers at any phase of the drop oscillation are shown in this figure. The calculated data for this plot are in Appendix IV.

TABLE XIII

SUMMARY OF THE POTENTIAL ENERGY CHANGES CALCULATED FROM THE MODEL FOR THE EXTREME UP AND DOWN CONFIGURATIONS AND THE MAXIMUM KINETIC ENERGY

$\underline{T}_{max}$ = maximum kinetic energy

$d\underline{V}_1$ = change in liquid-vapor potential energy

$d\underline{V}_2$ = change in liquid-solid potential energy

$d\underline{V}_3$ = change in gravitational potential energy

Film No.	Mixture	$\underline{T}_{max}$, $\times 10^{-3}$ ergs	Up Position			Down Position		
			$d\underline{V}_1$, $\times 10^{-3}$ ergs	$d\underline{V}_2$, $\times 10^{-3}$ ergs	$d\underline{V}_3$, $\times 10^{-3}$ ergs	$d\underline{V}_1$, $\times 10^{-3}$ ergs	$d\underline{V}_2$, $\times 10^{-3}$ ergs	$d\underline{V}_3$, $\times 10^{-3}$ ergs
17	H_2O	6.982	8.691	- 3.622	1.914	- 3.638	+11.943	- 1.323
34	"	9.248	10.387	- 5.579	4.440	- 3.941	16.363	- 3.174
18	"	21.156	21.847	- 9.156	8.465	- 6.685	33.095	- 5.253
20	"	28.974	31.068	-17.474	15.380	-11.108	49.784	- 9.702
36	"	35.256	33.339	-17.566	19.484	- 8.906	55.966	-11.803
33	"	18.258	22.838	-19.140	14.560	-10.426	39.056	-10.372
21	"	34.714	35.359	-26.507	25.863	-12.806	64.452	-16.932
73	"	20.522	22.444	-22.152	20.230	- 9.727	45.024	-14.775
41	40.32 wt. % glycerol	13.289	10.132	- 1.884	5.041	- 1.849	18.434	- 3.296
45	"	9.175	14.682	-14.856	9.350	- 3.853	19.259	- 6.230
43	"	29.349	7.949	- 7.752	13.648	- 0.397	38.857	- 9.907
56	57.93 wt. % glycerol	9.493	6.365	- 1.496	4.624	- 0.268	12.921	- 3.160
61	"	9.535	6.934	- 2.618	5.219	- 0.993	14.193	- 3.665
53	"	22.426	11.967	- 1.305	11.764	+ 1.627	28.012	- 7.213
63	"	23.535	10.932	- 1.421	12.745	+ 1.590	30.061	- 8.115
54	"	18.313	7.953	- 5.476	15.836	+ 1.708	27.721	-11.115
65	"	21.202	11.017	- 9.345	19.531	+ 1.028	33.564	-13.390
77	75.13 wt. % glycerol	13.354	8.397	- 3.008	7.965	- 0.696	19.484	- 5.435
82	"	15.497	9.021	- 3.644	10.119	- 0.381	22.772	- 6.894
79	85.17 wt. % glycerol	7.623	5.555	- 9.425	11.493	- 1.038	17.678	- 9.017
81	"	8.920	4.468	-10.343	14.795	+ 1.117	19.146	-11.343

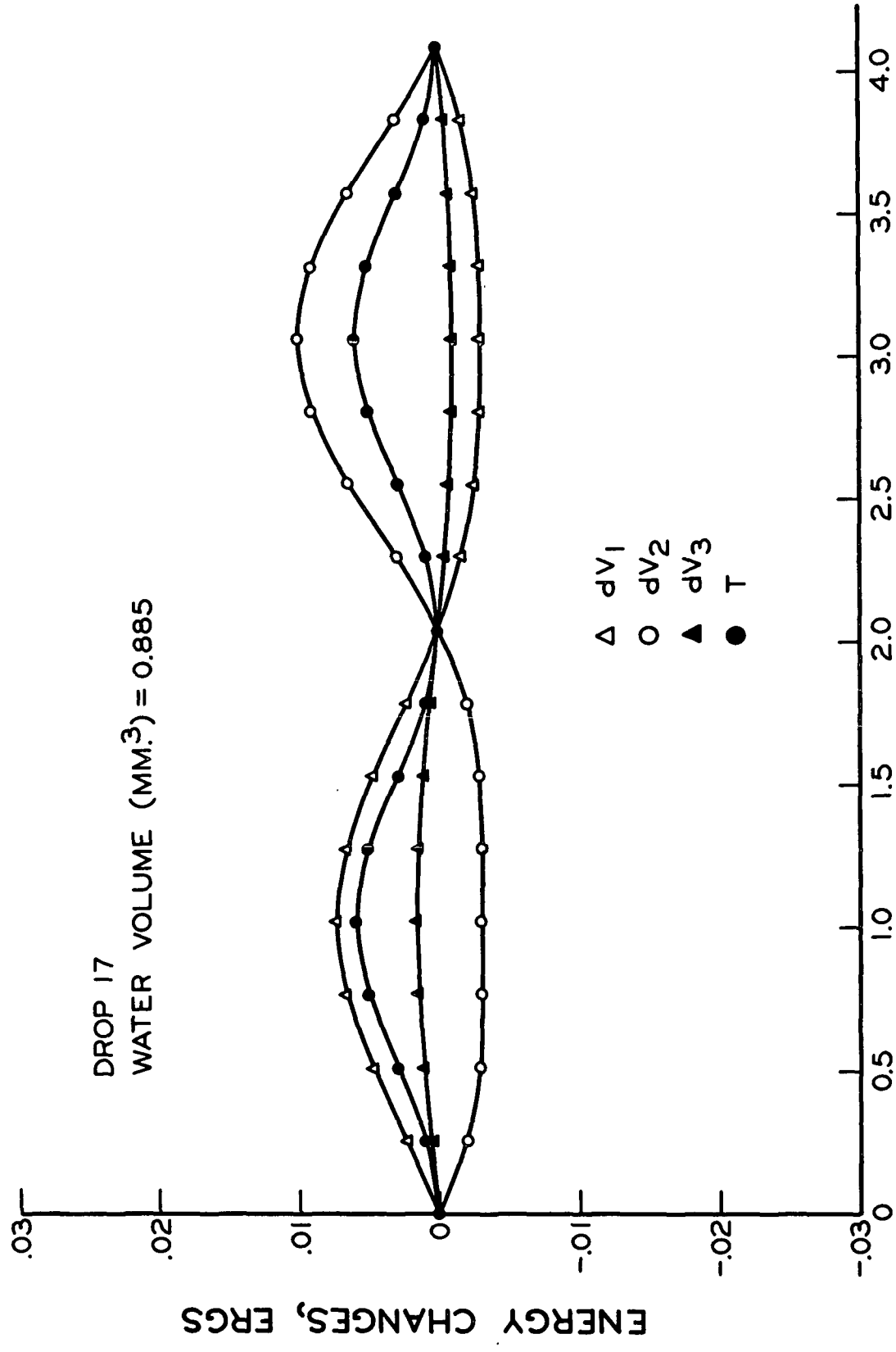

Figure 13. The Potential and Kinetic Energy Changes in One Period of Drop Oscillation

Comparison of Theoretical and Experimental Values

Gravitational Changes. The experimental gravitational changes were determined by integrating the experimental data at different phases of drop oscillation and plotting the results versus time. These results were found to be approximately sinusoidal. Based on sinusoidal behavior, the experimental amplitudes of these changes were given in Table V. These experimental amplitudes, the densities of the liquids, and the experimental drop volumes were used to calculate the maximum values of the gravitational potential energy changes in ergs for all the drops. These values are compared in Table XIV with the theoretical values calculated from Equation (19) for the extreme up and down drop configurations.

The model predicts a gravitational motion that is not quite sinusoidal. The experimental data obtained for the gravitational motion of the drops could just as easily have been fit to curves giving the slightly nonsinusoidal motion described by the model instead of being characterized by purely sinusoidal curves. The comparison of the values shown in Table XIV shows a very good agreement between the experimental determinations and the theoretical calculations for all the drops.

Liquid-Solid Interface Changes. The energy changes in the solid-liquid interface during drop oscillation were theoretically predicted from Equations (31) and (32) since this energy was the only unknown in those expressions. These theoretical results were summarized in Table XIII. When the drops were in their extreme up configurations, the decreases in the potential energy stored in the liquid-solid interfaces were approximately one half the magnitude of the increases that were obtained when the drops were in their extreme down configurations.

Experimental amplitudes for the sinusoidal motion for the edges of all the drops were reported in Table V. It was indicated in the discussion of error analysis that the error in these measured amplitudes could be very large. However, these

TABLE XIV

COMPARISON OF THEORETICAL AND EXPERIMENTAL VALUES OF THE CHANGES IN GRAVITATIONAL POTENTIAL AT THE EXTREME UP AND DOWN POSITIONS

Film Number	Experimental dV_3 Up and Down, $\times 10^{-3}$ ergs	Theoretical dV_3 Up, $\times 10^{-3}$ ergs	Theoretical dV_3 Down, $\times 10^{-3}$ ergs
17	± 1.978	+ 1.914	- 1.323
34	± 4.398	4.440	- 3.174
18	± 7.690	8.465	- 5.253
20	±13.452	15.380	- 9.702
36	±18.075	19.484	-11.803
33	±13.509	14.560	-10.372
21	±23.036	25.863	-16.932
73	±18.600	20.230	-14.775
41	± 5.259	5.041	- 3.296
45	± 8.212	9.350	- 6.230
43	±17.967	13.648	- 9.907
56	± 5.071	4.624	- 3.160
61	± 5.311	5.219	- 3.665
53	± 9.713	11.764	- 7.213
63	±11.882	12.745	- 8.115
54	±17.228	15.836	-11.115
65	±20.410	19.531	-13.390
77	± 6.994	7.965	- 5.435
82	±10.183	10.119	- 6.894
79	± 8.872	11.493	- 9.017
81	±16.858	14.795	-11.343

amplitudes represented an estimate of the area changes of the liquid-solid interfaces during drop oscillation. Consideration of the maximum and minimum dynamic contact angles measured for the different oscillating drops led to the calculated values reported in Table IX of the maximum and minimum energies associated with the three-phase boundary region for the different liquid mixtures used in this study. The maximum energy values were averaged with the equilibrium energy values of the dynamic three-phase boundary region to give an estimate of the average ergs $cm.^{-2}$ that were given up by the rest of the dynamic system to create the liquid-solid area increase obtained when the drop moved from the median to the extreme down configuration. The energy in ergs $cm.^{-2}$ of the solid area involved in this increase was subtracted from the average, since its contribution to the energy of the system remained constant. In a similar manner, the average energies required for the different liquids to create the total liquid-solid area increase in going from the extreme up to the median configurations were obtained by averaging the energy in ergs $cm.^{-2}$ associated with the three-phase boundary in those two positions and subtracting the constant contribution of the solid surface. The average energies in ergs $cm.^{-2}$ expended in the creation of the liquid-solid interfacial area in these two phases of drop oscillation for the different liquid mixtures are shown in Table XV.

The experimental edge amplitudes were used to calculate the liquid-solid area changes for the different drops between the extreme up and median configurations and the median and the extreme down configurations. These area changes were multiplied by the average energy changes, given in Table XV, associated with the creation of these liquid-solid interfacial areas. These energy calculations, based on experimental information, of the energy changes associated with the creation or removal of liquid-solid interfacial areas were compared with the theoretical energies assigned to this region based on calculations from the model. This comparison is

shown in Table XVI. In spite of the possible error in the edge amplitudes and the use of average energies for each liquid mixture, the agreement of the experimental values and the theoretically assigned values was very good. In particular, the agreement of the values was good in regard to the magnitude of the differences in energy required to create liquid-solid area from the up to median and the median to down configurations.

TABLE XV

AVERAGE ENERGY DIFFERENCES PER CM.$^{-2}$ ASSOCIATED WITH THE LIQUID-SOLID INTERFACIAL AREA CREATED OR REMOVED BETWEEN THE UP AND MEDIAN AND DOWN AND MEDIAN POSITIONS

(Calculations based on the average contact angle changes for each mixture on paraffin)

Mixture	Average Between Up and Median, ergs cm.$^{-2}$	Average Between Down and Median, ergs cm.$^{-2}$
H_2O	41.6	58.6
40.32% glycerol	37.6	48.9
57.93% "	31.5	43.6
75.13% "	31.4	42.0
85.17% "	31.4	40.2

It should be noted that the energies referred to here associated with the liquid-solid interfacial area changes are not necessarily "stored" energies. They are energies associated with the creation or removal of liquid-solid interfacial area. This point is elaborated further in the discussion of the results.

Viscous Heat Dissipation

Calculated Rates of Heat Loss

The steady-state oscillation of the drops on the plane surface had to be driven. It was expected that the viscous behavior of the drops would generate a certain amount

TABLE XVI

COMPARISON OF THE MODEL AND EXPERIMENTAL CALCULATIONS OF THE CHANGES IN LIQUID-SOLID INTERFACIAL POTENTIAL ENERGY IN THE EXTREME UP AND DOWN POSITIONS

Film Number	Experimental		Theoretical	
	dV_2 Up, $\times 10^{-3}$ ergs	dV_2 Down, $\times 10^{-3}$ ergs	dV_2 Up, $\times 10^{-3}$ ergs	dV_2 Down, $\times 10^{-3}$ ergs
17	- 3.622	+10.840	- 3.622	+11.943
34	- 9.162	22.011	- 5.579	16.363
18	-13.834	33.237	- 9.156	33.095
20	-16.357	39.297	-17.474	49.784
36	-16.436	39.488	-17.566	55.966
33	-16.625	39.941	-19.140	39.056
21	-18.614	44.721	-26.507	64.452
73	-17.534	42.125	-22.152	45.024
41	- 5.370	15.587	- 1.884	18.434
45	- 6.102	17.710	-14.856	19.259
43	- 3.971	11.530	- 7.752	38.857
56	- 0.945	7.123	- 1.496	12.921
61	- 0.638	4.808	- 2.618	14.193
53	- 2.023	15.257	- 1.305	28.012
63	- 1.073	8.093	- 1.421	30.061
54	- 1.486	11.205	- 5.476	27.721
65	- 1.415	10.668	- 9.345	33.564
77	- 0.933	3.732	- 3.008	19.484
82	- 1.865	7.460	- 3.644	22.772
79	- 1.750	6.821	- 9.425	17.678
81	- 1.420	5.682	-10.343	19.146

of heat. The rate of heat dissipation in ergs/sec. was calculated for the drops of different volumes, surface tensions, and viscosities by numerical integration of Equation (21). The maximum rates were divided by eight times the vibrational frequencies of the respective drops. These results gave the total amount of heat energy dissipated in ergs during the time required in the drop oscillation for the kinetic energy to go from zero to a maximum (i.e., one fourth of a phase). These results are presented in Table XVII. The magnitude of these dissipated energies can be compared to the kinetic energies in Table XIII. They were quite small for the water drops. For the more viscous drops (i.e., 85.17% glycerol), the heat dissipation energies in the time required to achieve the maximum kinetic energies were comparable in magnitude to the maximum kinetic energies.

TABLE XVII

CALCULATED VISCOUS HEAT LOSSES PER 1/4 CYCLE
FOR THE OSCILLATING DROPS

Film Number	Heat Loss, $x10^{-3}$ ergs	Film Number	Heat Loss, $x10^{-3}$ ergs
17	-0.398	56	- 2.895
34	-0.415	61	- 2.870
18	-1.032	53	- 6.016
20	-1.343	63	- 5.722
36	-1.494	54	- 3.968
33	-0.779	65	- 4.837
21	-1.389		
73	-0.733	77	-13.52
		82	-14.75
41	-1.919		
45	-1.761	79	-20.22
43	-2.084	81	-21.38

The temperature rise associated with this viscous effect, however, was found to be extremely small. A sample calculation was made using the drop from film number 82. The heat generated during 10 seconds of oscillation of that 75.13% glycerol drop would give a temperature rise of approximately 4.3×10^{-5} °C. (based

on a specific heat of 1 cal./g./deg.). The filming times were much shorter than 10 seconds. It was assumed that the viscous heating would have an extremely small effect on the surface tension and the viscosity of the drop.

Comparison of Theoretical and Experimental Decay Times

Experimental decay times were measured from high-speed films taken of the viscous damping of drops of different volumes and glycerol-water mixtures. These experimental decay times were presented in Table VI.

The kinetic energy and the rates of viscous heat dissipation were calculated for the steady-state oscillating drops. If the steady-state driving input to these drops had been stopped, the viscous effect would have damped out the oscillation. The decay times were calculated for the different drops using Equation (21d). These calculations resulted in theoretical predictions of the decay times for the steady-state oscillating drops.

These theoretically calculated decay times are compared with the experimentally obtained decay times in Table XVIII. The experimental and theoretical values were found to agree well.

MECHANICAL EFFECTS ON DYNAMIC CONTACT ANGLES

Velocities and Accelerations Based on the Flow Model

Equation (12) gave the radial velocity at any position in a drop oscillating on a plane surface. The radial accelerations were calculated by an initial partial differentiation of Equation (28) with respect to r and a second partial differentiation of that result with respect to t (time). The radial velocities and accelerations were calculated for representative drops of the different mixtures at the liquid-vapor interfacial surface. These calculations were made at one degree intervals of θ from the three-phase boundary to a point 19 degrees above the solid

TABLE XVIII

THEORETICAL DECAY MODULI FOR STEADY-STATE DROPS
COMPARED WITH EXPERIMENTAL VALUES FOR DAMPED DROPS

Mixture	Theoretical		Experimental	
	Volume, $mm.^3$	Decay Modulus, $x10^{-3}$ sec.	Volume, $mm.^3$	Decay Modulus, $x10^{-3}$ sec.
H_2O	0.885	36.0	--	--
"	2.03	67.0	2.03	85.0
"	2.12	66.0	--	--
"	3.27	83.5	--	--
"	4.01	99.3	3.80	92.0
"	4.31	103.0	4.45	100.0
"	5.49	121.0	6.07	101.0
"	6.45	139.0	6.40	110.0
40.32 wt. % glycerol	1.89	20.0	1.92	22.0
"	2.95	19.1	2.94	37.0
"	6.42	72.0	6.29	58.0
57.93 wt. % glycerol	2.20	11.0	2.36	24.5
"	2.46	12.0	2.61	24.0
"	3.66	16.1	--	--
"	4.26	18.5	3.69	36.5
"	6.69	25.5	4.43	43.0
"	7.09	25.8	6.89	40.0
75.13 wt. % glycerol	3.12	3.9	--	--
"	3.79	4.5	--	--
"	--	--	5.87	22.0
"	--	--	9.07	32.5
85.17 wt. % glycerol	6.34	2.2	7.59	13.0
"	8.05	2.9	8.93	13.0

surface (i.e., $\theta = 90°$ to $71°$). The radial velocities and accelerations were then reduced to their x-direction component (viz., the component parallel to the solid surface). The calculated streamlines shown in Fig. 12 indicated that the fluid particles in these regions would actually have most of their motion in a direction parallel to the solid surface plane.

The x-direction velocities and accelerations were then plotted versus the height above the solid surface for different phases of the oscillation. Typical results are shown for a water drop and a 75.13% glycerol drop in Fig. 14. The maximum values obtained for the x-direction velocities and accelerations and the height above the solid surface at which these values were obtained are summarized in Table XIX for the representative drops on which these calculations were made.

Inspection of plots of the velocity and acceleration profiles, such as those shown in Fig. 14, indicated that these instantaneous profiles were not linear. It was not expected that they should be linear. However, the profiles could be reasonably approximated as linear. Such approximations allowed the expression of the x-direction velocity and acceleration gradients existing at a particular time as constants. While these results were not exactly correct, they gave a good approximation of the shearing forces and the rate of change of shearing forces that were acting in the liquid-vapor surface in the region above the solid surface. The maximum values that were obtained for the "constant" velocity and acceleration gradients are also presented in Table XIX. It was noted that the maximum velocity gradients were not particularly large, but the acceleration gradients reached very large values.

Viscous and Inertial Effects

Inspection of all the plots of the theoretical drop shapes versus the experimental data indicated that the model deviated very slightly from the data in the

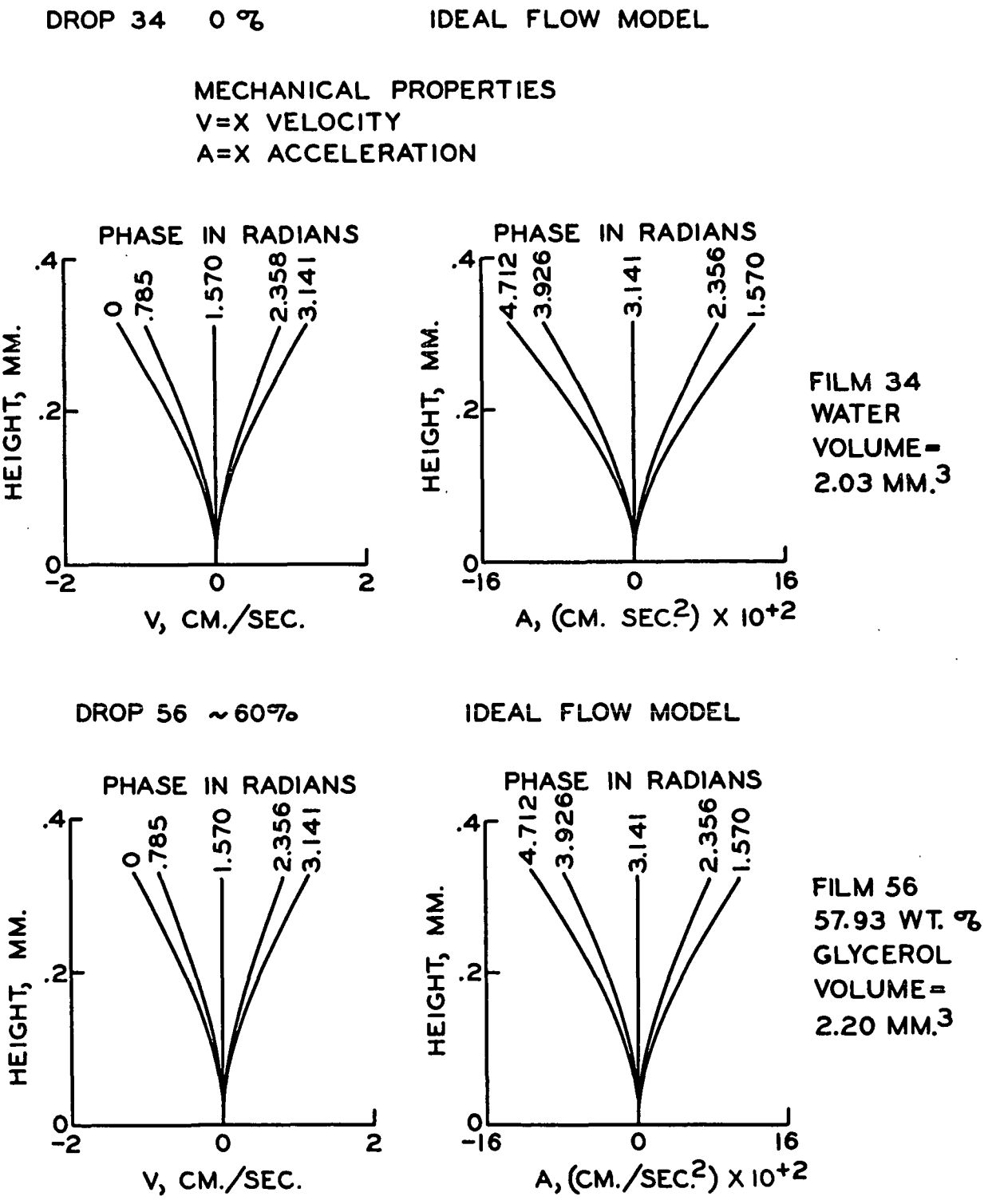

Figure 14. Velocity and Acceleration Profiles in the Liquid-Vapor Interface Above the Contact Point Calculated from the Model

region above the three-phase boundary. The model did not allow the liquid-vapor surface to come in quite as far as the experimental data when the drops were in their extreme up position. Likewise, the model did not allow the liquid-vapor surface to extend out quite as far as the experimental data in the extreme down position of the drops. This deviation was symmetrical in all cases, and the model and experimental data did coincide exactly for all the drops when the shape passed through its median configuration. This slight deviation can be seen by close inspection of Fig. 4 which showed a typical plot of the theoretical dynamic model compared with the experimental data.

TABLE XIX

SUMMARY OF THE FLOW MODEL CALCULATIONS OF THE MAXIMUM VELOCITY, ACCELERATION, AND ACCELERATION GRADIENT NEAR THE THREE-PHASE BOUNDARY FOR REPRESENTATIVE DROPS

Film No.	Mixture	Max. Velocity, cm. $sec.^{-1}$	Max. Accel., cm. $sec.^{-2}$	Height Above Solid, mm.	Max. Accel. Gradient,[a] $x10^{4}$ $sec.^{-2}$
17	H_2O	1.653	2506	0.23	10.00
34	"	1.261	1294	0.31	4.00
36	"	1.764	1293	0.39	3.00
73	"	1.050	639.6	0.46	1.25
41	40.32 wt. % glycerol	1.504	1575	0.31	2.25
45	"	1.207	1012	0.35	3.00
56	57.93 wt. % glycerol	1.163	1084	0.33	3.00
63	"	1.303	947.8	0.41	2.20
77	75.13 wt. % glycerol	1.127	890.9	0.36	2.25
81	85.17 wt. % glycerol	0.561	258.2	0.51	0.50

[a] A linear approximation was made to the entire acceleration profile.

The flow model used in this study was an ideal flow model based on potential flow theory. The coefficients for the Legendre series describing the dynamic drop behavior were selected to meet the boundary condition of no slip at the wall.

Therefore, the ideal flow model included an approximation to the viscous effects at the solid surface. If the viscous shearing effects near the solid surface had been large, a measurable hysteresis of the dynamic contact angles on advancing and receding would have been obtained. No hysteresis was found in the dynamic contact angle data. The contact angle data, in all cases, were sinusoidal. All the drops passed through the same median configuration on advancing as they did on receding.

The deviation of the ideal model was 180 degrees out of phase with the acceleration values. That is, a large deceleration was accompanied by a positive deviation of the experimental data from the ideal model. The very large value of acceleration changes calculated from the ideal model indicated that the inertial effects would be significant.

It was concluded that these slight deviations of the ideal flow model from the experimental drop shape data were due to inertial forces.

Corrected Velocities and Accelerations

The inertial effects did not have a large effect on the overall energy considerations of a drop oscillating on a plane surface. However, the x-direction velocities calculated from the model in the region above the three-phase boundary were very small. The slight positive deviations of the experimental drop shapes from the ideal model indicated that the model was not describing enough flow in this region. Since the velocity values were small, the deviation could have resulted in fairly large differences between the theoretical velocities and the actual velocities.

Corrected values for the velocities and accelerations were obtained by first calculating the values from the ideal model (as discussed earlier). An amplitude correction was calculated for the r value at $\theta = 81°$ based on the ideal acceleration and the deviation distance of the experimental data from the ideal model at that point. This correction was then applied to the r values from $\theta = 82$ to $90°$ in

proportion to the ideal acceleration calculated at that point. The velocities and accelerations were then recalculated using the corrected r values and the ideal model expressions.

The r values that were corrected on the basis of the initial acceleration profiles were plotted versus the experimental shape data for all the drops. This correction eliminated the slight deviation between the model and the experimental shape data. Figure 15 shows a typical plot of the corrected r values versus the data.

The recalculated values for the x-direction velocities and accelerations were approximately twice as large as the initially calculated values. The corrected values for the velocity and acceleration profiles shown in Fig. 14 are shown in Fig. 16. Table XX presents the corrected calculated values for all of the drops of the maximum velocities and accelerations, the height above the solid surface, and the respective "constant" gradients.

Comparison with Dynamic Contact Angles

The rates of x-direction shear (in $sec.^{-1}$) in the liquid-vapor interface in the region near the three-phase boundary were calculated for the different drops at different phases of their oscillation. For a given drop, these shear rates ranged from zero to ωt = odd multiples of $\pi/2$ to a maximum value at ωt = multiples of π. The maximum shear rates for the different drops are reported in Table XX. The maximum shear rates ranged from $\sim$ 60 to 200 $sec.^{-1}$. These calculated velocity gradients represented relatively small shear rates. In addition, no hysteresis of the dynamic contact angles was observed. It was concluded that in the oscillating drops studied in this work, there was no measurable effect of viscosity on the dynamic contact angles.

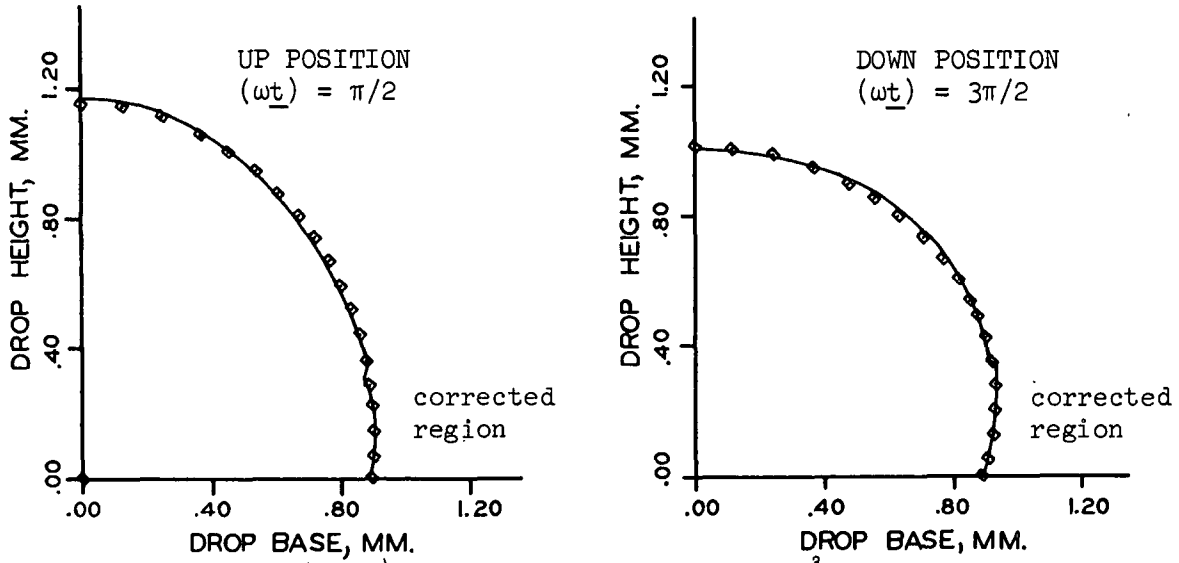

Film 34, Water, Volume = 2.03 mm.^{3}

Figure 15. Corrected Drop Shape Above the Contact Point, Based on the Theoretical Acceleration Profiles

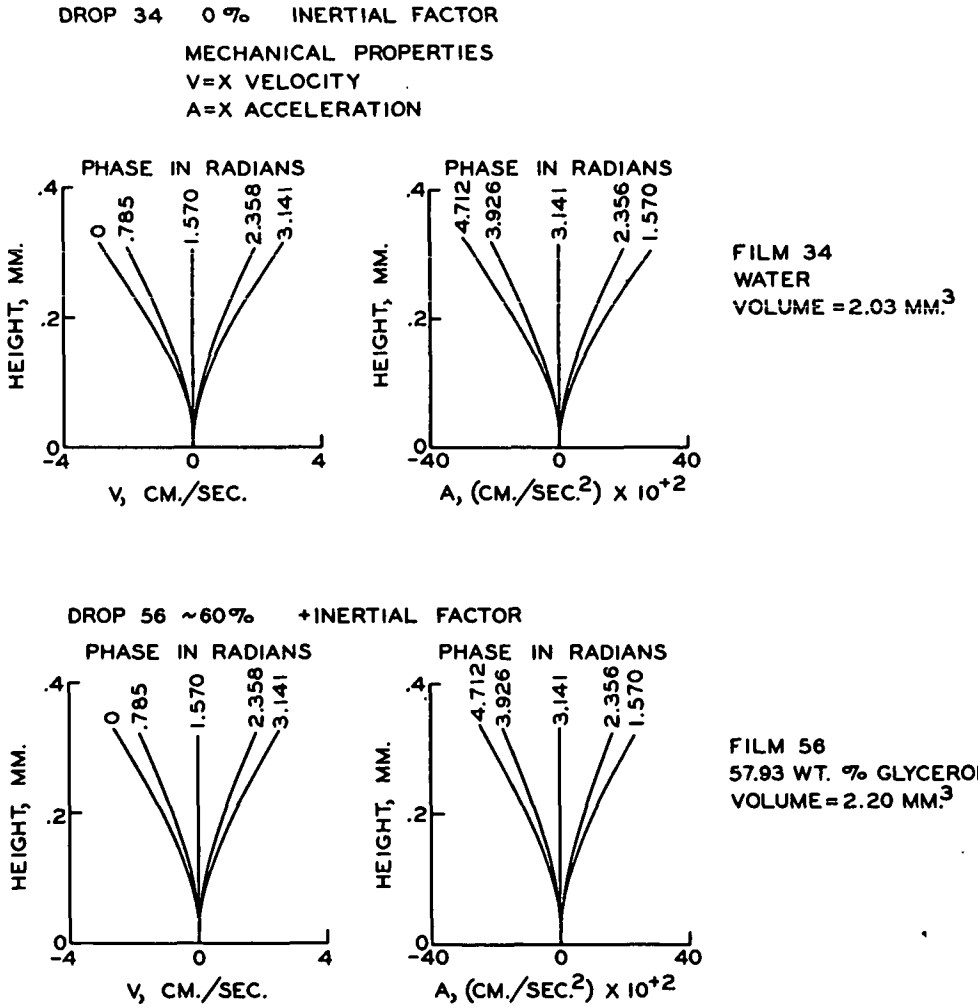

Figure 16. Corrected Velocity and Acceleration Profiles in the Liquid-Vapor Interface Above the Contact Point

TABLE XX

SUMMARY OF THE CORRECTED FLOW MODEL CALCULATIONS OF THE MAXIMUM VELOCITY, ACCELERATION AND ACCELERATION GRADIENT NEAR THE THREE-PHASE BOUNDARY

Film No.	Mixture	Max. Velocity, cm. sec.$^{-1}$	Max. Accel., cm. sec.$^{-2}$	Height Above Solid, mm.	Max. Accel. Gradient,[a] x10^{4}sec.$^{-2}$
17	H_2O	3.395	5147	0.23	22.5
34	"	2.830	2904	0.31	10.0
36	"	3.511	2573	0.39	7.5
73	"	1.981	1206	0.46	3.0
41	40.32 wt. % glycerol	3.510	3676	0.31	12.5
45	"	2.970	2492	0.35	7.5
56	57.93 wt. % glycerol	2.589	2412	0.33	7.5
63	"	2.555	1859	0.41	4.5
77	75.13 wt. % glycerol	3.393	2683	0.36	7.5
81	85.17 wt. % glycerol	1.874	861.7	0.51	2.0

[a] A linear approximation was made to the entire corrected acceleration profile.

The rates of change of rate of x-direction shear (in sec.$^{-2}$) were also calculated for the different drops in the liquid-vapor surface region near the three-phase boundary. These acceleration gradients for the drops were zero at ωt = multiples of π, and reached maximum values at ωt = odd multiples of $\pi/2$. The maximum rates of change of rate of shear for the different drops are reported in Table XX. These maximum acceleration gradients were found to be very large and ranged from 2.5×10^4 to 30.0×10^4 sec.$^{-2}$.

For representative drops, the values of these acceleration gradients calculated at different times in the drop oscillation were plotted versus the cosine of the dynamic contact angle at that time. In every case, linear plots were obtained. A typical plot is shown in Fig. 17. The slopes of these plots gave the change of the cosine of the contact angle per change in acceleration gradient in sec.$^{-2}$. The

slopes of these plots for the different drops are reported in Table XXI. The values obtained for these slopes were too scattered to determine any difference between the different mixtures. This distinction would have allowed an estimate of the effect of the inertial forces on the dynamic contact angles in terms of the densities of the mixtures. The slopes were all of the same magnitude with an average of $\sim 3 \times 10^{-6}$ Δ cosine per 1 sec.$^{-2}$. The complete calculated data for these relationships are in Appendix IV.

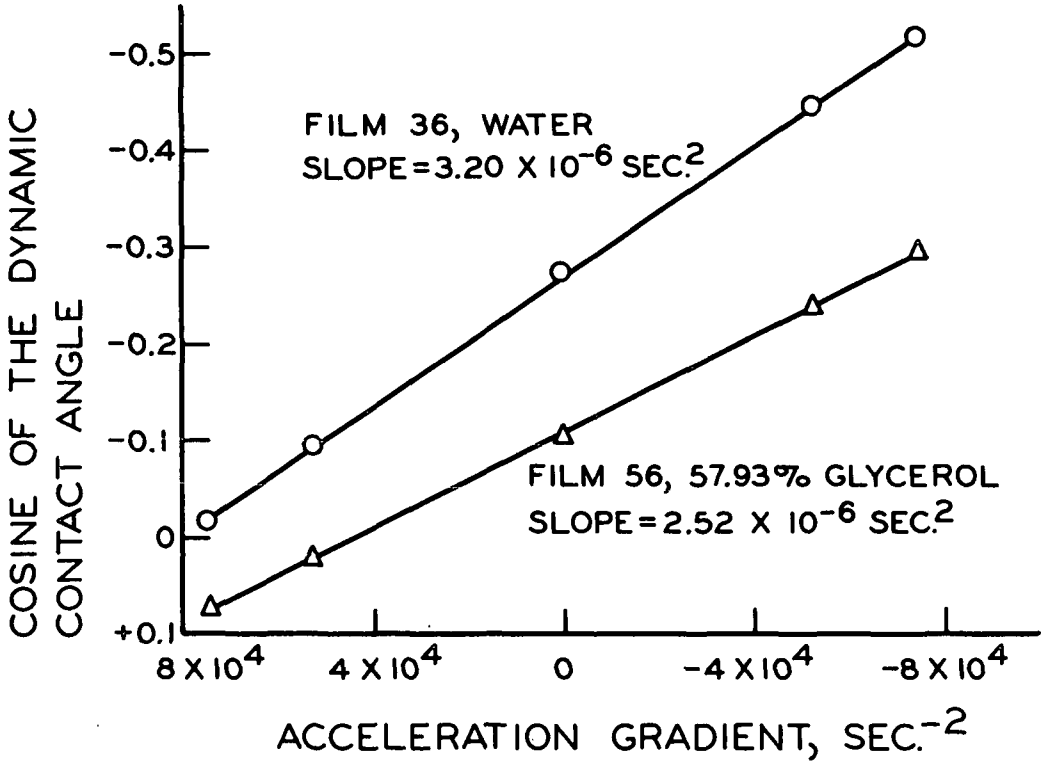

Figure 17. Linear Relationship Between the Cosine of the Dynamic Contact Angle and the Acceleration Gradient

TABLE XXI

SUMMARY OF THE SLOPES OF THE LINEAR RELATIONSHIP BETWEEN THE COSINE OF THE DYNAMIC CONTACT ANGLE AND THE ACCELERATION GRADIENT

Film Number	Mixture	Slope of Cosine of Contact Angle $\frac{\text{vs.}}{\Delta}$ Accel. Gradient, $\times 10^{-6}$ cosine per sec.$^{-2}$
17	H_2O	0.728
34	"	1.18
36	"	3.20
73	"	5.98
41	40.32 wt. % glycerol	1.48
45	"	2.42
56	57.93 wt. % glycerol	2.52
63	"	4.36
77	75.13 wt. % glycerol	2.40
81	85.17 wt. % glycerol	5.58
		average[a] $\sim 3.0 \times 10^{-6}$ per sec.$^{-2}$

[a]The results were too scattered to assign differences in the slopes to the density differences of the mixtures.

DISCUSSION OF RESULTS

THE MODEL OF A DROP OSCILLATING ON A PLANE SURFACE

EQUILIBRIUM DESCRIPTION

The expression of the equation of capillarity in polar coordinates resulted in an equation describing sessile drop shapes that were readily adaptable to integration by numerical methods. The approach used in this study to solve Equation (6) gave tabular form drop shapes that agreed extremely well with experimental data. Very satisfactory results were obtained for the high contact angle drops used in this study. The ranges of drop volumes, surface tensions, and densities were not extreme, but these variables did provide a good test of the approach.

DYNAMIC DESCRIPTION

Shapes

The first test of the validity of the flow model was a direct comparison (computer plotted) of the theoretical drop shapes and the experimental drop shape data at different times in the oscillation. For all the different drop sizes and mixtures, these comparisons were very good. A very slight deviation of the theoretical shape from the experimental shape in the region just above the three-phase boundary was noted for all the drops. This deviation had a fairly large effect on the velocities calculated for that region. However, the velocities in that limited region were very small compared to the flow in the rest of the drop. Therefore, this slight deviation had little effect on the overall energies calculated for the entire oscillating drop systems.

Volumes

Comparison of the volumes resulting from integration of the theoretical expression and integration of the experimental data provided a good test of the model.

The results were presented in Table XII. The agreement between these values was very good and was within 1% in most cases. It can be noted that the theoretically integrated values for the volumes were slightly higher than the volumes integrated from the experimental data. This would be expected since the integration step size was one degree for the theoretical determinations, in contrast to a stepwise of $\sim$ five degrees for the experimental data points. It is quite likely that the theoretical value provided a better estimate of the actual drop volumes than the experimental data integration values.

Gravitational Changes

Comparison of the energy changes of the gravitational motion determined from the experimental data and the theoretical model provided another test of the flow model. The maximum values of these two approaches were presented in Table XIV. The magnitudes of the experimental and the theoretical values were in very good agreement. The theoretical results indicated the gravitational motion was not quite sinusoidal. The experimental results were characterized as sinusoidal. The experimental data from the integration of the experimental shapes were actually only approximately sinusoidal. These data could have easily been characterized by the slightly nonsinusoidal motion predicted by the model. The close agreement of the magnitude of the two approaches provides good support for the flow model.

Decay Times

The comparison of the theoretical decay times and the experimentally determined decay times provided good experimental support for the flow model. These values were compared in Table XVIII. The experimental values were determined by direct measurement of high-speed movies of the decaying oscillation of drops of different liquid mixtures and volumes. The theoretical values were calculated from Equation (21d) for the drops of different mixtures and volumes that were driven in steady-state oscillation. The theoretical decay times were slightly shorter than the

experimental decay times. This would be expected since the calculation of the energy dissipation was a slight overestimate. The good agreement of the values in Table XVIII indicated that the flow model closely described the kinetic energies associated with the actual oscillation behavior of the liquid drops on the plane paraffin surfaces.

EFFECT OF THE MECHANICAL PROPERTIES ON WETTING

ENERGY TRANSFERS IN THE THREE-PHASE BOUNDARY AND THE LIQUID-SOLID INTERFACE

Consideration of Molecular Orientation Requirements

Dynamic Three-Phase Boundaries

The experimental calculations and the values assigned by the flow model (in Table XVI) both indicated there was a difference in the intrinsic energy per cm.^{2} for the liquid-solid interfacial area created in a system with the same solid and liquid but different dynamic contact angles. In addition, because of the steady-state nature of the oscillation of the drops and the lack of hysteresis, these energies were recoverable. Since the liquid-solid interface was created and removed at the three-phase boundary, it is essential to give some consideration to what may be occurring in this region.

Elliot and Riddiford (30) in their 1967 publication proposed a mechanism for the behavior of liquid molecules in the liquid-solid interface in their dynamic system. They advanced a liquid-vapor interface at various constant velocities by causing a puddle of liquid to grow between two narrowly spaced plates. They observed large increases in the dynamic contact angle with increasing velocity. They concluded that, with an increasing velocity of the three-phase boundary, there were increasing numbers of disoriented liquid molecules in that region. This molecular disorientation led to higher contact angles, and a maximum dynamic contact angle was obtained when all the molecules in this region were disoriented. For

water on siliconed glass, they reported this maximum disorientation was obtained at a velocity of 8 mm./min.

In their analysis, they referred to a "velocity of the three-phase boundary" as the fluid flowed between the plates. Actually, because of the behavior of liquids (i.e., no slip at the wall), there is no velocity associated with the three-phase boundary region. The liquid molecules that are placed in the three-phase boundary region have a zero velocity when they reach that point. However, there is a rate of formation of liquid-solid interfacial area. This area is initially formed at the three-phase boundary, and the rate of formation of new liquid-solid area is determined by the velocity of the fluid stream.

The idea of the orientation of molecules in the three-phase boundary region is important, and it is the key to understanding liquid-solid interfacial energies in dynamic wetting. However, the orientation effect described by Elliot and Riddiford (30) is not reasonable for rapidly relaxing liquid molecules such as water [$\sim 10^{-6}$ sec. at a liquid-solid interface (45)] at the flow rates they studied. If the velocity of a rapidly relaxing liquid molecule is zero relative to the solid surface when it is placed in the three-phase boundary region, it would be able to immediately align itself to the orientation requirements placed on it.

The physical forces of attraction which give rise to the surface tension of a liquid will result in a constant surface tension for the liquid even during the creation of new liquid surface area, if the relaxation times of the liquid molecules are great relative to the rates of surface formation. This constant surface tension has been shown to be true for water at very rapid rates of surface formation (49). The average energy of a particular solid surface will remain constant, and the direction of the attractive forces in this surface will remain constant because of the immobility of the solid surface molecules. If a liquid is caused to move over

a solid surface, the fluid flow characteristics result in a change in the curvature of the free liquid surface due to a changed pressure distribution at this surface. Because of the continuity of the free surface, a change in the curvature of the free surface results in a change in the contact angle from its equilibrium value. With a constant liquid surface tension and a constant solid surface energy, the only change in the dynamic system regarding the liquid-solid interface is a change in the direction of the liquid surface tension forces acting on the three-phase boundary region. The change in direction of these forces is reflected in the dynamic contact angle. If the liquid molecules in the three-phase boundary region have rapid relaxation times, they will orient immediately to the required relationship of the forces acting on them. Changing orientation requirements for the liquid molecules in this region implies changing energies associated with the liquid-solid interface area in this specific region. An instantaneous force balance applied to the three-phase boundary region will indicate the nature of the energy change in this region. This effect on the three-phase boundary region is shown in Fig. 18.

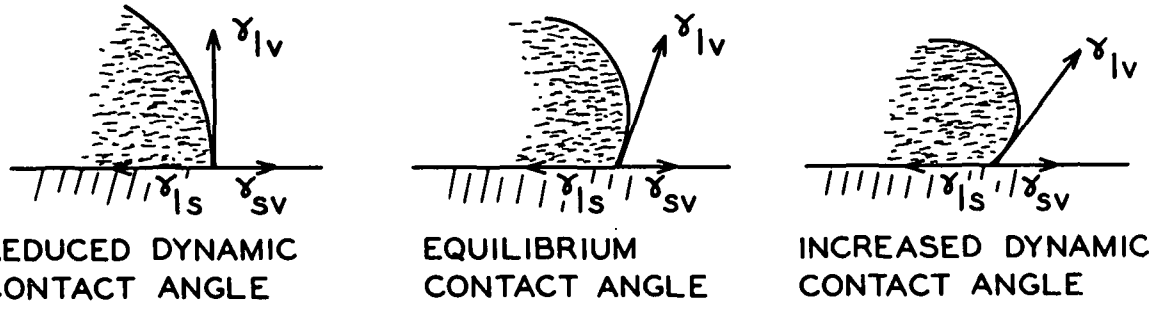

Figure 18. Fluid Flow Effects on the Free Surface Curvature and the Resulting Change in Direction of the Surface Forces

The approach of Elliot and Riddiford indicated that increasing velocity of an advancing three-phase boundary led to increasing disorientation of the liquid molecules in this region. In turn, the molecular disorientation resulted in higher dynamic contact angles. In contrast, the viewpoint expressed here simply implies that the

energy differences in the three-phase boundary region result from different orientation requirements, not increasing disorientation. A dynamic contact angle greater than the equilibrium value would result in a greater energy associated with this region. Likewise, a dynamic contact angle less than the equilibrium value would result in a lesser energy associated with this region.

This viewpoint further implies that the energy changes associated with this region can be predicted in any case where the nature of the fluid flow and its effect on the liquid-vapor curvature can be characterized. This is true if the liquid molecules in this region can orient rapidly enough to meet the requirements predicted by the flow expressions. If some of the molecules cannot meet these orientation requirements, a dynamic surface tension effect will occur in that region. In such a case, the energies associated with that region will, in reality, be higher than the energies predicted by the fluid flow expressions.

Support for this viewpoint is found in the work of Rose and coworkers (24, 25, 26). In these studies, free liquid surfaces and liquid-liquid interfaces were advanced through glass capillary tubes at various constant velocities. In every case, linear relationships were found between the cosines of the measured contact angles at the solid-liquid interfaces and the steady-state velocity of the liquid. In tube flow at low velocities, constant velocity gradients would be expected from the wall to the center of the tube (50). Such a velocity distribution would give rise to a linear pressure distribution and would change the free liquid surface or liquid-liquid interfacial curvature accordingly. The cosine of the contact angle is a measure of the direction in which the liquid surface tension forces are acting relative to the solid forces at the contact point. The magnitude of the steady-state fluid velocity would be direct measurement of the linear velocity profile existing in the tube. In their studies, an incremental increase in the viscous shear gradient and its effect on the curvature of the free surface was met by an

incremental decrease in the cosine of the contact angle. The linear relationship indicated that, in the systems they studied, the liquid molecules in the three-phase boundary region were able to meet the higher energy orientation requirements placed on them without any measurable disorientation of the liquid molecules. In their studies, they used Nujol-air-glass and oleic acid-air-glass systems. They studied the dynamic contact angle effects in tubes of 0.033 and 0.050-cm. diameters with steady-state velocities ranging from zero to 0.23 cm./sec.

Resulting Liquid-Solid Interfaces

The orientation of liquid molecules in the three-phase boundary region and the effect of fluid dynamics on the energy of the liquid-solid interfacial area of that specific region have been discussed. Further consideration must be given to the nature of liquid-solid interfacial areas that have been initially formed in a "dynamic" three-phase boundary region and are then allowed to relax to some kind of "equilibrium" relationship as the boundary moves on. Again, it should be noted that no velocity relative to the solid surface is associated with the liquid molecules in this region. However, the relationship between these molecules and the solid surface is greatly affected by the fluid flow effects on the curvature of the free surface above the contact point. The nature of the structure of a real solid surface will also have a large effect on the character of the liquid-solid interface that is formed from a dynamic three-phase boundary.

However, first consider a solid surface that is completely smooth on a molecular scale. The previous history of liquid molecules in a liquid-solid interface on such a surface would have no effect on the resulting interfacial energy. Regardless of what the orientation requirements were in the three-phase boundary as the interface was being formed, complete contact would be made between the liquid and solid molecules. As soon as the liquid molecules were out of the boundary region, they would relax to the equilibrium relationship. There would be complete

contact between the liquid and solid, and the same wetting or adhesion would result regardless of the dynamic conditions that produced the interface. In spite of this end result, it should still be possible to "store" different amounts of potential energy in such an interface. If a liquid drop is oscillating on such a surface, dynamic contact angles will be observed because of the no slip condition at the wall and the pressure effects on the curvature of the free surface. As the drop goes from its median to down position, the orientation requirements of the liquid molecules in the boundary region result in higher energy relationships between the liquid-solid molecules in that region. Although complete contact is occurring between the liquid and solid molecules, the liquid-solid area is being created at an increasing energy expenditure of the rest of the oscillating drop system. When the drop reaches its down position, the liquid molecules in the newly created liquid-solid area no longer in the boundary region will have relaxed to the equilibrium relationship and given off some heat in the process. The energy expended by the rest of the system to create this area is not literally "stored" as potential energy in this newly created area. However, this area and the greatly increased dynamic contact angle do represent energy that is recoverable. As the drop moves from its down position toward the median configuration, it is removing liquid-solid interfacial area. As the liquid molecules find themselves in the boundary region again, they must reorient to the forces acting on them (reflected by the dynamic contact angle). These molecules most likely pick up heat to meet the orientation requirements of the boundary. They are then more easily removed from the solid surface than the equilibrium relationship would indicate. The greater ease of removal of these molecules represents an energy gain to the system that is equal to greater energy (compared to the equilibrium relationship) than was necessary to create this liquid-solid area.

This same reasoning applies to the liquid-solid area that is created and removed in the phases of the oscillation between the up and median configurations. Because

of the orientation requirements in the boundary region, that area is created with less energy than the equilibrium relationship would indicate. Therefore, less potential energy is "stored" in that area. This is reflected in the increased difficulty of removal of these liquid molecules and, therefore, a lower energy gain by the rest of the system than the equilibrium relationship would indicate.

Real solid surfaces are not likely to be smooth on a molecular scale. The effect of macroscopic roughness (i.e., the surface asperities are of significant size when compared to the size of the liquid drops) of the solid surface on equilibrium contact angles, and the measured hysteresis between advanced and receded equilibrium contact angles have been investigated and discussed by many researchers (10-14). Other researchers (20) have reported equilibrium studies done on "smooth" surfaces. No hysteresis was observed between advanced and receded equilibrium contact angles on these surfaces. The paraffin surfaces used in this oscillating drop study were of this type of "smooth" surface. These surfaces were not really smooth in a molecular sense. These smooth surfaces can be referred to as being "microscopically rough."

The effect of this roughness on the nature of liquid-solid interfaces created under dynamic conditions would be considerable. Higher energy orientation requirements at a three-phase boundary (i.e., a dynamic contact angle that is higher than the equilibrium value) would decrease the amount of intimate liquid-solid molecule contact in the boundary region. When this area was no longer in the boundary region and the liquid molecules relaxed, there would be areas of entrapped air. That is, the liquid-solid interface would be heterogeneous. The energy of this interfacial area would necessarily be of higher energy than the equilibrium value would indicate. This energy difference would be recoverable when the liquid molecules are removed from the solid. Likewise, it is expected that the lower energy orientation requirements of liquid molecules in three-phase boundary characterized by a dynamic contact

angle less than the equilibrium value would lead to a more intimate association than the equilibrium relationship. This would result in the creation of a liquid-solid interface that is less heterogeneous and of lower energy than the equilibrium interface.

In the case of a drop oscillating on a microscopically rough surface, it is expected that the actual energy of the liquid-solid interfacial area created under different orientation requirements at the three-phase boundary would have different values. The area involved in the up to median phases of the oscillation would have less entrapped air and a lower energy per $cm.^2$. The area involved in the median to down configurations would have more entrapped air and a higher energy per $cm.^2$

This reasoning also implies that the median configuration and the equilibrium contact angle of pure liquids on low energy microscopically rough surfaces do not necessarily indicate the real energy relationship between the liquid and solid (i.e., the result that would be observed if the solid surface were molecularly smooth). When the liquid drop is placed on the microscopically rough surface, some liquid-vapor regions will still exist in the liquid-solid interface. This will make the experimentally observed result give a slightly higher energy to the liquid-solid attraction forces than one would obtain if the total interaction in this interfacial area were due solely to liquid-solid molecule attraction forces. This effect may be the cause of the differences obtained between Fowkes' calculation (32) for solid surface energies [when applicable (33)] and Zisman's critical surface tension (34) determinations. Based on an observed contact angle, Fowkes' method gives a lower energy to a "smooth" solid surface of paraffin than Zisman's critical surface tension plot [25.5 and 32.5 ergs $cm.^{-2}$, respectively (32, 33)]. This difference could result from Fowkes' assumption that the liquid-paraffin interface is composed solely of liquid-solid interactions.

Experimental and the Model Calculations

The energies associated with the creation and removal of liquid-solid interfacial area determined from the flow model and experimental calculations were reported in Table XVI. These values in ergs cm.$^{-2}$ represented the energy associated with the liquid-solid area involved between the extreme up and median configuration and the area involved between the median and extreme down configuration. The calculations based on the model were not direct calculations of these energies but values determined by calculating the other potential energies of the system and assigning the differences between these potential energies and the kinetic energy to the liquid-solid region. These relationships were calculated from the model for all the drops at the extreme up and down configurations. The energies assigned to the liquid-solid region in these two configurations represented the total amount of energy involved in the changes in liquid-solid area between these two configurations and the median configuration. The model calculations indicated that total liquid-solid interfacial energy between the up and median configurations was about one half the total liquid-solid interfacial energy between the median and down configurations for all the drops. If the liquid-solid area changes were approximately the same between the median and extreme configurations, these results imply that the energy per cm.^{2} associated with liquid-solid interfaces from the median to down position was greater (approximately twice) than that for the median to up position.

The experimental data for the motion of the drop edges were very close to sinusoidal. The amplitudes of this motion for the different drops were reported in Table V. A sinusoidal edge motion would give a slightly greater area change from equilibrium to down than from equilibrium to up, but the difference is very small ($\sim$ 1.5%). Error analysis indicated that the error in these amplitudes could be quite high. However, they were used as the best available estimate of the magnitude of the change in liquid-solid interfacial area. Average values for

the energies per cm.^{2} for the two liquid-solid areas involved in the change between up and median and median and down positions were calculated for the different liquids based on the experimental dynamic contact angle changes and Equation (1) (the Young equation). These values were reported in Table IX. These energies and the amplitudes of edge motion were used to calculate the energy changes due to area changes of the liquid-solid interface. These changes for all the drops at the up and down configurations were reported in Table XVI. The magnitude of these values for the energy changes agreed well with those assigned by the flow model. Particularly, it was noted that the average energies per cm.^{2} for the liquid-solid area change from the median to down positions were also $\sim$ twice those for the area change from the up to median positions.

The calculations based on the flow model and the calculations based on the drop edge motion and dynamic contact angles for the liquid-solid interfacial energies of drops oscillating on "smooth" paraffin surfaces gave good support to the proposed energy transfers in the three-phase boundary region. The experimental results indicated the dynamic contact angles that were less than the equilibrium values in the phases of drop oscillation between the up and median positions did, indeed, have liquid-solid interfacial energies associated with them that were less than the equilibrium interfacial energies. The phases of the drop oscillation between the median and down positions and the increased dynamic contact angles relative to the equilibrium values did, indeed, have liquid-solid energies associated with them that were higher than the equilibrium values. Since the "smooth" paraffin surfaces were actually microscopically rough, some of the energy differences in the interfacial liquid-solid energies were most likely due to differences in the heterogeneity of the interfacial region. That is, there was probably less entrapped air in the areas created under the decreased dynamic contact angle conditions and more entrapped air in the areas created under the increased dynamic contact angle conditions. The

liquid molecules that were actually in contact with solid molecules most likely behaved in the manner discussed for the energy transfers under dynamic conditions on a molecularly smooth surface. That is, they oriented to the specific requirements in the three-phase boundary when in the boundary and relaxed to the equilibrium relationship when not in the boundary. This would be their necessary behavior, since the experimental results indicated no hysteresis effects. Therefore, all the energy transferred into the liquid-solid interface had to be recoverable.

Median Dynamic Contact Angle Results

A comparison of the median dynamic contact angles and the equilibrium contact angles for each liquid mixture provided an interesting test of the proposed theory of changing orientation requirements at a three-phase boundary under dynamic conditions. The relaxation time of water molecules at liquid-solid interfaces has been shown to be about 10^{-6} sec. (45). This relaxation time is very rapid with respect to the vibrational frequencies of the drops in this study. The oscillation of the drops in this study showed no hysteresis. That is, they passed through the same configurations going from up to down as they did going from down to up. A rapidly relaxing molecule like water would be able to immediately meet the changing orientation requirements in the three-phase boundary region. Since no disorientation of water molecules would be occurring at the boundary region, the median or "equilibrium" shape of the oscillating drop would be expected to correspond exactly with the true equilibrium drop shape. This means that the same value should be obtained for the equilibrium contact angle and the median dynamic contact angle. Figure 8 showed a plot of the cosines of the median dynamic contact angles and the equilibrium contact angles versus the composition of the drops. The median dynamic values and the equilibrium values were found to be the same for water and the lower glycerol content drops. This indicated that the molecules in those mixtures were able to relax rapidly and meet the changing orientation requirements at the three-phase boundary.

No literature values were available for the relaxation times of glycerol molecules. However, the literature did indicate that with higher concentrations of glycerol in water (> 60% by weight), the glycerol-water complex becomes almost polymeric in nature (51, 52). On this basis, a great reduction would be expected in the ability of the glycerol-water complex to relax rapidly. The experimental data in Fig. 8 showed a slight but significant increase in the dynamic median contact angles compared with the equilibrium values for the glycerol in water mixtures greater than ∿ 65%. This would indicate a slight general increase in the energy of the three-phase boundary region due to the inability of some of the molecules of the glycerol-water complex to meet the changing orientation requirements placed on them.

RELATIVE EFFECTS OF VISCOSITY AND INERTIA IN THIS STUDY

The general effect of fluid viscosity was important in this work because the viscous behavior of fluids necessitates a zero velocity at the solid boundary. This effect of viscosity was approximated in the flow model by the proper selection of coefficients for the Legendre series describing the perturbations of the oscillating drops. In previous studies of dynamic contact angles the investigators observed the dynamic contact angles under conditions of steady flow (constant velocity) of the fluid. Rose and coworkers (24-26) reported a linear relationship between the cosine of the contact angle and the fluid velocity of liquid-vapor interfaces advancing with constant velocity through capillary tubes. In this case, the changes in the curvature of the free surface were the direct result of the linear velocity gradients existing in the region of the tube wall. That is, the dynamic contact angles observed depended entirely on the viscous behavior of the fluid. The dynamic contact angles observed by Elliot and Riddiford (29, 30) under steady flow conditions should also be considered as resulting from the viscous behavior of the fluid.

In the case of the oscillating drops in this study, the oscillation was steady state, but the nature of the fluid flow was not steady. The motion (actually rate of formation) of the three-phase boundary was very small for these drops. No hysteresis of the dynamic contact angles was observed for the oscillating drops. Therefore, the viscous effects near the solid boundary were very small and were not measurable in the drops in this study.

The large changes in dynamic contact angles measured in this study were almost entirely due to inertial forces. The inertial forces arose from the very large and rapidly changing acceleration gradients present in the fluid in the region of the solid surface near the edge of the drops. The acceleration profiles actually existing in these regions most likely were not linear. However, to a good approximation, the acceleration gradients existing at any given time were characterized as constant. The acceleration profiles calculated on the basis of the model were used to correct the slight deviation of the model from the data in this region. A linear relationship was found between the corrected acceleration gradients and the values of the cosine of the dynamic contact angles at different times in the oscillation for the drops. The slopes of these plots gave the change in the cosine of the dynamic contact angle associated with a change in the acceleration gradient in the region above the solid surface. These slopes were reported in Table XXI. These results were varied. It was not possible to distinguish specific differences in these slopes that could be associated with the density differences of the mixtures. An average value for the drops in this study gave a change of $\sim 3 \times 10^{-6}/\text{sec.}^{-2}$ change in the acceleration gradient. The acceleration gradient referred to here was the gradient of $\underline{x}$-direction (parallel to the solid surface) accelerations existing in liquid-vapor interface in the region immediately above the three-phase boundary. This value was assumed to be a reasonable estimate of the magnitude of the relationship actually existing in the drops in this study. The implication is

that a slight increase in contact angle is associated with an increase in the rate of deceleration of a liquid flowing on a solid surface. The linear relationship obtained between the cosine of the contact angle and the acceleration gradient indicated that an incremental increase in the deceleration gradient caused an incremental increase in the direction of the liquid surface tension forces acting on the liquid molecules in the three-phase boundary.

In this study with oscillating drops, the inertial effects on the dynamic contact angles were so great they masked the viscous effects. However, the use of larger drops and lower surface tension liquids should give a system which would allow much greater motion of the three-phase boundary. In such a case, large viscous effects would be expected. Hysteresis of the dynamic contact angles should be observed which would be the result of the viscous behavior of the fluid motion under nonsteady flow conditions.

CONCLUSIONS

FLOW MODEL FOR A DROP OSCILLATING ON A PLANE SURFACE

The approach to the solution of the equilibrium configuration of a sessile drop on a plane surface used in this study gave excellent results when compared with experimental drop shape data. This approach involved the numerical integration of the second-order differential obtained when the equation of capillarity was expressed in spherical coordinates. The perturbations about the equilibrium form when such a drop was driven in steady-state oscillation in its first mode were successfully described using Legendre polynomials. This dynamic description allowed the development of a complete theoretical flow model. Good agreement was obtained between the theoretical and experimental drop shapes, volumes, decay times, and changes in gravitational potential energy. On the basis of these comparisons, it was concluded that the theoretical model presented in this study for the steady-state oscillation of a drop on a plane surface provided a good description of the real phenomena.

MECHANICAL EFFECTS IN DYNAMIC WETTING SITUATIONS

It was concluded in this study that the relationship existing between the liquid and solid molecules in the three-phase boundary region determined the nature of the liquid-solid interface that is formed under dynamic conditions on a real solid surface (at least microscopically rough). It has been proposed that dynamic contact angles greater than the equilibrium values place higher orientation requirements on the liquid molecules in the three-phase boundary region. Liquid molecules in contact with the solid in this region would relax to the equilibrium relationship when the boundary has passed. However, on a real surface the higher energy orientation requirement in the boundary will allow less contact between liquid and solid molecules. The liquid-solid interfacial area formed under such conditions will

necessarily have more entrapped vapor than the equilibrium interfacial area. That is, increasing dynamic contact angles will lead to more heterogeneous and higher energy liquid-solid interfacial areas. In a like manner, dynamic contact angles less than the equilibrium values will lead to less heterogeneous and lower energy interfacial areas.

This proposed effect of the boundary region was substantiated by the results from the oscillating drops in this study. The liquid-solid interfacial energies assigned by the flow model and the energies determined from the experimental edge amplitudes and dynamic contact angles indicated that the energy per $cm.^2$ associated with the creation or removal of liquid-solid interfacial area between the up and equilibrium configurations was about 1/2 that associated with the area created or removed in equilibrium to down configurations. The reduced interfacial energy was associated with reduced dynamic contact angles. The increased interfacial energy was associated with increased dynamic contact angles. It is reasonable to assume that a good portion of these energy differences was due to differences in the heterogeneity of the liquid-solid interfacial area created on the microscopically rough paraffin surfaces.

It was further concluded that the orientation requirements in the three-phase boundary were directly the result of the nature of the fluid flow and its effect on the curvature of the liquid-vapor interface. The mechanical forces acting on the free surface can be strictly viscous forces as shown in the work of Rose and coworkers (24-26) and their studies of steady flow in capillary tubes. These mechanical forces can also be inertial forces arising from the rapidly changing nature of unsteady flow such as those found for the oscillating drops in this study.

Finally, it was concluded that if the liquid molecules in the three-phase boundary region can relax rapidly to meet the orientation requirements placed on

them, the energy relationship between the liquid and solid molecules in this region can be predicted by the description of the fluid flow. However, if some molecules cannot relax rapidly to meet these requirements, some disorientation of liquid molecules in the boundary will result. This will tend to raise the energy of the region and the experimental dynamic contact angles will be higher than can be predicted by the flow description. This effect was observed in a comparison of the median dynamic contact angles and the equilibrium contact angles for the drops in this study. These values were the same for drops of the rapidly relaxing water molecules and the lower glycerol content drops. However, the higher glycerol content drops (65%) had median dynamic contact angles that were slightly higher than the equilibrium contact angles. This indicated that some molecules in the glycerol-water complex in these cases were not able to relax rapidly enough to meet the orientation requirements. This resulted in a slightly higher energy associated with the three-phase boundary region.

PRACTICAL APPLICATION OF THE RESULTS

It was seen in this study that the characteristics of the fluid flow in a dynamic wetting situation can greatly affect the nature of the liquid-solid interface. This effect was seen to be the result of changes in the orientation requirements of liquid molecules in the three-phase boundary region due to flow effects on the curvature of the free surface. In the case of the oscillating drops in this study, wetting was actually improved because of reduced dynamic contact angles in some phases of the oscillation. However, in industrial processes involving the wetting of liquids applied to solids, it is hard to conceive of a situation where the dynamic contact angles are reduced from their equilibrium values. Such angles would be associated with receding three-phase boundaries or removal of the liquid from the solid. Most industrial processes involving wetting are concerned with advancing boundaries. If the industrial wetting process is considered in terms of

the nature of the three-phase boundary effects concerned in this study, the dynamic effects on wetting in such a case are very great. For example, in many coating operations the fluid velocity is extremely large relative to the sheet. The viscous effects on the curvature of the free surface would greatly increase the energy of the three-phase boundary. In addition, the amount of molecular disorientation in this region could be large. Finally, the solid surface in this case would be macroscopically rough. These effects will greatly increase the resulting liquid-solid interfacial energy and, therefore, greatly reduce the quality of the wetting. The best wetting situation that can be achieved on application of a liquid to a solid is the equilibrium relationship between the liquid and solid. Depending on the particular operation, it should be possible to design equipment that will apply the liquid to the solid so that the liquid velocities at application are approximately the same as the solid's velocity. This would greatly reduce the shear stresses in the region of the three-phase boundary and would lessen the dynamic effects on the resulting wetting.

FUTURE WORK

In this study it was not possible to get a highly accurate measurement of the drop edge motion because this motion was extremely small. The potential energy of the liquid-solid interface was determined from the model by calculating the other potential energies of the system (liquid-vapor and gravitational). The change in potential energy from the equilibrium value at the extreme up and down positions had to equal the maximum kinetic energy of the system. Therefore, the differences between the maximum kinetic energy and the potential energy changes from equilibrium of the liquid-vapor surface and the gravitational motion in the extreme positions of the drop were assigned to the liquid-solid interface. Experimental values for the liquid-solid energy changes based on the dynamic contact angles and measured edge motion agreed quite well with the values assigned by the model. However, highly accurate measurements of the edge motion would allow the calculation of much more accurate values for these changes based on the experimental information. The maximum kinetic energy was calculated with the theoretical integral expression using the experimental vibrational frequency. If experimental values for the liquid-solid energy changes could be put in the energy balance, the vibrational frequency could be used as the only unknown. This would allow the solution for theoretical vibrational frequencies which could be compared with the experimental values. This would give a very sensitive check on the experimental calculations of the energy effects in the three-phase boundary region.

The accuracy of the edge measurement can only be improved by investigating oscillating drop systems where this motion is much greater than in this study. This increased motion should be obtainable using larger drops and lower surface tension liquids. It was indicated in this study that a larger edge motion should also produce measurable viscous effects. These viscous effects would result in a

hysteresis of the contact angle between the advancing and receding phases of the oscillation. This flow situation would be somewhat more difficult to describe. However, it should be possible to describe such a flow situation with Legendre functions having coefficients with different phase dependencies.

Finally, the oscillating drop on a plane surface presents itself as a useful tool in investigating any phenomenon involving surface tension or volume. The frequency of the vibration of a drop on a planar surface is extremely sensitive to the surface tension and/or the drop volume. Frequency changes would be a good way to follow movement of slowly diffusing materials into the surface of drops. It was noted during the course of this work that oscillating drops of water evaporated many times faster than sessile drops (at normal R.H.). The vibrational frequencies provide a good way to determine volume changes with time under various conditions.

ACKNOWLEDGMENTS

The author would like to express his appreciation to J. W. Swanson, R. W. Nelson, and H. Meyer for the many helpful discussions in the course of this work.

The scholarship support received from The Institute of Paper Chemistry throughout his studies is gratefully acknowledged by the author.

NOMENCLATURE

$\underline{AH}$ = amplitude of the drop top motion in cm.

$\underline{A_n}$ = coefficient of $\underline{n}$th term in the Legendre series describing drop shape (has units of cm.)

$\underline{B_n}$ = coefficient of $\underline{n}$th term in the Legendre series describing the velocity potential [has units of $\text{cm.}^{-(\underline{n}-2)}$]

$\underline{b}$ = radius of curvature at the top of a sessile drop

$\underline{e}$ = base of natural logarithms

$\underline{2F}$ = viscous energy dissipation in ergs

$\underline{g}$ = gravitation constant in g. cm./sec.^{2}

$\underline{I}$ = energy in ergs added to the oscillating drop by the drive coil in 1/4 cycle

$\underline{n}$ = an integer

$\underline{P_n}$ = Legendre polynomial of degree $\underline{n}$

$\underline{Q}$ = energy in ergs dissipated by an oscillating drop in 1/4 cycle

$\underline{R}$ = radial distance from origin to the equilibrium surface of a sessile drop (a function of θ)

$\underline{R_1}$ & $\underline{R_2}$ = the principal radii of curvature of a sessile drop

$\underline{R_s}$ = the integrated value of $\underline{R}$ from $\theta = 0$ to $\pi/2$

$\underline{r}$ = radial spherical coordinate, cm.

$\underline{S}$ = a function of θ and $\underline{t}$ describing the perturbations of the free surface of an oscillating drop about its equilibrium form

$\underline{T}$ = kinetic energy in ergs of an oscillating drop

$\underline{t}$ = time in seconds

$\underline{V_1}$ = total potential energy in ergs of the liquid-vapor interface of a drop on a plane surface

$\underline{V_2}$ = total gravitational energy in ergs of a drop on a plane surface relative to the origin

$\underline{V_3}$ = total potential energy in ergs of the liquid-solid interface of a drop on a plane surface

$\underline{W_{sl}}$ = work required to separate a liquid from a solid in ergs/cm.^{2}

$\gamma_{\underline{l}}^{(\underline{d})}$ = contribution of the dispersion forces of a liquid to an interfacial energy in ergs/cm.^{2}

$\gamma_{\underline{lv}}$ = equilibrium surface energy of the liquid-vapor interface in ergs/cm.^{2}

$\gamma_{\underline{s}}^{(\underline{d})}$ = contribution of the dispersion forces of a solid to an interfacial energy in ergs/cm.^{2}

$\gamma_{\underline{sl}}$ = surface energy of the solid-liquid interface in ergs/cm.^{2}

$\gamma_{\underline{sv}}$ = surface energy of the solid-vapor interface in ergs/cm.^{2}

$\gamma_{\underline{sv}^o}$ = surface energy of the solid surface in a vacuum in ergs/cm.^{2}

η = fluid viscosity in poise

θ = spherical coordinate, the polar angle in degrees

μ = cosine θ

$\pi_{\underline{e}}$ = equilibrium film pressure of adsorbed vapor on a solid in ergs/cm.^{2}

ρ = density in g./cm.^{3}

τ = decay time in seconds in which a nondriven drop reaches $1/\underline{e}$ of its original amplitude

Φ = the stream function as a function of $\underline{r}$ and θ in cm.^{3} sec.$^{-1}$

ϕ = contact angle between a liquid and solid in degrees

ψ = the velocity potential as a function of $\underline{r}$ and θ in cm.^{2} sec.$^{-1}$

ω = circular frequency of drop vibration in radians/sec.

LITERATURE CITED

1. Laplace, P. Mechanique celeste, suppl. 10 (1806); Advances in Chemistry Series No. 43. p. 1. Washington, D. C., American Chemical Society, 1964.

2. Young, T., Phil. Trans. Roy. Soc. (London) 16:65(1805); Advances in Chemistry Series No. 43. p. 2. Washington, D. C., American Chemical Society, 1964.

3. Lester, G. R., J. Colloid Sci. 16:315(1961).

4. Dupré, A. Theorie mechanique. Paris, Gauthier-Villors, 1869. 369 p.; Advances in Chemistry Series No. 43. p. 3. Washington, D. C., American Chemical Society, 1964.

5. Bangham, D. H., and Razouk, R. I., Trans. Faraday Soc. 33:1459(1937).

6. Bangham, D. H., Trans. Faraday Soc. 33:805(1937).

7. Bartell, F. E., and Bristol, K. E., J. Phys. Chem. 44:86-101(1940).

8. Yarnold, G. D., Proc. Phys. Soc. (London) 58:120-5(1946).

9. Yarnold, G. D., and Mason, B. J., Proc. Phys. Soc. (London) 62B:121-8(1949).

10. Wenzel, R. N., J. Phys. Colloid Chem. 53:1466(1949).

11. Cassie, A. B. D., and Baxter, S., Trans. Faraday Soc. 40:546(1944).

12. Shuttleworth, R., and Bailey, G. L. R., Disc. Faraday Soc. 3:16-22(1948).

13. Johnson, R. E., Jr., and Dettre, R. H. Advances in Chemistry Series No. 43. p. 112. Washington, D. C., American Chemical Society, 1964.

14. Dettre, R. H., and Johnson, R. E., Jr. Advances in Chemistry Series No. 43. p. 136. Washington, D. C., American Chemical Society, 1964.

15. Johnson, R. E., Jr., and Dettre, R. H., J. Phys. Chem. 68:1744(1964).

16. Dettre, R. H., and Johnson, R. E., Jr., J. Phys. Chem. 69:1507(1965).

17. Schwartz, A. M., Rader, C. A., and Huey, E. Advances in Chemistry Series No. 43. p. 250-67. Washington, D. C., American Chemical Society, 1964.

18. Ablett, R., Phil. Mag. 46, no. 272:244-56(Aug., 1923).

19. Elliot, T. A., and Leese, L., J. Chem. Soc. 1957:22-30.

20. Elliot, T. A., and Leese, L., J. Chem. Soc. 1959:1466-74.

21. Knight, G. D. Doctor's Dissertation. Appleton, Wis., The Institute of Paper Chemistry, 1947. 90 p.

22. Barrer, R. M., Disc. Faraday Soc. 3:61-72(1948).

23. Brittin, W. E., J. Appl. Phys. 17:37-44(1946).

24. Rose, W., and Heins, R. W., J. Colloid Sci. 17:39-48(1962).

25. Rose, W., Nature (London) 191:242-3(1961).

26. Rose, W., Chaudhari, N., and Fara, H., Z. Physik. Chem. Neue Folge 34:182-97 (1962).

27. McIntyre, D. E., and Swanson, J. W. Unpublished work. Appleton, Wis., The Institute of Paper Chemistry, 1965.

28. Richards, N. J., and Swanson, J. W. Unpublished work. Appleton, Wis., The Institute of Paper Chemistry, 1966.

29. Elliot, G. E. P., and Riddiford, A. C., Nature 196:795-6(1962).

30. Elliot, G. E. P., and Riddiford, A. C., J. Colloid Interface Sci. 23:389-98 (1967).

31. Hansen, R. S., and Miotto, M., J. Am. Chem. Soc. 79:1765(1957).

32. Fowkes, F. M. Chemistry and physics of interfaces. p. 2-3. Washington, D. C., American Chemical Society, 1965.

33. Phillips, M. C., and Riddiford, A. C., J. Colloid Interface Sci. 22:149-57 (1966).

34. Zisman, W. A. Advances in Chemistry Series No. 43. p. 11-22. Washington, D. C., American Chemical Society, 1964.

35. Mack, G. L., and Lee, D., J. Phys. Chem. 40:169-76(1936).

36. Adamson, A. W. Physical chemistry of surfaces. p. 1-50. Easton, Pa., Interscience, 1963.

37. Rayleigh, John W. S. The theory of sound. p. 371-5. New York, Dover, 1945.

38. Lamb, Sir H. Hydrodynamics. p. 473-5. New York, MacMillan Co., 1945.

39. Dwight, H. B. Tables of integrals and other mathematical data. p. 192-3. New York, MacMillan Co., 1947.

40. Ref. (38), p. 118.

41. Miner, C. S., and Dalton, N. N. Glycerol. p. 240-1. New York, Reinhold, 1953.

42. Hodgman, C. D., Weast, R. C., and Selby, S. M. Handbook of chemistry and physics. 42nd ed. p. 2179, 2212. Cleveland, Chemical Rubber Pub. Co., 1960.

43. Ref. (38), p. 639-41.

44. Ref. (32), p. 3, 8.

45. Bockris, J. O'M., Mehl, W., Conway, B. E., and Young, L., J. Chem. Phys. 25:776(1956).

46. Ref. (38), p. 118-19.

47. Ref. (38), p. 127-8.

48. McCracken, D. D., and Dorn, W. S. Numerical methods and fortran programming. New York, Wiley and Sons, 1964. 172 p.

49. Vandegrift, A. E., J. Colloid Interface Sci. 23:43-5(1967).

50. Bird, R. B., Stewart, W. E., and Lightfoot, E. N. Transport phenomena. p. 3-4. New York, Wiley and Sons, 1963.

51. Dumanskii, I. A., and Khailenko, L. V., Kolloid. Zh. 22:277-81(1960); C.A. 55:8982h.

52. Dumanskii, I. A., and Khailenko, L. V., Kolloid. Zh. 23:684-6(1961); C.A. 57:84e.

53. Johnson, R. E., J. Phys. Chem. 63:1655(1959).

54. Defay R., Prigogine, I., Bellemans, A., and Everett, D. H. Surface tension and adsorption. New York, Wiley and Sons, 1966.

55. Ref. (38), p. 579-81.

APPENDIX I

MATERIALS

PURIFICATION PROCEDURES

WATER

The water used in this study was distilled, in succession, from a dilute permanganate solution, a dilute H_2SO_4 solution, and a final straight distillation. The starting material was water obtained from a large, general use, still. The pure water was stored in clean, glass bottles. (All glassware in this study was cleaned by boiling in concentrated sulfuric acid solution saturated with potassium dichromate.)

PARAFFIN

Sun Oil paraffin wax number 5512 (m.p. 158-160°F.) was used in this study. This material was further processed to remove any polar impurities. A 300-ml. Allihn Condenser was filled with silica gel particles (Davidson Chem. Co., No. Mil-D-3716). The condenser jacket was heated with steam. The paraffin was initially heated to just above its melting point and then passed through the column. The column was used to pass 1200 ml. of paraffin. The first and last 300-ml. portions were discarded. The remaining paraffin was triply wrapped in aluminum foil (dull - side in) in 100-ml. portions.

Small pieces of the purified paraffin were dropped on pure water surfaces sprinkled with ignited talc. No spreading was observed.

GLYCEROL

Matheson (99.5% by assay) glycerol was used as the starting material. This material was doubly distilled under vacuum. The distillation setup included a

Liebig condenser, a Viggero column, a 3-neck one liter flask and heating mantle. A vacuum pump protected by a dry ice-acetone trap was used to obtain the reduced pressure. A nitrogen bleed was introduced in the bottom of the flask to promote uniform boiling. A safety shield was placed around the distillation setup.

The first distillation was done at 170°C. under 28.7 inches of vacuum. The middle 70% of one liter of glycerol was collected. This material was redistilled at 172°C. under 28.5 inches of vacuum. The middle 500 ml. were collected and stored in a clean, glass bottle.

IR analysis (Institute IR file No. 3015) indicated this material was quite pure (no detectable oxidation or water). Subsequent analysis of other physical properties of the glycerol indicated it was very pure.

PHYSICAL PROPERTIES OF THE MIXTURES

WEIGHING OUT OF MIXTURES

Mixtures of the pure glycerol and water were weighed out to give mixtures of approximately 40, 60, 75, and 85% glycerol by weight. The weighing was done on a 200-g. double pan swing balance. About 200 ml. of each mixture were obtained. The weight results are shown in Table XXII.

TABLE XXII

WEIGHED GLYCEROL-WATER MIXTURES

~ %	Glycerol, g.	Water, g.	Wt. % Glycerol
40	88.021	132.040	40.00
60	137.990	101.970	57.51
75	178.560	60.500	74.69
85	207.410	36.600	85.00

REFRACTIVE INDEX

The refractive indices of the mixtures were measured using an Abbe Refractometer at 20.0°C. The results were in very good agreement with literature values (41). Table XXIII shows the experimental average refractive indices from this study and the extrapolated composition based on the literature values.

TABLE XXIII

REFRACTIVE INDICES OF THE GLYCEROL-WATER MIXTURES AT 20.0°C.

Av. Refractive Index	Extrapolated Wt. of Glycerol
1.3330	0.00
1.3848	40.50
1.4102	58.13
1.4361	75.51
1.4517	85.55
1.4739	100.00

VISCOSITY

Viscosities of the mixtures were determined at 23.5°C. using a Hoppler falling ball viscometer (Instrument No. CH 1428). These results agreed very well with the literature values (41). The average time of fall, the calculated viscosity, and the extrapolated composition based on the literature values are shown in Table XXIV.

TABLE XXIV

VISCOSITIES OF THE MIXTURES AT 23.5°C.

Av. Fall Time, sec.	Viscosity, cp.	Extrapolated Wt. % Glycerol
12.60 (ball B)	3.6309	40.47
28.85 (ball B)	8.4123	58.16
17.65 (ball C)	30.657	75.20
51.8 (ball C)	89.582	84.97
19.6 (ball D)[a]	1130.000[a]	100.00

[a]Determined at 23.0°C.

COMPOSITION

Comparison of the composition of the glycerol-water mixtures from the weighing up and the values indicated by the refractive indices and viscosities showed very good agreement. The average of these values was used to describe the mixtures. The composition is shown in Table XXV.

TABLE XXV

COMPOSITION OF GLYCEROL-WATER MIXTURES

Approximate Wt. % Glycerol	Actual Composition Wt. % Glycerol
0	0.00
40	40.32
60	57.93
75	75.13
85	85.17
100	100.00

SURFACE TENSION

The surface tensions of the mixtures were measured at 23.5°C. using a DeNouy interfacial tensiometer. The tensiometer was first calibrated against weights. Two runs of 6 measurements per run were made on each mixture. The platinum ring was burned clean between each measurement. Each mixture was put in a clean culture dish every run. The raw data were corrected for the amount of liquid retained on the ring according to recommended procedure (36). The results are shown in Table XXVI. The literature values showed some slight disagreement with one another. The results in this work were in the range of the literature values. It was noted that the results for this work gave slightly lower surface tensions to the higher glycerol content mixtures than the literature values. This difference may be due to the fact that in this study the density changes of the mixtures were included in the correction calculations.

TABLE XXVI

SURFACE TENSION OF THE MIXTURES AT 23.5°C.

Mixture, wt. % glycerol	Av. Tensiometer Reading, dyne $cm.^{-1}$	Corrected Surface Tension, dyne $cm.^{-1}$
Water	77.45	72.85
40.32	73.62	68.80
57.93	72.10	66.76
75.13	70.15	64.66
85.17	68.98	63.36
100.00	67.57[a]	61.70

[a]Measured at 25.0°C.

DENSITY

Density measurements were made on the mixtures after all the filming runs were completed. This was to insure enough material to complete the filming study. The densities were measured with one trial in 100-ml. volumetric flasks at 23.5°C. The larger flasks (as opposed to small pycnometers) were used because of the viscous nature of the higher % glycerol mixtures and the resulting difficulty of filling the flasks. The densities are reported in Table XXVII. The values were slightly lower than literature values (41). However, the mixtures were stored for 6 months. A very slight moisture pickup (< 1%) would account for these differences.

TABLE XXVII

DENSITIES OF THE MIXTURES AT 23.5°C.

Mixture, wt. % glycerol	Density, g. $cm.^{-3}$	Extrapolated Composition, %
40.32	1.0958	39.26
57.93	1.1445	57.21
75.13	1.1926	74.91
85.17	1.2174	84.15

APPENDIX II

APPARATUS

DRIVE CIRCUIT

An electromagnetic coil with a stationary soft iron core was used to drive a steel platform supporting the paraffin surfaces and drops used in this study. The design of this coil was shown in Fig. 1. The frequency of the input into the coil was controlled by a D and H audio-oscillator. The audio-oscillator output was fed into a MacIntosh amplifier. The gain on the amplifier was opened 20%. The drive coil was attached to the highest resistance matched output of the amplifier (6 ohms). The amplitude of the amplifier output was controlled by the audio-oscillator gain control which could regulate 0 to 100% of the amplitude represented by the gain setting on the amplifier. An oscilloscope was used to check the purity of the resulting sine waves in the drive coil. Under the conditions of this study (amplifier gain open 20%), these sine waves were very pure up to about 70 to 75% gain on the audio-oscillator for the range of driving frequencies of 20 to 200 c.p.s. At gains greater than 75%, there were slight irregularities in the peaks of the sine curves. However, the inputs used in oscillating the drops for this study were less than 65%. The driving frequencies of the audio-oscillator were 1/2 the resulting drop frequencies. Therefore, the input to the drops in this study (drop frequencies of 73 to 245 c.p.s.) were purely sinusoidal. The general experimental setup, including the audio-oscillator, amplifier, and drive coil, is shown in Fig. 19. A detailed diagram of the drive coil and R.H. chamber was shown in Fig. 1.

A short circuiting switch was included in the drive circuit. This was used to cut off the input to the drive coil during the damping studies. This circuit made use of a double-throw, double-go, break-before-make toggle switch. In one position, the audio-oscillator and amplifier output was fed into the coil. In the other

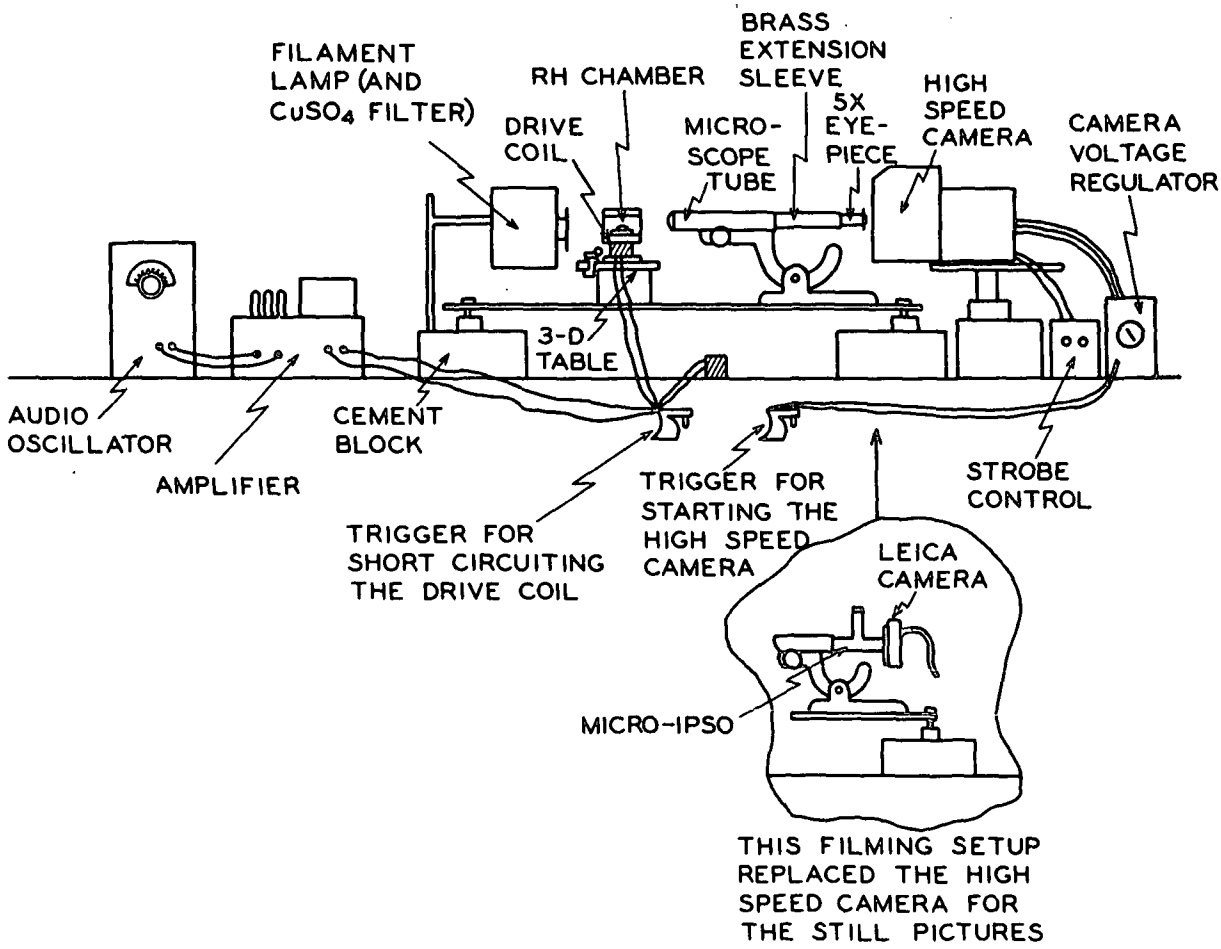

Figure 19. Experimental Drive Circuit and Filming Setups

position, a short circuit was thrown across the coil, and the output from the amplifier was fed through an equivalent resistance. A diagram of this circuit is shown in Fig. 20.

This overall technique of vibrating sessile drops worked extremely well. The vibration of the drops was very sensitive to the frequency of the drive. A slight vibration of a drop was obtained when its natural resonant frequency was being closely approached from either the high or low side. However, the maximum amplitude of vibration could be visually observed in a narrow range of $\sim$ 1.0 to 1.5 c.p.s. Figure 21 shows the amplitude of a water drop at a constant input to the drive coil as the resonant frequency of the drop was approached and passed. The maximum oscillation occurred over a very small range. (The frequencies reported in this figure were the drive frequencies, and the mode of oscillation was the first mode.)

R.H. CONTROL CHAMBER

At less than very high humidities, the small water drops in this study evaporated rapidly. The natural resonant frequency of the first mode of vibration of the drops increased greatly with the decreasing drop volume due to evaporation. Because of the sensitivity of the drop vibration to the drive frequency, the evaporation was easily detected. In addition, if the drops were allowed to vibrate continuously (and the drive frequency was continuously changed as necessary), the evaporation rates were approximately 10 times as rapid as an equilibrium drop under the same conditions. It was necessary to control the R.H. of the atmosphere surrounding the water drops and to reduce the evaporation to a negligible level.

The design of the R.H. control chamber used in this study was shown in Fig. 1.

This R.H. chamber was conditioned by placing 40 strips (1 x 3 $cm.^2$) of Whatman No. 42 filter paper on the floor of the box and then sealing the top. The humidity

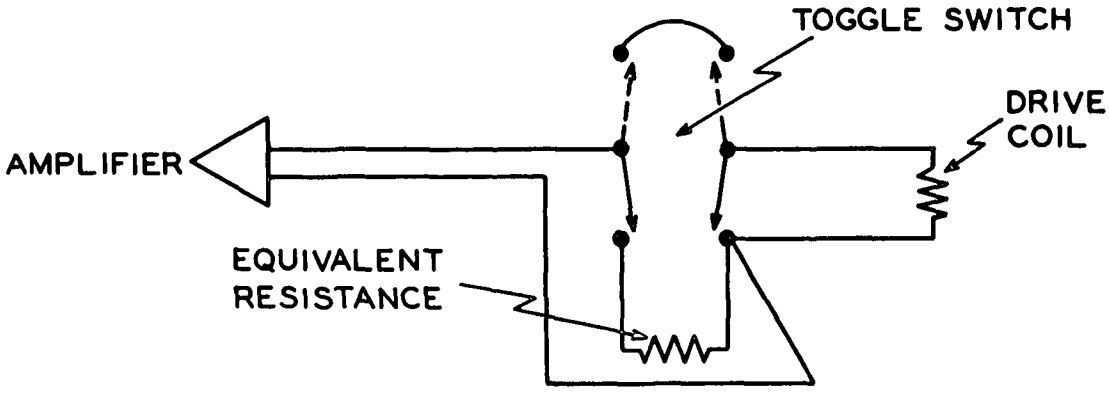

Figure 20. Short Circuit for Damping Films

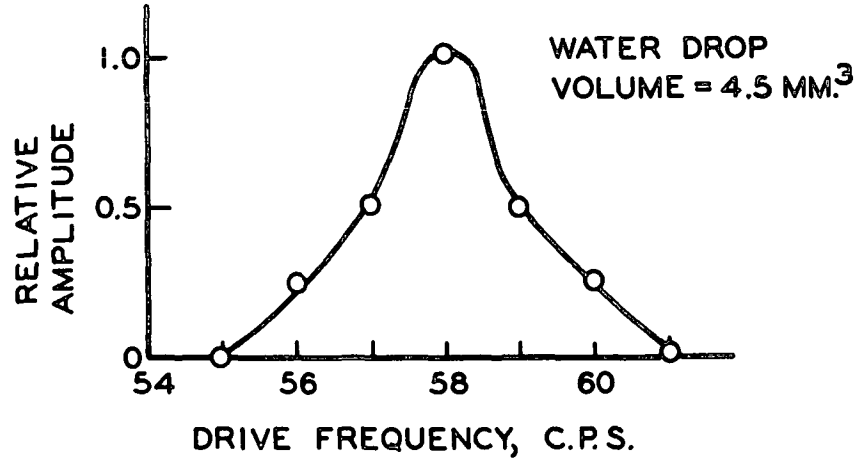

Figure 21. Drop Reaction Near the Resonant Frequency

curve for this box was obtained with a small hygrometer electrode. The electrode was calibrated over saturated salt solutions for very high relative humidities (92.8 to 99.3% R.H. range). The electrode was sealed in the R.H. chamber with the wet paper strips. Leads from the electrode were run from the small hole in the box top (hole through which test drops could be introduced). The R.H. was then measured vs. time. The R.H. curve for the chamber is shown in Fig. 22. The R.H. climbed to 90.0% rapidly (10 min.). A R.H. of 98.5% was reached in 2 hours. Saturation was reached in 4 hours (i.e., the walls of the box became cloudy). It was decided to condition the chamber for 3-1/2 hours before each filming run, at which time the R.H. was 99+%. Removal of the plug from the top of the chamber (which was necessary to introduce test drops) did not measurably affect the humidity for short periods of time. A further precaution was taken against evaporation of the test drop. When the wet filter paper was placed in the chamber, 100 small drops ($\sim$ the size of the test drop) were placed on paraffin surfaces at the sides of the chamber interior.

Figure 23 shows the rate of evaporation of a small water drop at 50% R.H. and the rate at 99+% with the retarding drops in the system. The volume decrease was measured by the increase in drive frequency necessary to excite the first mode of vibration. At 50% R.H., a water drop of $\sim$ 4.5 mm.^{3} evaporated to a volume of $\sim$ 1.5 mm.^{3} in 8 min. A water drop placed in the R.H. chamber after conditioning 3-1/2 hours with wet filter paper and retarding drops (99+% R.H.) evaporated from $\sim$ 3.2 mm.^{3} to $\sim$ 3.0 mm.^{3} in 1 hour. Since the filming times in this study were short (< 1.0 sec.), the conditioning of the R.H. chamber reduced the effect of drop evaporation to a negligible amount.

FILMING SYSTEMS

The general experimental setup used in this study was shown in Fig. 19. Two types of filming systems were used in this arrangement. The equilibrium pictures

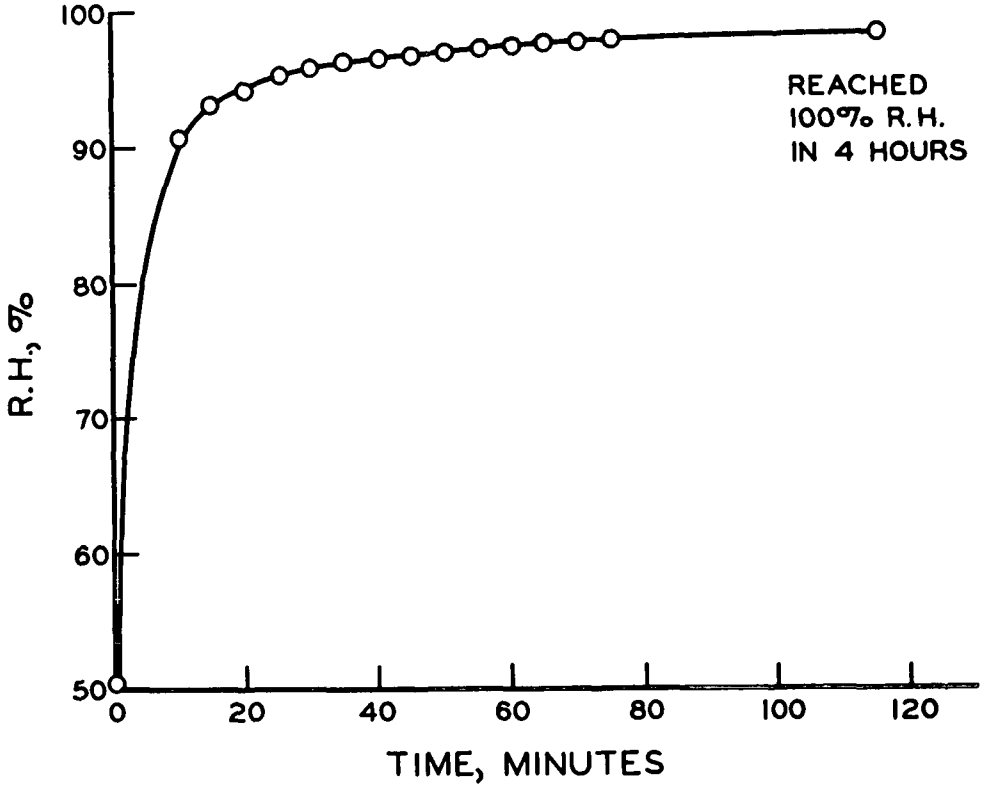

Figure 22. R.H. Versus Time for Conditioning the R.H. Chamber

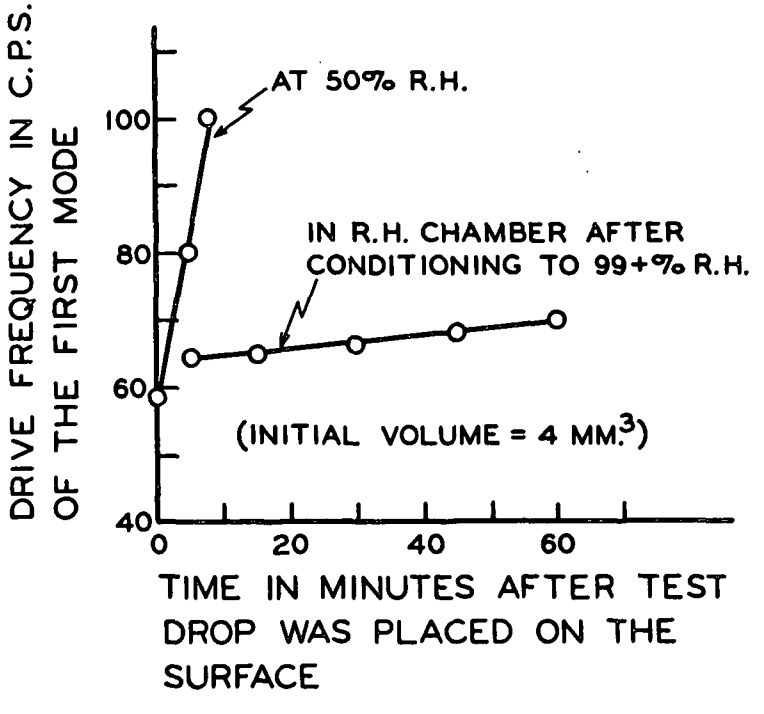

Figure 23. Evaporation of Sessile Water Drops Under 50 and 99+% R.H. Conditions

were taken with a micro-ipso placed in the tube of a microscope with a 48-mm. objective lens. The micro-ipso had a 10X eyepiece. Attached to the micro-ipso were a frosted glass screen and a D.R.P. Leica camera. These were readily positioned at the back of the micro-ipso. The drop image was focused on the screen. The camera was then moved into position and the drop image photographed.

For the oscillating drop films, a Fairchild Motion Analysis Camera, model HS 101, was used. In this case, the optical system consisted of the 48-mm. microscope objective lens and a 5X eyepiece placed in the end of a machined brass extension tube which fit into the microscope barrel. A very fine spider-web crosshair was positioned in the extension tube in the inside focal plane of the optics.

The lighting for the speed and still filming was back lighting of the object by a powerful filament lamp. In both cases, the optics were fixed and unchanged from run to run. The object itself was on a table which could be moved in 3 dimensions. The object was positioned and focused by moving it into the focal plane of the optical system. The dimensions of the optical system used in the high-speed filming are shown in Fig. 24.

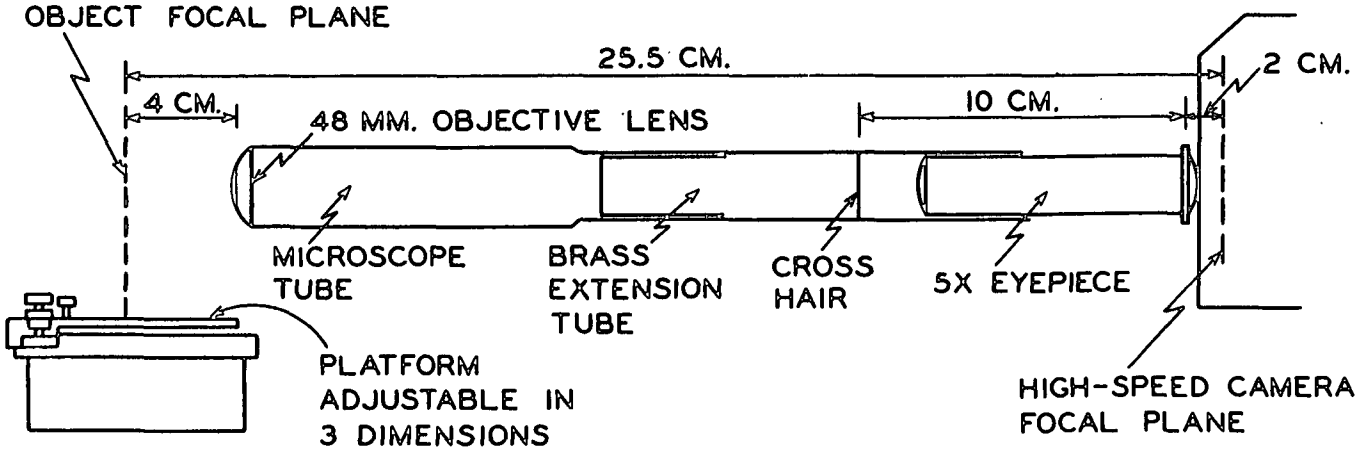

Figure 24. Dimensions of the Fixed Optical System Used for the High-Speed Filming

APPENDIX III

PROCEDURES

PARAFFIN SURFACE PREPARATION

The smooth paraffin surfaces were molded against clean ferrotype plates in small machined brass molds. The molds were milled from one piece of brass. They had a very precise level top and bottom. Since they were a solid piece of metal, they did not produce extraneous vibration in the oscillating system, and they did not change with the mild heating during the surface molding process. The design of these molds is shown in Fig. 25.

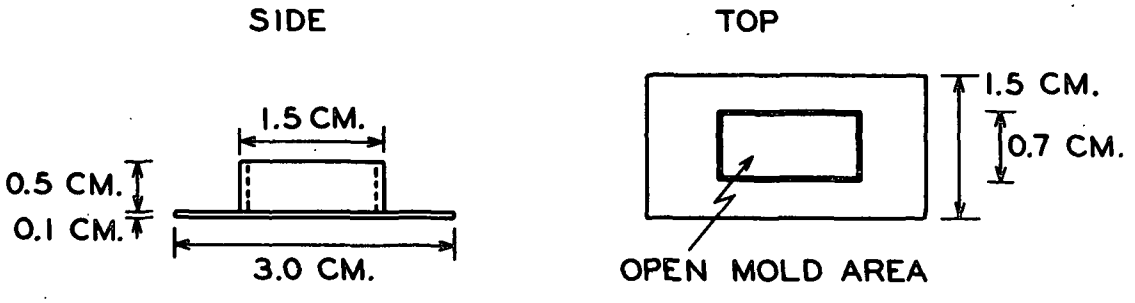

Figure 25. Design of Machined Brass Molds

The procedure for molding the paraffin surfaces was as follows:

1. A ferrotype plate was cleaned by
   a. washing in soap and water, rinsing, and drying,
   b. dipping in cleaning solution,
   c. rinsing with distilled water and drying,
   d. rinsing with toluene and drying,
   e. rinsing thoroughly with triply distilled water, drying in a clean oven, and then cooling.

2. The purified paraffin was melted very slowly in a clean crucible on a hot plate very slightly above the melting point temperature of the paraffin.

3. A brass mold was placed on the ferrotype plate upside down. (The smooth paraffin surface was formed at the interface between the paraffin and ferrotype plate. When the mold was broken loose, the smooth surface was at the top of the mold.)

4. A clean (as all glassware), heated eyedropper was used to remove a small amount of paraffin from the interior of the molten liquid in the crucible. The brass mold was filled with the molten paraffin.

5. The ferrotype plate and mold were placed on the hot plate slightly above the paraffin m.p. temperature. The mold, ferrotype plate, and paraffin were allowed to come to the paraffin m.p. temperature. All air bubbles were allowed to rise away from the paraffin-ferrotype plate interface.

6. The mold and plate were set aside and allowed to cool slowly at room temperature (15+ min.).

7. The mold and plate were then placed in the controlled temperature at which the surface was to be used. When this temperature was reached, the mold was broken away from the ferrotype plate. The resulting paraffin surface was ready for immediate use.

This procedure consistently produced mirror-smooth paraffin surfaces. It was necessary, however, to produce a number of surfaces at one time to insure having a smooth paraffin surface when a filming trial was ready to begin. All surfaces were used within $\sim$ several hours after the paraffin had been placed in the mold.

FILMING CONDITIONS

The filming procedures were presented in the experimental procedures section. For the still pictures taken, the back lighting filament lamp was turned to its medium intensity brightness. Kodak Plus-X pan film was used in the Leica camera. Very satisfactory pictures were obtained at a shutter speed of 1/50 second.

The high-speed films were taken with the back lighting lamp on high intensity. The camera control was run at 40 volts. This resulted in an average film speed of $\sim$ 5000 frames per second. The strobe light fixed inside the camera which marked time intervals on the side of the film was set to mark the film at 1/1000 second intervals. The cycle of this flash was checked with an oscilloscope and standard source. It was found to be accurate within 0.1%. The high-speed films taken in this system under these conditions were extremely good.

CONTACT ANGLE TANGENTOMETER

An accurate and rapid contact angle measuring device was designed for use in this study. The device consisted of a flat lucite ring with 6 in. and 5 in. outside and inside diameters, respectively. A protractor was mounted on the top of this flat ring with the origin of the protractor coinciding with the center of the ring. A semicircular solid piece of lucite sat inside the ring with a machined fit. A surface mirror was mounted on this movable disk. The mirror was perpendicular to the ring and extended to the bottom of the ring. It coincided with the base line of the protractor and was scribed with a vertical line coinciding with the origin of the protractor. A pointer was attached to the back of the mirror. It was perpendicular to the mirror in the plane of the ring and passed through the origin of the protractor. The design of this instrument is shown in Fig. 26.

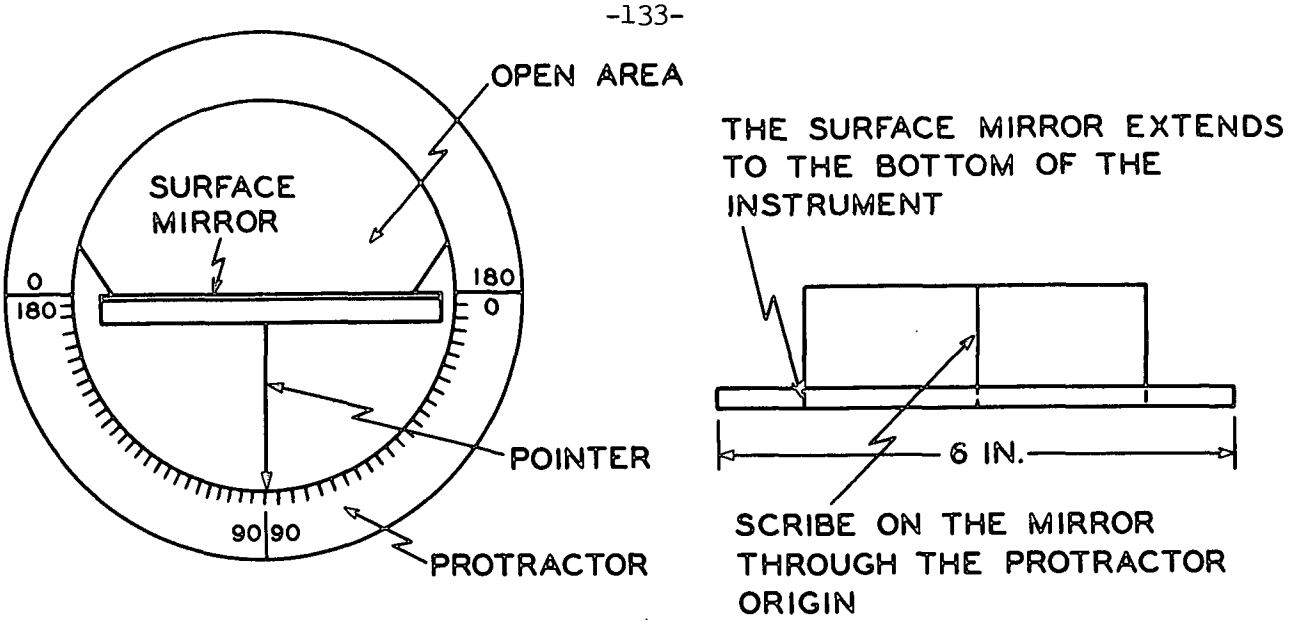

Figure 26. Design of the Tangentometer

The contact angle of a drop image was measured by setting the pointer on 90°. The origin of the protractor was placed at the contact point with the bottom of the mirror on the base line of the drop. The mirror and disk inside the ring were rotated until the curve of the drop shape and its reflected image in the mirror formed a continuous curve. The contact angle was then indicated on the protractor by the pointer attached to the mirror.

HIGH-SPEED FILM MEASUREMENTS

The high-speed films of drop oscillation were measured in the following manner:

1. An oscillation film was viewed on a microfilm reader. A portion near the end of the film was selected for measurement. At this point, the camera had been up to speed, and the resulting time separation between frames was constant. The contact angles for a sequence of frames covering 4 periods of drop oscillation were measured with the tangentometer. These frames were then marked.

2. The marked section of film was cut into strips of about 20 frames each. The sequence was preserved by the way the film was cut, and

each section was scribed with a sequence number. The film strips were mounted on glass plates for measurement on the microcomparator.

3. The drop images were measured on the microcomparator. Twenty relative coordinate points were taken around one half of the drop image. The points were taken in the order shown in Fig. 27. The first point taken was the drop edge where it contacts the surface. The second was the origin (found by taking one half the distance between the edges). The third point was the very top of the drop. The remaining 17 points were taken counterclockwise from the top to the edge.

4. Each point was established by turning the X-screw on the microcomparator clockwise and the Y-screw counterclockwise. The X, Y coordinates were punched on IBM cards with four points to a card. Every five cards in the resulting deck were a set of 20 relative points describing the drop shape at a particular time.

5. The time function was easily determined by measuring the distance between the 1/1000 second markings on the film and dividing by the length of a frame.

6. The absolute units conversion was obtained by measuring films of a 0.1, 0.01-mm. stage micrometer.

7. The measured film strips were stored in marked envelopes.

The high-speed films of drop damping were measured in a similar manner. However, the microcomparator measurements were made only on the frames representing the maximum amplitude as the oscillation damped out. Figure 27 shows how the films were sectioned and marked, and the order in which the data points were taken about the drop image.

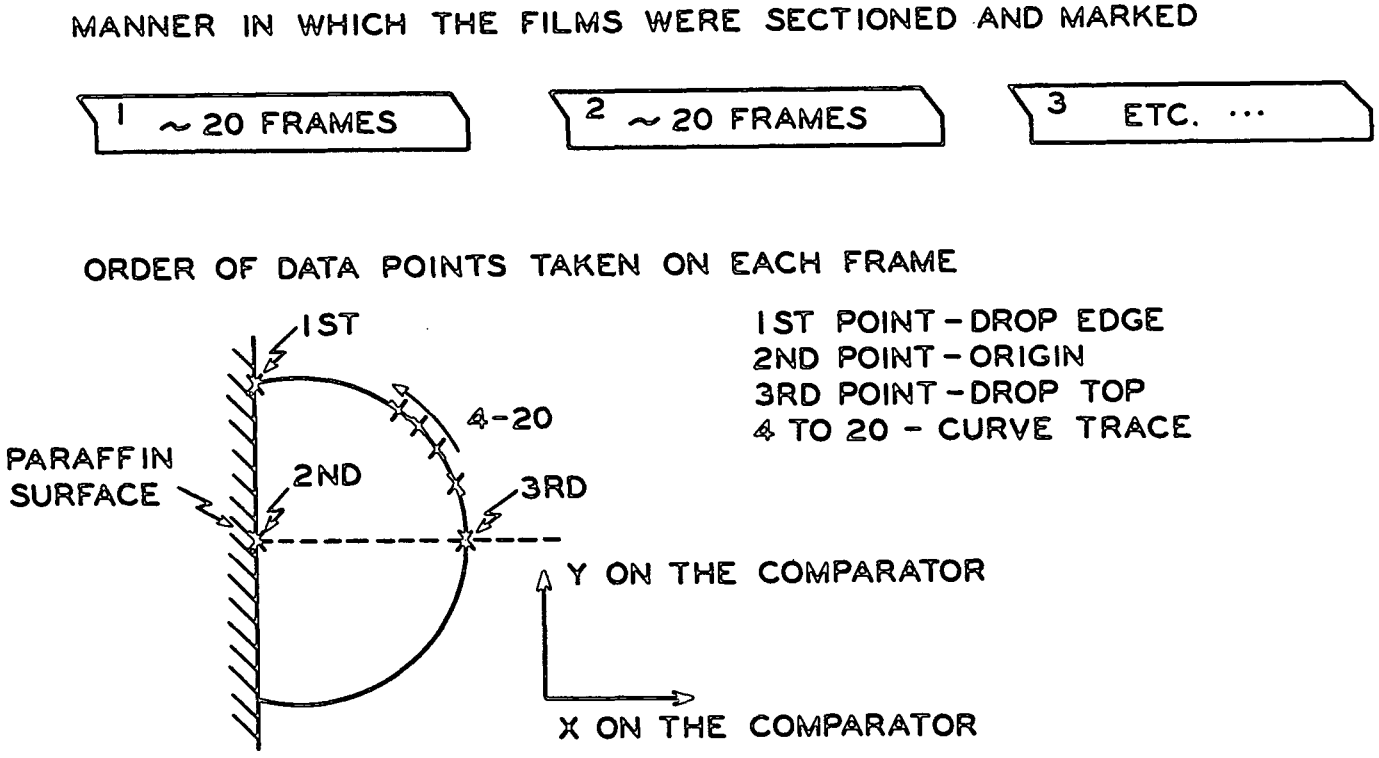

Figure 27. Film Sectioning and Microcomparator Data Taking

APPENDIX IV

EXPERIMENTAL DATA

EQUILIBRIUM CONTACT ANGLES

The equilibrium contact angles were measured on enlarged negatives of the still pictures that were taken in this study. A light source was placed behind a glass plate. The enlarged negatives were placed on this plate, and the contact angles were measured with the tangentometer. All the equilibrium results were for drops of the various mixtures on paraffin surfaces that had been conditioned for 3-1/2 hours in the R.H. chamber at 23.5°C. The results of the average contact angles per picture for the mixtures are shown in Table XXVIII.

TABLE XXVIII

EQUILIBRIUM CONTACT ANGLES OF THE MIXTURES ON CONDITIONED PARAFFIN SURFACES AT 23.5°C.

Mixture	Equilibrium Contact Angles (each value is an average for an individual drop), °
Water	107.0, 106.0, 106.5, 106.0 106.0, 106.5
40.32 Wt. % glycerol	101.0, 100.0, 100.0, 100.0 100.0, 100.5, 101.0
57.93 Wt. % glycerol	98.0, 97.0, 96.5, 97.0, 96.5 97.0, 97.0, 97.0, 97.5, 97.0 96.0, 96.0, 96.5
75.13 Wt. % glycerol	94.5, 94.5, 94.5, 94.5, 94.5 94.5, 94.0, 94.5, 94.5, 94.5, 94.0
85.17 Wt. % glycerol	93.0, 93.0, 93.0, 93.0, 93.5 93.0, 93.0, 93.0, 93.0
100.00 wt. % glycerol	91.0, 91.5, 91.5, 91.0, 90.5, 91.0

The average values of the cosine of the equilibrium contact angles versus % weight glycerol were plotted in Fig. 8.

DYNAMIC CONTACT ANGLES

The dynamic contact angles were measured with the tangentometer on steady-state oscillation films viewed on a microfilm viewer. These data were obtained for 4 periods of oscillation for each drop. The contact angle changes were found to be sinusoidal in all cases. The dynamic contact angle data are shown in Table XXIX. The cosines of the average median dynamic contact angles for each mixture were plotted versus % weight glycerol in Fig. 8.

TABLE XXIX

DYNAMIC CONTACT ANGLE DATA

C The dynamic contact angles were measured with the tangentometer
C device. The contact angle data are listed here in sequence
C from left to right. The time increment between each datum is
C constant within a given film. These data were obtained from
C the same frames that were measured on the microcomparator.

Film 17

106.0	103.0	100.0	98.0	97.0	95.0	95.0	96.0	98.0	100.0	103.0
106.0	108.5	111.0	113.0	114.0	115.0	114.0	112.5	111.0	107.0	103.0
101.0	98.0	97.0	95.0	94.0	95.0	97.0	98.0	101.0	104.0	107.0
110.0	112.0	113.0	115.0	115.0	113.0	112.0	110.0	107.0	104.0	101.0
99.0	97.0	95.0	94.0	95.0	97.0	98.0	101.0	104.0	107.0	110.0
112.0	113.0	115.0	115.0	113.0	110.0	108.0	106.0	103.0	100.0	98.0
97.0	95.0	95.0	96.0	98.0	100.0	103.0	106.0	110.0	112.0	113.0
115.0	115.0	113.0	112.0	110.0	107.0	104.0	101.0	98.0		

Film 34

106.0	99.0	96.0	94.0	93.0	93.0	92.0	95.0	98.0	105.0	111.5
116.0	116.0	115.0	106.0	100.0	97.0	93.0	91.0	91.0	92.0	93.0
96.0	103.0	110.0	116.0	119.0	118.0	115.0	113.0	107.0	99.0	95.0
92.5	92.0	92.5	95.0	101.0	106.0	110.0	114.0	117.5	119.0	117.0
113.0	108.0	102.0	99.0	95.0	94.0	92.0	93.0	96.0	101.0	106.0
112.0	115.0	118.0	118.0	116.0	113.0	107.0	102.0			

Film 18

118.0	115.0	111.0	107.0	100.0	95.0	92.0	90.0	90.0	91.0	92.0
96.0	102.0	108.0	113.0	118.0	119.0	118.0	116.0	112.0	106.0	100.0
95.0	92.0	90.0	91.0	92.0	94.0	99.0	106.0	112.0	117.0	119.0
118.0	115.0	110.0	102.0	96.0	92.0	91.0	90.0	90.0	92.0	95.0
100.0	107.0	111.5	115.0	117.0	119.0	117.0	112.0	107.0	99.0	94.0
92.0	91.0	90.0	92.0	95.0	100.0	106.0	111.5	116.0	118.0	119.0
118.0	113.0	108.0								

Film 33

111.0	113.0	116.0	117.0	117.0	116.0	116.0	113.0	108.0	104.0	100.0
97.0	94.5	94.5	96.0	97.0	98.0	100.0	104.0	105.0	109.0	114.0
115.0	116.0	117.0	116.0	114.0	112.0	109.0	105.0	101.0	99.0	97.0
95.0	94.5	94.5	95.0	96.0	98.0	100.0	104.0	108.5	112.5	114.0
116.0	117.0	117.0	116.0	115.0	112.0	106.0	101.0	97.0	95.0	94.5
95.0	97.0	98.0	100.0	104.0	107.0	111.0	114.0	116.0	116.0	117.0
115.0	113.0	111.0	107.0	102.5	100.0	98.0	96.5	94.5	94.5	95.0
96.0	96.0	99.0	102.5	105.0	108.0	113.0	116.0			

TABLE XXIX (Continued)

DYNAMIC CONTACT ANGLE DATA

Film 20

107.0	103.5	100.0	98.0	96.0	92.0	93.0	96.0	100.0	107.0	113.0
117.0	119.0	120.0	122.0	120.0	117.0	114.5	108.0	104.0	101.0	98.0
94.0	93.0	92.0	93.0	96.0	100.0	105.0	110.0	115.0	118.0	120.0
122.0	120.0	118.0	115.0	111.0	105.0	100.0	96.0	93.0	92.0	93.0
94.0	98.0	101.0	104.0	108.0	114.0	117.0	120.0	122.0	120.0	118.0
116.0	112.0	107.0	100.0	97.0	94.0	92.0	93.0	96.0	100.0	105.0
110.0	115.0	118.0	120.0	122.0	120.0	117.0	114.0	110.0	105.0	100.0
96.0	93.0	92.0								

Film 21

101.0	106.0	110.0	115.0	118.0	122.0	119.0	118.0	115.0	112.0	109.0
105.0	101.0	98.0	95.0	93.0	93.0	92.0	93.0	95.0	98.0	102.0
108.0	112.0	116.0	118.0	120.0	122.0	121.0	118.0	115.0	112.0	107.0
104.0	101.0	98.0	95.0	93.0	91.0	91.0	93.0	96.0	100.0	105.0
110.0	115.0	118.0	120.0	121.0	119.0	117.0	115.0	112.0	109.0	105.0
101.0	98.0	95.0	93.0	92.0	93.0	95.0	98.0	102.0	104.0	107.0
112.0	115.0	118.0	121.0	121.0	119.0	118.0	116.0	112.0	108.0	102.0
98.0	95.0	93.0	91.0	91.0	93.0	95.0	98.0	102.0	108.0	112.0
115.0										

Film 36

110.0	105.5	100.0	96.5	94.0	92.0	91.0	91.0	92.0	94.5	98.0
102.0	106.0	113.0	117.0	119.5	120.0	121.0	120.0	119.0	115.0	111.0
105.0	101.0	97.0	94.5	93.0	92.0	91.0	91.0	92.0	94.5	99.0
103.5	109.0	115.0	118.0	119.0	120.0	121.0	120.0	118.0	115.0	110.0
106.0	99.0	97.0	94.0	92.0	91.0	90.0	91.0	92.0	94.0	98.0
102.5	109.5	114.5	117.0	119.0	120.0	121.0	120.0	119.0	117.0	114.5
105.0	99.0	96.0	94.0	92.0	91.0	90.5	90.5	91.0	93.5	96.0
101.0	108.0	112.0	116.0	118.0	119.0	120.0	120.0	119.0	116.0	112.0
104.0										

Film 73

108.0	102.0	99.0	97.0	95.0	95.0	94.0	95.0	98.0	105.0	109.0
113.0	115.0	116.0	116.0	115.0	114.0	113.0	108.0	105.0	102.0	99.0
96.0	95.0	94.0	96.0	98.5	101.0	107.0	111.0	114.0	115.5	116.0
116.5	115.0	115.0	113.0	107.0	102.0	100.0	97.0	95.0	95.0	94.5
96.0	99.0	102.5	107.0	111.5	114.0	115.0	116.0	115.0	114.0	112.0
109.0	105.0	101.0	98.0	97.0	95.0	94.0	95.0	96.0	98.0	102.0
107.0	111.0									

TABLE XXIX (Continued)

DYNAMIC CONTACT ANGLE DATA

Film 41

101.0	98.0	95.0	92.0	90.0	89.0	92.0	96.0	100.0	105.0	108.0
110.0	111.0	108.0	104.0	100.0	96.0	93.0	91.0	90.0	91.0	95.0
100.0	104.0	108.0	111.0	111.0	109.0	106.0	100.0	96.0	93.0	90.0
89.0	89.0	92.0	95.0	102.0	107.0	109.0	110.0	111.0	108.0	103.0
97.0	94.0	91.0	89.0	89.0	92.0	97.0	102.0	108.0	110.0	111.0
111.0	110.0	105.0	99.0	95.0						

Film 45

105.0	101.0	98.0	96.0	93.0	91.0	91.0	93.0	97.0	101.0	106.0
109.0	111.0	113.0	113.0	113.0	109.0	105.0	101.0	99.0	96.0	94.0
92.0	91.0	93.0	93.0	96.0	98.0	103.0	106.0	109.0	111.0	112.0
113.0	113.0	111.0	108.0	104.0	100.0	96.0	94.0	93.0	92.0	91.0
93.0	95.0	98.0	102.0	106.0	109.0	111.0	113.0	113.0	112.0	108.0
105.0	102.0	99.0	96.0	94.0	92.0	91.0	91.5	92.0	95.0	98.0
102.0	106.0	109.0	111.0	113.0	113.0	111.0	110.0	108.0	104.0	99.0

Film 43

99.0	97.0	94.0	93.0	92.0	94.0	95.0	98.0	102.0	106.0	107.5
108.5	109.0	109.0	108.0	106.0	103.0	99.0	97.0	95.0	93.0	92.0
92.0	94.0	97.5	100.0	103.0	105.0	107.0	109.0	110.0	110.0	108.5
107.5	105.0	103.0	100.0	97.5	95.0	93.0	92.0	92.0	93.0	95.0
97.0	101.0	104.0	106.0	108.0	109.0	110.0	110.0	108.0	106.0	102.0
98.0	96.0	94.0	92.0	92.0	94.0	96.0	98.0	102.0	106.0	108.0
109.5	110.0	110.0	109.0	108.0	105.5	101.5	97.0			

Film 56

95.0	92.0	89.0	86.0	86.0	87.0	89.0	92.0	95.0	99.0	102.0
105.0	106.0	107.0	107.0	105.0	101.0	96.0	93.0	90.0	87.0	85.0
86.0	88.0	90.0	93.0	97.0	101.0	104.0	106.0	107.0	105.0	102.0
98.0	94.0	91.0	88.0	86.0	85.0	87.0	89.0	91.0	93.0	96.0
101.0	104.5	106.0	107.0	106.0	104.0	102.0	98.0	94.0	91.0	88.0
86.0	85.0	86.0	88.0	90.0	93.0	97.0	101.0	104.0	105.0	107.0
106.0	104.0	101.0	97.0	93.0						

Film 61

95.0	92.0	90.0	88.0	87.0	86.0	88.0	91.0	95.0	99.0	102.0
104.0	106.0	107.0	106.0	104.0	101.0	97.0	93.0	90.0	88.8	86.5
86.0	87.5	90.0	92.0	96.0	99.0	102.0	104.0	105.0	106.0	107.0
105.0	102.0	99.0	95.0	92.0	90.0	89.0	87.0	86.0	86.0	89.0
92.0	96.0	99.0	103.0	105.0	106.0	107.0	106.0	104.0	101.0	97.0
93.0	90.0	88.0	86.0	86.0	87.0	88.0	91.0	95.0	99.0	102.0
104.0	105.0	106.0	107.0	105.0	102.0	98.0	94.0			

TABLE XXIX (Continued)

DYNAMIC CONTACT ANGLE DATA

Film 54

98.0	94.0	91.0	89.0	88.0	89.0	92.0	94.0	97.0	100.0	103.0
105.0	106.0	107.0	106.0	104.0	101.0	98.0	95.0	92.0	89.0	87.0
88.0	89.0	91.0	93.0	96.0	100.0	103.0	105.0	106.0	107.0	105.0
103.0	100.0	97.0	95.0	93.0	91.0	89.0	88.0	87.0	88.0	90.0
92.0	95.0	98.0	101.0	104.0	106.0	107.0	106.0	105.0	102.0	99.0
96.0	93.0	91.0	89.0	88.0	87.0	88.0	91.0	94.0	97.0	100.0
103.0	105.0	106.0	107.0	106.0	105.0	102.0	99.0	96.0		

Film 53

95.0	89.0	86.0	85.0	87.0	95.0	102.0	106.0	107.0	106.0	102.0
96.0	89.0	86.0	85.0	87.0	90.0	97.0	103.0	106.0	106.0	104.0
98.0	92.0	88.0	85.0	86.0	91.0	97.0	102.0	106.0	107.0	105.0
101.0	93.0	89.0	86.0	85.0	88.0	94.0	100.0	105.0	107.0	106.5
102.0	97.0	91.0								

Film 63

100.0	94.0	91.0	88.0	86.0	85.0	87.0	90.0	95.0	100.0	103.0
106.0	107.0	108.0	106.0	102.0	95.0	90.0	87.0	85.0	85.5	87.5
90.5	96.0	101.0	104.0	106.0	107.0	108.0	105.0	101.0	94.0	90.0
88.0	86.0	85.0	88.0	91.0	97.0	102.0	105.0	107.0	108.0	106.0
104.0	100.0	95.0	91.0	88.0	86.0	85.0	87.0	89.0	94.0	100.0
104.0	106.0	108.0	107.0	106.0	103.0	97.0	92.0			

Film 65

96.0	93.0	91.0	89.0	88.0	87.0	88.0	90.0	94.0	99.0	102.0
105.0	106.0	105.5	105.0	103.0	100.0	96.0	93.0	90.0	88.0	87.0
86.0	88.0	90.0	93.0	97.0	100.0	103.0	105.0	106.0	106.0	105.0
102.0	98.5	94.5	91.0	89.0	87.0	86.0	87.0	89.0	91.5	95.0
99.0	102.0	104.0	105.5	106.0	105.0	103.0	100.0	96.0	92.0	90.0
88.0	87.0	86.0	87.0	89.0	92.0	95.0	100.0	103.0	105.0	106.0
105.5	105.0	102.0	99.0	95.0						

Film 82

101.0	98.0	92.0	88.0	86.0	87.0	90.0	96.0	100.0	104.0	105.5
105.0	101.0	95.0	92.0	88.0	86.0	87.0	91.0	96.0	101.0	104.0
105.5	103.0	99.5	93.5	90.0	87.5	86.0	87.0	91.5	97.0	100.0
103.5	105.5	101.0	96.5	92.0	87.5	86.0	87.0	89.0	91.0	99.0
103.0	105.5	105.0	102.0	97.0	92.0					

TABLE XXIX (Continued)

DYNAMIC CONTACT ANGLE DATA

Film 77

95.0	91.0	88.0	86.0	87.0	91.0	96.5	102.0	106.0	106.0	102.0
96.0	91.0	88.0	85.5	88.0	91.5	97.0	102.0	106.0	106.0	102.0
95.0	91.0	87.0	85.0	86.5	92.0	98.0	102.0	106.0	106.0	102.0
96.0	91.0	87.0	85.0	89.0	93.0	98.0	103.0	106.0	104.0	99.0
92.5										

Film 50

100.0	97.0	95.0	93.0	91.0	90.0	91.0	92.0	93.0	94.0	96.0
98.0	101.0	103.0	104.0	105.5	105.5	107.0	106.0	105.0	104.0	
103.0	101.0	97.0	95.0	93.0	92.0	91.0	90.0	89.0	88.5	90.0
92.0	94.0	97.0	100.0	102.0	103.0	104.0	105.0	105.0	105.5	105.0
104.0	102.0	100.0	97.0	95.0	93.0	91.0	90.0	89.0	89.0	90.5
92.5	94.0	95.0	98.0	101.0	103.0	104.0	105.0	105.5	105.5	105.0
104.0	103.0	102.0	100.0	97.0	95.0	93.0	91.5	90.0	89.0	89.0
90.0	91.0	92.0	93.0	95.0	97.5	100.5	102.0	103.0	104.0	105.0
105.5	105.5	105.0	104.0	103.0	101.0					

Film 78

96.0	92.0	89.0	87.0	87.0	89.0	93.0	97.0	102.0	105.0	106.0
105.0	102.0	100.0	96.0	92.0	89.0	87.0	86.0	89.0	93.0	97.0
101.0	105.0	105.0	102.0	99.0	95.0					

Film 80

96.0	91.0	88.0	87.0	87.0	89.0	92.0	97.0	100.0	103.0	103.0
101.0	99.0	94.0	91.0	89.0	87.0	87.0	89.0	92.0	97.0	100.0
102.0	103.0	101.0	98.0	93.0						

Film 66

100.0	96.0	93.0	91.0	89.0	87.0	86.0	86.0	87.0	90.0	93.0
97.0	100.0	102.0	103.0	102.0	98.0	94.0	91.0	88.0	86.0	86.0
87.0	89.0	91.0	94.0	98.0	101.0	102.0	102.0	101.0	97.0	94.0
91.0	89.0	88.0	86.0	86.0	88.0	91.0	94.0	98.0	100.0	102.0
103.0	102.0	99.0	95.0	92.0	89.0	87.0	86.0	86.0	88.0	91.0
95.0	99.0	101.0	102.0	103.0	102.0	99.0	95.0	92.0		

TABLE XXIX (Continued)

DYNAMIC CONTACT ANGLE DATA

Film 58

99.0	95.0	92.0	90.0	88.0	88.0	90.0	92.0	95.0	99.0	102.0
104.0	105.0	104.0	103.0	100.0	96.0	93.0	91.0	88.0	87.0	89.0
91.0	93.0	96.0	100.0	103.0	105.0	105.0	104.0	103.0	101.0	97.0
94.0	91.0	89.0	88.0	88.0	89.0	92.0	95.0	98.0	102.0	103.0
104.0	105.0	104.0	102.0	98.0	94.0	92.0	90.0	88.0	87.0	88.0
90.0	93.0	97.0	101.0	103.0	105.0	105.0	104.0	101.0		

Film 81

92.0	90.0	89.0	90.0	91.0	94.0	97.0	100.0	102.0	101.0	99.0
95.0	92.0	90.0	89.0	89.0	90.0	93.0	98.0	100.0	101.0	102.0
101.0	98.0	95.0	92.0	90.0	89.0	89.0	90.0	92.0	95.0	98.0
100.5	102.0	101.0	100.0	97.0	93.0	91.0	89.0	89.0	90.0	93.0
97.0	100.0	101.0	102.0	101.0	98.5	96.0	92.0			

Film 79

100.0	96.0	92.0	90.0	88.0	89.0	91.0	96.0	99.0	101.0	102.0
102.0	101.0	100.0	97.0	93.0	90.0	88.0	90.0	93.0	98.0	100.0
102.0	103.0	102.0	100.0	97.0	94.0	91.5	88.0	89.0	93.0	98.0
101.0	102.0	102.0	100.0	98.0	95.0	92.0	90.0	88.0	91.0	94.0
97.0	100.0	102.0	102.0	100.0	98.0	95.0	93.0			

DATA FOR TANGENTOMETER ERROR ESTIMATE

Measurements were made on geometrically constructed contact angles with the tangentometer. These data were used to estimate the probable error in the contact angle measurements. These data are shown in Table XXX.

TABLE XXX

TANGENTOMETER ERROR ESTIMATE DATA
ON CONSTRUCTED CONTACT ANGLES

Angle (degrees) measured by construction	62.4	70.3	81.2	101.2	110.5	120.8
Tangentometer measurements (degrees)	62.5	70.9	81.4	101.2	110.5	121.1
	62.2	70.8	81.3	101.2	110.7	121.0
	62.4	70.9	81.3	101.5	110.6	120.8
	62.4	70.6	81.2	101.2	110.8	120.9
	62.4	70.6	81.5	101.4	110.7	121.0
	62.3	70.8	81.1	101.2	110.5	120.7
	62.5	70.6	81.5	101.3	110.5	120.7
	62.2	70.6	81.5	101.1	110.8	120.7
	62.5	70.7	81.5	101.5	110.9	120.8
	62.3	70.7	81.2	101.5	110.5	121.0
Median contact angle	62.37	70.73	81.35	101.31	110.65	120.87
Standard deviation	± 0.14	± 0.15	± 0.25	± 0.23	± 0.23	± 0.22

Overall standard deviation = ± 0.19

REFERENCE FILM DATA

The data obtained from the microcomparator measurements on the reference high-speed films of the 0.1, 0.01-mm. stage micrometer were used to determine the absolute units of the drop shape microcomparator data. They were also used to make estimates of the probable error in the microcomparator measurements. These results were discussed in the Error Analysis section. These data are shown in Table XXXI.

TABLE XXXI

MICROCOMPARATOR MEASUREMENTS ON THE HIGH-SPEED REFERENCE FILMS

Film Number	Microcomparator (m.c.) Units/mm.	Std. Deviation of the Group
40	888, 889, 892 885, 890, 894	3.30
47	905, 909, 905 906, 905, 902	2.28
60	901, 898, 900 902, 908, 902	2.72
68	896, 902, 896 891, 895, 898	3.60
76	899, 898, 898 899, 896, 896	1.22

Overall median value = 895.7 $\pm$ 6.02 m.c. units/mm.

83[a]	1067, 1064, 1066, 1066, 1063 1073, 1065, 1063, 1072, 1066 1062, 1062, 1064, 1066, 1063 1065, 1062, 1062, 1063	

median = 1064.7 $\pm$ 2.70 m.c. units/mm.

[a]The optics of the filming setup were changed for this reference film.

TIME FUNCTION DATA

The time function was determined by measuring the distance separating the 1/1000-sec. marks on the high-speed films. The frame lengths were measured on all the films with the microcomparator. The time per frame was obtained by dividing the average distance per 1/1000-sec. mark on each film by the average frame length. The average 1/1000-sec. length per film was based on $\sim$ 10 measurements. The averages and deviations for each film are shown in Table XXXII. The average frame lengths were based on $\sim$ 10 measurements per film. These averages and the calculated sec. per frame are also shown in Table XXXII.

TABLE XXXII

AVERAGE 1/1000-SEC. LENGTH (M.C. UNITS), AVERAGE FRAME LENGTH, AND TIME PER FRAME FOR THE OSCILLATION FILMS

Film Number	Av. 1/1000-Sec. Length, m.c. units	Av. Frame Length, m.c. units	Time per Frame, $x10^{-3}$ sec.
17	18154 ± 0.3	3586	0.197
34	17884 ± 1.7	3583	0.199
18	17904 ± 2.8	3584	0.198
33	17422 ± 5.6	3585	0.201
36	19129 ± 3.0	3585	0.183
20	17046 ± 4.5	3587	0.207
21	15504 ± 6.2	3580	0.231
73	19644 ± 5.2	3588	0.179
41	17059 ± 5.0	3596	0.207
45	18081 ± 4.0	3583	0.194
43	18946 ± 4.8	3584	0.189
56	18463 ± 3.8	3589	0.192
61	18447 ± 4.9	3586	0.191
63	18251 ± 4.5	3586	0.193
54	18374 ± 6.8	3583	0.190
53	09920 ±18.4	3586	0.350
65	16397 ± 8.2	3585	0.212
82	20140 ± 4.9	3580	0.178
77	20046 ± 4.3	3577	0.179
79	20173 ± 4.1	3578	0.178
81	20215 ± 4.2	3577	0.177

Overall av. frame length = 3586

DROP SHAPE DATA

The method of obtaining the drop shape data was discussed in Appendix III. The general nature of these data was discussed in the Experimental Results section. The characteristics of these data were shown in Table V and Fig. 4 and 5. The raw data associated with the shape measurements were too voluminous to include in this text. One such set of microcomparator data is shown in Table XXXIII to indicate the nature of these data for all the drops in this study.

TABLE XXXIII

DROP SHAPE DATA FOR FILM NUMBER 17

```
C     MICROCOMPARATOR DATA FOR THE DROP SHAPE OF DROP 17.
C     WATER DROP, VOLUME= 0.885 MM3.
C     EACH TEN DIGIT NUMBER IS A SET OF X,Y CO-ORDINATES. THE FIRST
C     5 DIGITS ARE THE X CO-ORDINATE, AND THE SECOND 5 THE Y.
C     THERE ARE 20 SETS OF POINTS PER FRAME, SO EACH 5 LINES IN
C     THIS LISTING DESCRIBE ONE FRAME. THE SEQUENCE OF POINTS IN
C     EACH FRAME (FROM LEFT TO RIGHT) IS,
C     FIRST POINT = THE DROP EDGE
C     SECOND POINT = THE ORIGIN
C     THIRD POINT = THE DROP TOP
C     NEXT 17 POINTS TRACE THE CURVE FROM THE TOP TO THE EDGE.
C     THE DATA SETS ARE IN SEQUENCE AND REPRESENT EQUAL TIME INCREMENTS.
```

2373816333	2373816922	2448316922	2446216744
2442416659	2439616599	2433816526	2429616481
2427216457	2424416440	2422116424	2419216409
2415916384	2412816370	2409216354	2401816332
2396416321	2391516314	2386516318	2379116325
2732316336	2732316922	2809116922	2807816782
2805616710	2801516628	2796916560	2793016518
2789416487	2786016457	2780816426	2773916380
2770116364	2765216349	2761516343	2757616334
2753916326	2749516323	2741916321	2735516330
3090316332	3090316918	3168816918	3168616834
3166516729	3161216629	3154616544	3148316482
3143816448	3138816419	3133616389	3129116372
3123816352	3118116339	3114816334	3109616326
3104616319	3101016321	3097816322	3094216329
3449516336	3449516920	3530116920	3529216820
3526616736	3523716670	3520116610	3515516554
3510516503	3503716452	3498416419	3492916395
3488216376	3483016360	3477816344	3472916337
3468216332	3463616326	3459416326	3454116330
3808916337	3808916920	3890416920	3889816842
3888316758	3885216687	3880816613	3875316550
3870216503	3865016464	3858716427	3851316390
3845516370	3840516356	3835716341	3831916336
3826716336	3822716329	3818216334	3813916336
4167416338	4167416920	4249216920	4248816838
4246816771	4242916665	4236016581	4229416508
4222816462	4212016399	4201816365	4194416347
4190116342	4185916338	4182316336	4180016332
4177916335	4176016336	4174216333	4170916336
4525016335	4525016918	4606316918	4605916819
4604316764	4600916697	4597416627	4592216567
4587116512	4583316480	4579216453	4574916427
4570516407	4565716388	4559516368	4552316347
4546916336	4541216335	4533916334	4528416337
2404016324	2404016900	2485516900	2485216826
2483916772	2481616698	2477716629	2474216574
2471116538	2465516484	2458616435	2453216401
2446216369	2441316350	2436616338	2431516325
2426116317	2421216313	2415616308	2409416314

TABLE XXXIII(Continued)

DROP SHAPE DATA FOR FILM NUMBER 17

2761816325	2761816904	2842216904	2841616846
2840616777	2837616691	2833316607	2827216533
2820816475	2814216431	2805616376	2799216353
2793616335	2789616327	2784916321	2779516315
2775516314	2772116314	2768416317	2765116319
3119116322	3119116907	3197816907	3197516818
3195916758	3192516671	3189516611	3184516551
3180316501	3174716454	3169316419	3165216395
3159516364	3153116340	3149216328	3144616318
3138416315	3133416308	3127716311	3123016320
3477616326	3477616909	3553216909	3552916829
3551716764	3549116685	3545716629	3541516552
3537216502	3531516455	3525716411	3521416384
3517116361	3512616340	3508316329	3504516321
3497716311	3492316307	3486716309	3480916319
3835616332	3835616920	3909916920	3909316847
3908516784	3906616717	3903916655	3901116604
3897016542	3892216483	3887116439	3883416409
3877316375	3871916351	3867016331	3860316314
3854016310	3848216312	3842816318	3839116329
4194216345	4194216932	4266716932	4265416811
4263316731	4260516666	4257916615	4252416534
4247316470	4242216428	4237216391	4229916356
4223816336	4216816321	4211216317	4206416320
4202716327	4199916330	4197616338	4195816346
4552016351	4552016943	4622116943	4621516848
4620516778	4619016714	4616616652	4612616575
4607816510	4602216453	4596016399	4591416374
4585016345	4579116329	4574916318	4570516318
4565916319	4563016322	4559816327	4556516339
2325616342	2325616932	2393716932	2393316857
2392616778	2390416706	2388816657	2386216602
2382916542	2378516476	2373816429	2369316391
2365116367	2359216338	2353616317	2347916304
2342416302	2337616308	2332716318	2329116328
2683416354	2683416941	2750516941	2750416871
2749616770	2747216694	2744816630	2739916548
2734716469	2729016419	2723916381	2718716351
2714016330	2709016318	2704416313	2699716312
2696916315	2693816323	2690816331	2687316339
3041816360	3041816953	3108616953	3108716868
3107616792	3105316710	3101516614	3097816547
3092516477	3088616438	3084116401	3079516377
3075616356	3071316341	3067516331	3063016326
3059216324	3055016325	3050716332	3045916348
3399216361	3399216951	3466916951	3466316858
3465416785	3463716723	3460116643	3457416581
3454016526	3450216481	3445316432	3441616406
3436716376	3432316356	3426616339	3421216328
3416316324	3412416327	3407316336	3403916346
3755716369	3755716962	3824716962	3824616893
3823216815	3820816729	3818216663	3814116588
3809516523	3806416488	3802016450	3797516417
3793016391	3788016366	3783516354	3779316345
3773716341	3767716344	3763416350	3759116364
4113816382	4113816975	4184216975	4183716899
4183116822	4180516752	4177616670	4174516617
4169616552	4165016496	4159416447	4154016416
4148116388	4142616371	4138116361	4133916356
4130016352	4127116356	4123016360	4118216370
4471016393	4471016988	4544116988	4543716908

TABLE XXXIII (Continued)

DROP SHAPE DATA FOR FILM NUMBER 17

4542216824	4540016753	4536416672	4532216610
4528016557	4522716502	4517216462	4511416425
4506416401	4502016388	4496316377	4491716370
4487916368	4484016368	4479316376	4475216382
4704516387	4704516975	4779416975	4778616869
4776716784	4773216705	4770016650	4766116593
4760416532	4755516488	4750416453	4746516433
4740416405	4734016385	4726816370	4716316365
4712716369	4710116373	4708316376	4706616380
2211916390	2211916976	2289416976	2289016884
2287216817	2284716751	2281016678	2276016608
2270316547	2265116502	2259916471	2255116440
2251016421	2245816402	2242616392	2237516383
2234516379	2229416373	2223216374	2217216379
2569916373	2569916958	2649516958	2649116876
2647316790	2644216724	2639916651	2635716591
2630116535	2624016485	2619516459	2611516419
2605716396	2600316383	2595316372	2591216368
2587116363	2583816363	2579416364	2574716366
2927816362	2927816944	3009716944	3008816836
3006316764	3003216694	2997216607	2991416543
2987216504	2981816470	2975616436	2970216413
2965216392	2960516378	2955616366	2949616359
2945216352	2940816348	2936516352	2932916352
3285616344	3285616928	3367816928	3367116828
3365416747	3362016692	3358816634	3355316585
3351116539	3346716502	3341516462	3334416423
3328316393	3322416373	3317816359	3312616346
3307116342	3301216337	3295516340	3290216344
3643716332	3643716913	3726016913	3725716828
3723816751	3720416677	3715616607	3710316541
3703616477	3696816436	3691716405	3685016377
3678316356	3672716342	3667616331	3662416326
3657616324	3653316322	3650116324	3646516328
4001616323	4001616904	4083816904	4083916835
4082516764	4080116694	4076816633	4072016568
4066516508	4060116456	4054416418	4050616399
4042416364	4036816344	4031216328	4024616316
4019716313	4014916312	4010616315	4005416316
4360216309	4360216886	4441616886	4441416806
4439716733	4436716658	4431716580	4425916510
4420316459	4413816414	4408516381	4401516353
4396316332	4390316315	4385016308	4380916304
4375916299	4371816298	4367916300	4363416305
4717916290	4717916872	4798316872	4798416796
4797416726	4794716670	4791116593	4786016517
4780116455	4774816412	4770016382	4763816351
4758616329	4754016309	4748816296	4744616289
4739316278	4734516280	4727916280	4721716286
2193316241	2193316823	2271616823	2271316758
2270616699	2269016632	2266016569	2262116506
2257716449	2252916395	2247916358	2242516324
2237716297	2233316275	2228416262	2223116243
2217116235	2211116228	2204016231	2197416233
2552216231	2552216814	2629016814	2628716746
2627616688	2625416614	2622116535	2619216481
2614616425	2609516374	2604716337	2599216300
2593316269	2588216248	2583116228	2577816219
2573216212	2568916210	2563216211	2558016219
2911316224	2911316807	2986016807	2985416727
2984216660	2982816592	2979416523	2975816457

TABLE XXXIII (Continued)

DROP SHAPE DATA FOR FILM NUMBER 17

2969916393	2964916338	2959416295	2954916270
2949016242	2942416219	2937116206	2933216200
2929516195	2923816195	2919416199	2915016210
3268916206	3268916791	3341416791	3341316723
3340516666	3339616607	3336616531	3333116461
3329316400	3323616342	3319316298	3315216272
3310916241	3306316220	3302816207	3297816187
3293516178	3288316172	3281516170	3275816185
3626616187	3626616774	3696816774	3696616687
3695516633	3693316549	3690416465	3686916410
3683516353	3679816313	3676116275	3671916246
3666616212	3661316181	3655616166	3649316152
3644616146	3640116148	3635816157	3630716172
4005416175	4005416766	4074216766	4073916696
4073816638	4072416580	4070616520	4068016449
4065016394	4061316346	4057416293	4054016256
4049616224	4045816198	4041216175	4037816159
4031716142	4026116140	4020016138	4013216150
4363816164	4363816752	4431316752	4430616694
4430216635	4428216514	4425416444	4421116370
4417216314	4413416260	4408616217	4404916193
4399416167	4395616151	4390316138	4386216130
4381616124	4377916127	4373816135	4368316148
4720716150	4720716738	4788716738	4788616670
4787816607	4786216529	4783616454	4780216385
4776816339	4772516278	4768416232	4764816197
4759216162	4754716139	4748916122	4742516109
4738016106	4734616110	4729816120	4726216128
3284316097	3284316688	3352016688	3351716617
3351016548	3349416481	3346816407	3343516339
3340116281	3335616227	3331916183	3328216156
3323716126	3319816105	3314616084	3310716072
3304516061	3298816061	3293616069	3288516083
3642116099	3642116690	3710916690	3710516619
3709916566	3709216501	3706616444	3703416367
3700216310	3696716249	3692616207	3688316169
3682916131	3676716098	3670316079	3661716066
3655116067	3649916080	3647316083	3644816090
4047916094	4047916686	4118016686	4117716620
4117216550	4115416483	4112016394	4108516330
4104016273	4099616223	4094216173	4089516139
4085316117	4079516091	4073316074	4069216068
4063216067	4058416069	4054916075	4051316085
4404216094	4404216685	4477216685	4477216619
4475816549	4474216481	4471316407	4467016333
4463016278	4458316229	4453716188	4448316151
4444016126	4439616105	4434116089	4429516077
4425116075	4420016073	4414216073	4408916084
3336518308	3336518896	3412118896	3411018778
3407418677	3402318577	3397018506	3390218436
3384918391	3381218370	3376418348	3372018328
3367018312	3363418301	3360118294	3356718291
3352618289	3349318291	3346118292	3341418298
3340318337	3340318926	3418218926	3417318825
3414918736	3411618669	3408418608	3404018556
3398118494	3393318455	3386918412	3379218376
3373818354	3368818341	3363218333	3356818327
3352318327	3348218327	3345618334	3343618331
3337418304	3337418892	3417118892	3416818821
3414418737	3411718656	3407618583	3401518507
3396418458	3390118413	3384618382	3378718353

TABLE XXXIII (Continued)

DROP SHAPE DATA FOR FILM NUMBER 17

3374118336	3369118320	3363818307	3357818300
3353218294	3349418295	3345918295	3342018302
3324717949	3324718536	3406118536	3405118443
3402618356	3398618284	3394918220	3390018157
3385118115	3380218076	3373318033	3368118007
3362217986	3358417972	3354217960	3350017953
3345117945	3339717940	3333417942	3329617945
3312417968	3312418552	3394418552	3394018472
3391718384	3388118304	3383118236	3377518172
3371618118	3366218083	3361018054	3353318019
3345817994	3340617979	3335617970	3330417965
3325817964	3322117962	3319317963	3316117966
3310517985	3310518563	3393018563	3392318486
3389918391	3386118308	3380218227	3374718169
3369518132	3364018090	3357918057	3352718032
3346618011	3340817996	3337417987	3332717980
3328917975	3324817972	3320617973	3315417977
3304217980	3304218547	3387218547	3386818474
3384218375	3379418288	3373118213	3367918158
3361118104	3356518078	3350118047	3344018024
3339318006	3333517987	3329417981	3324417976
3319817972	3315617972	3312617975	3309517977
3304917986	3304918567	3387018567	3386418475
3384018392	3380618325	3376718263	3371718206
3367118157	3362818123	3358418094	3353818068
3348818045	3344618029	3339818014	3332917996
3328417986	3323417978	3318517978	3312317980
3314817985	3314818566	3395518566	3395318494
3393418415	3390418344	3386418269	3381218208
3376018150	3371418112	3366618082	3361218053
3354918023	3348918000	3342217984	3335817975
3332117970	3328817971	3324517970	3320417978
3320018064	3320018648	3399818648	3399418585
3397618501	3394918426	3390618349	3385618278
3379418218	3373218172	3368318141	3363218117
3358218095	3352418074	3347618064	3344318058
3340418051	3335818048	3330318050	3325318056
3313418068	3313418652	3391418652	3390018530
3386318426	3382418352	3378418293	3374618241
3369818196	3365618165	3361318143	3356418113
3351718092	3348218081	3344018069	3337918053
3333218048	3328618045	3324118049	3319218056
3316418074	3316418659	3392118659	3391718587
3390318498	3387418433	3384618361	3380018294
3374918231	3369218184	3362618138	3357418110
3353218090	3348618074	3344618062	3339018052
3333918049	3329618053	3325918057	3322118067
3316918088	3316918671	3390018671	3389418573
3386818476	3384718420	3381318349	3377718293
3373918239	3370018202	3364318156	3358318119
3352118091	3346818071	3342418062	3337718055
3333218054	3328018054	3324718061	3321218075
3317618147	3317618736	3388318736	3387618633
3386018554	3383218478	3380018411	3376818352
3372418296	3367518247	3362118204	3357118172
3352518148	3347818133	3344018121	3339318113
3335118112	3331218114	3327518118	3322818131
3312018201	3312018791	3381018791	3380618709
3379718619	3376818532	3373018456	3368718386
3363718318	3358918273	3355718247	3351818223
3348018202	3343418186	3339618173	3334118165

TABLE XXXIII (Continued)

DROP SHAPE DATA FOR FILM NUMBER 17

3329618161	3325918161	3322018170	3317418183
3321718205	3321718797	3389318797	3388818701
3387218608	3384918532	3382618476	3379018407
3375318354	3371018304	3366618267	3361318230
3356418203	3351818186	3347818176	3343418168
3339818163	3335818164	3331818172	3327718183
3318018217	3318018810	3386018810	3385418705
3384118615	3381918537	3379218476	3375518416
3372318368	3367118310	3362618270	3357718237
3352818206	3347518189	3343618179	3339018176
3334718172	3331018179	3327618183	3324218195
3316218231	3316218824	3384818824	3384518744
3383118643	3380418568	3377418493	3374618436
3370618382	3366118334	3361718294	3357718262
3353118238	3348418214	3344218201	3339018194
3333718191	3329318192	3325418200	3321118213
3310018248	3310018839	3379318839	3379218764
3377718686	3376018610	3373818550	3370618486
3367218428	3362818372	3358018329	3353618297
3348018262	3343218241	3338818226	3333018211
3327518207	3323118211	3318918218	3315618224
3309318338	3309318929	3380018929	3379618846
3378118753	3375718683	3372318613	3369118554
3364518494	3359518446	3355318409	3351118380
3345618356	3340318328	3335318316	3332218311
3327518303	3323018306	3319218310	3315218320
3306018354	3306018945	3379118945	3378818876
3377918798	3375218716	3372318658	3368618592
3364818538	3361718502	3357318460	3353118427
3348818395	3343818372	3339618354	3333518335
3328518325	3324218324	3319618326	3313618332
3306718369	3306718959	3382118959	3381518880
3379618775	3376618704	3373018640	3369018582
3364618525	3359818486	3354518446	3348018407
3342318385	3336518367	3332418355	3327918349
3324118344	3320518344	3316418349	3311718358
3305318389	3305318979	3382818979	3381518860
3378818770	3375418701	3372018644	3368618600
3364218554	3359118509	3354418473	3349318445
3343818420	3340018406	3335418394	3330218379
3326218371	3322418370	3317718372	3312218373
3297218316	3297218905	3376818905	3375818808
3373218718	3370218652	3367018595	3363318549
3360318513	3356018473	3352118445	3347218407
3342218382	3335918355	3329918336	3324218318
3318618311	3313118310	3307118307	3301218316
3296018338	3296018924	3377318924	3376818820
3374218734	3371318671	3367018607	3362218553
3357418501	3352418463	3347418434	3341818404
3336218381	3330718360	3325718347	3319618335
3314518327	3309418327	3304618329	3299718334
3291418338	3291418922	3373718922	3373318826
3371018743	3367418672	3363818617	3360018568
3355918525	3351818489	3347218455	3341018419
3333818389	3327618367	3320318346	3313918332
3307318327	3300518326	3297318329	3294818334
3299918334	3299918921	3383218921	3382618822
3378618712	3372418610	3364618526	3356118458
3349618416	3343918392	3336618368	3331918352
3327518346	3324018337	3320718332	3317318330
3314018330	3311118328	3307318329	3303918332

TABLE XXXIII (Continued)

DROP SHAPE DATA FOR FILM NUMBER 17

3292618325	3292618908	3375518908	3374718816
3371018707	3367918647	3363618586	3358618533
3354518491	3348818444	3341818406	3336918386
3332018365	3325918347	3320418333	3314018324
3309118319	3304818317	3300918315	3297218320
3287418314	3287418897	3370018897	3369218813
3367318737	3364718672	3360218596	3356318542
3350918490	3345918450	3340518416	3336018391
3330218364	3325116346	3320018329	3314618316
3308518309	3304218302	3300218303	3294718307
3290118304	3290118888	3371318888	3370718796
3368318707	3364218626	3359718556	3355018501
3349218449	3343918410	3338218379	3332418352
3326618326	3322318314	3317718300	3312918294
3308418290	3303318290	3298818288	3295218293
3288318298	3288318882	3367818882	3367418816
3365418711	3362618641	3359018578	3354218517
3349018464	3342618410	3336018373	3329518344
3323718315	3319418302	3315918294	3311618287
3307018281	3302418279	3298718282	3293618287
3283318281	3283318864	3361418864	3360818769
3358318688	3355318609	3351818549	3347118489
3342618439	3337718397	3331718352	3327018329
3322618306	3318018290	3314018276	3309318268
3304918260	3299918256	3295318256	3290218264
3272918272	3272918856	3348318856	3347218751
3344618654	3341418579	3337618515	3334418472
3329818425	3325918384	3322318357	3318418331
3314318310	3309918286	3304318266	3297818252
3292018245	3287618246	3282818249	3278218258
3271418259	3271418844	3344518844	3344018762
3341918664	3338018570	3334418507	3330118448
3325918398	3321918361	3317418323	3313718299
3310218279	3305718259	3300818241	3296718231
3292018228	3287118227	3281718228	3276918239
3269218258	3269218847	3340818847	3339818737
3337818646	3334918573	3331518506	3327418450
3323218392	3319018355	3314618321	3309918290
3305918270	3301218250	3296818235	3292018228
3287618224	3283018227	3278018234	3273618248
3255918245	3255918836	3325018836	3324318727
3322718639	3320418575	3317818514	3314718459
3311518415	3308118371	3304318335	3300618303
3296218272	3292718253	3287418231	3281718215
3275118208	3270218209	3265818215	3260718228
3236618239	3236618828	3304518828	3304118757
3303618685	3301618608	3299418541	3296218472
3292218414	3288218362	3284118318	3280118288
3275218252	3269918229	3265418214	3260218200
3255218197	3251018198	3246018204	3240918220
3233418233	3233418823	3301218823	3300918740
3299518646	3297218564	3294018489	3289818421
3286818375	3283118335	3278718293	3274018261
3268418232	3263818212	3259718199	3254918195
3250118193	3244918199	3240418210	3236918215
3219418110	3219418700	3287218700	3286818625
3285618526	3283318445	3280718383	3278118330
3275418284	3271318233	3267618191	3263718162
3258718126	3254418105	3248218082	3242218072
3237418068	3232918069	3228818070	3224118092
3221118100	3221118693	3289918693	3289318599

TABLE XXXIII (Continued)

DROP SHAPE DATA FOR FILM NUMBER 17

3287518496	3285118423	3281718353	3278618303
3275518257	3270718201	3266718167	3261818133
3257818111	3253618092	3248218076	3242318067
3237618062	3233618067	3229618072	3225218086
3222818098	3222818689	3293218689	3292618620
3291118514	3288018431	3285618371	3282518315
3278918265	3274618221	3269418169	3265418140
3260618114	3257418098	3253818085	3249718070
3245018063	3239618062	3235118065	3229418074
3223418101	3223418692	3295718692	3295218596
3293018488	3289818414	3285618336	3281218279
3276718227	3272118190	3267618154	3264018132
3259918113	3256018097	3252218086	3247518075
3243018070	3238818071	3234318075	3229018086
3217618096	3217618686	3292518686	3292018577
3289918499	3286918434	3283018361	3278618304
3275318261	3270918215	3266018182	3261318151
3257618130	3252618109	3247818091	3242018078
3237018071	3231818069	3226618079	3221918068

DATA FOR EXPERIMENTAL DECAY TIMES

The high-speed damping films were edited to determine the point at which the damping of the oscillation began. Shape measurements were then made on the micro-comparator of the frames with the maximum amplitude from that point on. These frames characterized the damping curve. Equilibrium shapes were obtained from frames at the end of films. The time was obtained from the 1/1000-sec. marks on the film. The drop top amplitudes and the relative times obtained for these films are shown in Table XXXIV.

TABLE XXXIV

EXPERIMENTAL DATA FOR THE DAMPING CURVES

Time, 10^{-3} sec.	Amplitude of Drop Top, $x10^{-2}$ mm.	Time, 10^{-3} sec.	Amplitude of Drop Top, $x10^{-2}$ mm.
(Film 74, Vol. = 6.41 $mm.^3$)		(Film 72, Vol. = 4.46 $mm.^3$)	
9.5	16.75	7.6	15.63
19.0	15.07	15.2	14.40
28.5	12.50	22.8	12.39
38.1	10.27	30.4	10.38
47.6	7.93	38.0	9.27
57.1	7.48	45.6	8.93
66.7	7.15	53.2	--
76.2	7.48	60.8	--
85.7	7.15	68.4	7.70
95.3	6.60	76.1	5.14
104.4	6.40	83.7	6.48
eq'm	0.00	91.3	--
		98.9	5.36
(Film 35, Vol. = 2.03 $mm.^3$)		eq'm	0.00
5.6	9.49	(Film 37, Vol. = 3.80 $mm.^3$)	
11.2	9.60		
16.8	9.82	7.7	16.30
22.5	9.94	15.4	17.75
28.1	8.37	23.1	18.09
33.7	7.26	30.8	15.18
39.4	7.48	38.5	13.73
45.0	6.36	46.2	11.95
50.6	6.36	53.9	10.38
56.3	5.80	61.6	8.93
61.9	5.58	69.3	7.70
67.5	4.35	77.1	7.15
73.1	4.47	84.8	6.92
eq'm	0.00	eq'm	0.00

TABLE XXXIV (Continued)

EXPERIMENTAL DATA FOR THE DAMPING CURVES

Time, 10^{-3} sec.	Amplitude of Drop Top, $x10^{-2}$ mm.
(Film 39, Vol. = 6.07 mm.^{3})	
9.5	16.30
18.9	16.30
28.4	15.63
37.9	13.73
47.4	12.17
56.8	10.27
66.3	8.93
75.8	7.59
85.3	6.92
94.8	6.42
eq'm	0.00
(Film 44, Vol. = 6.29 mm.^{3})	
10.2	12.84
20.4	13.29
30.6	11.39
40.8	9.38
51.0	7.82
61.2	5.92
eq'm	0.00
(Film 57, Vol. = 2.36 mm.^{3})	
6.6	10.49
13.2	9.27
19.8	8.71
26.4	7.82
33.0	5.02
39.6	3.68
eq'm	0.00
(Film 53, Vol. = 3.69 mm.^{3})	
8.0	12.28
16.0	10.61
24.0	8.60
32.0	6.92
40.0	5.14
48.0	4.24
eq'm	0.00

Time, 10^{-3} sec.	Amplitude of Drop Top, $x10^{-2}$ mm.
(Film 42, Vol. = 1.92 mm.^{3})	
6.0	10.49
11.9	10.83
17.8	8.04
23.8	4.80
29.7	3.35
35.7	3.30
41.6	3.13
eq'm	0.00
(Film 46, Vol. = 2.94 mm.^{3})	
7.3	12.28
14.6	12.73
21.9	14.63
29.2	10.38
36.6	8.26
43.9	4.91
51.2	4.69
eq'm	0.00
(Film 62, Vol. = 2.61 mm.^{3})	
7.0	11.72
13.9	11.16
20.8	11.27
27.8	6.92
34.8	4.13
41.7	2.57
eq'm	0.00
(Film 55, Vol. = 6.89 mm.^{3})	
10.4	13.40
20.8	12.28
31.2	12.39
41.6	8.48
52.1	5.58
eq'm	0.00

TABLE XXXIV (Continued)

EXPERIMENTAL DATA FOR THE DAMPING CURVES

Time, 10^{-3} sec.	Amplitude of Drop Top, $x10^{-2}$ mm.	Time, 10^{-3} sec.	Amplitude of Drop Top, $x10^{-2}$ mm.
(Film 64, Vol. = 4.43 mm.^{3})		(Film 51, Vol. = 9.07 mm.^{3})	
8.6	16.64	12.4	12.17
17.1	15.18	24.8	12.84
25.7	12.50	37.2	13.40
34.3	10.05	49.6	9.71
42.9	8.04	62.0	6.81
51.4	6.81	eq'm	0.00
eq'm	0.00		
(Film 49, Vol. = 5.87 mm.^{3})		(Film 59, Vol. = 7.59 mm.^{3})	
9.4	11.28	11.8	13.26
18.7	10.16	23.6	13.51
20.0	7.82	35.4	5.47
37.4	3.91	47.2	2.68
eq'm	0.00	eq'm	0.00
(Film 67, Vol. = 8.93 mm.^{3})			
11.4	13.29		
22.8	12.28		
34.2	4.91		
45.6	2.57		
eq'm	0.00		

DATA FOR PLOT OF ENERGY CHANGES VERSUS TIME

Figure 13 showed the calculated energy changes in the oscillation of a small water drop (Film 17) throughout one period of oscillation. Table XXXV shows the values of these energy differences for this period of oscillation at intervals of 1/16 period.

TABLE XXXV

DIFFERENTIAL POTENTIAL AND KINETIC ENERGY CHANGES WITH TIME[a]

Drop 17 Water Volume ($mm.^3$) = 0.885 One Period of Motion

Time	Liquid-Vapor Interface	Liquid-Solid Interface	Center of Gravity	Kinetic Energy	Total Energy
0.00	00.0000E-99	00.0000E-99	00.0000E-99	00.0000E-99	00.0000E-99
0.25	27.2870E-04	-23.6451E-04	65.8350E-05	10.2253E-04	10.0000E-09
0.51	56.2210E-04	-34.1835E-04	12.8741E-04	34.9116E-04	00.0000E-99
0.76	78.5150E-04	-36.3718E-04	17.4547E-04	59.5978E-04	10.0000E-09
1.02	86.9080E-04	-36.2216E-04	19.1369E-04	69.8232E-04	10.0000E-09
1.27	78.5160E-04	-36.3728E-04	17.4547E-04	59.5979E-04	00.0000E-99
1.53	56.2210E-04	-34.1835E-04	12.8741E-04	34.9116E-04	00.0000E-99
1.79	27.2880E-04	-23.6461E-04	65.8351E-05	10.2253E-04	11.0000E-09
2.04	10.0000E-08	-10.1000E-08	10.0000E-10	58.3278E-17	-58.3278E-17
2.30	-19.8920E-04	35.8368E-04	-57.1948E-05	10.2253E-04	20.0000E-10
2.55	-30.9610E-04	75.7957E-04	-99.2313E-05	34.9116E-04	-30.0000E-10
2.81	-35.3850E-04	10.7398E-03	-12.4153E-04	59.5978E-04	-10.0000E-09
3.06	-36.3790E-04	11.9434E-03	-13.2320E-04	69.8232E-04	-20.0000E-09
3.32	-35.3850E-04	10.7398E-03	-12.4153E-04	59.5979E-04	-20.0000E-09
3.58	-30.9610E-04	75.7958E-04	-99.2314E-05	34.9116E-04	60.0000E-10
3.83	-19.8930E-04	35.8379E-04	-57.1950E-05	10.2254E-04	00.0000E-99
4.09	00.0000E-99	10.0000E-10	-10.0000E-10	23.3311E-16	-23.3311E-16

Time in 10^{-3} seconds
Energy in ergs

[a] E-04 = 10^{-4}, etc.

DATA FOR THE ACCELERATION GRADIENT VERSUS COSINE OF THE CONTACT ANGLE RELATIONSHIP

A linear relationship was found between the cosine of the dynamic contact angle and the "constant" value of the acceleration gradient. The data for two drops (Films 36, 56) were shown in Fig. 17. The values for the data points in these plots and the data for the other drops for which these calculations were made are shown in Table XXXVI.

TABLE XXXVI

CALCULATED ACCELERATION GRADIENT (da/dy) AND COSINE OF THE DYNAMIC CONTACT ANGLE ($\cos\phi$) AT DIFFERENT TIMES IN THE DROP OSCILLATION

Film Number		Phase in the Oscillation, (ωt) $\pi/2$	$3\pi/4$		$3\pi/2$	2π
17	da/dy	22.5×10^{4} sec.$^{-2}$		0.0		-22.5
	$\cos\phi$	-0.0872		-0.2588		- 0.4226
34	da/dy	10.0×10^{4} sec.$^{-2}$		0.0		-10.0
	$\cos\phi$	-0.0349		-0.2672		- 0.4848
36	da/dy	7.5×10^{4} sec.$^{-2}$	5.3	0.0	-5.3	- 7.5
	$\cos\phi$	-0.0174	-0.0941	-0.2756	-0.4478	- 0.5150
73	da/dy	3.0×10^{4} sec.$^{-2}$		0.0		- 3.0
	$\cos\phi$	-0.0698		-0.2588		- 0.4384
41	da/dy	12.5×10^{-4} sec.$^{-2}$		0.0		-12.5
	$\cos\phi$	+0.0174		-0.1736		- 0.3584
45	da/dy	7.5×10^{4} sec.$^{-2}$		0.0		- 7.5
	$\cos\phi$	-0.0174		-0.2079		- 0.3907
56	da/dy	7.5×10^{4} sec.$^{-2}$	5.3	0.0	-5.3	- 7.5
	$\cos\phi$	+0.0698	+0.0209	-0.1045	-0.2385	- 0.2924
63	da/dy	4.5×10^{4} sec.$^{-2}$		0.0		- 4.5
	$\cos\phi$	+0.0872		-0.1132		- 0.3090
77	da/dy	7.5×10^{4} sec.$^{-2}$		0.0		- 7.5
	$\cos\phi$	+0.0872		-0.0958		- 0.2756
81	da/dy	2.01×10^{4} sec.$^{-2}$		0.0		- 2.0
	$\cos\phi$	+0.0349		-0.0958		- 0.2079

Average slope $\sim 3.0 \times 10^{-6}$ cosine ϕ sec.^{2}